

UNIVERSITY OF CALIFORNIA
RIVERSIDE

Robust GPS-INS Outlier Accommodation
in
Nonlinear Bayesian Optimal Estimation

A Dissertation submitted in partial satisfaction
of the requirements for the degree of

Doctor of Philosophy

in

Electrical Engineering

by

Paul F. Roysdon

September 2017

Dissertation Committee:

Professor Jay A. Farrell, Chairperson
Professor Matthew Barth
Professor Nael Abu-Ghazaleh

Copyright by
Paul F. Roysdon
2017

The Dissertation of Paul F. Roysdon is approved:

Committee Chairperson

University of California, Riverside

Acknowledgments

I thank my advisor, Prof. Jay A. Farrell, for the opportunity to pursue this course of study. I appreciate his rigorous theory and writing style. I also thank the members of my defense committee, Prof. Matthew Barth and Prof. Nael Abu-Ghazaleh, for their time and guidance in the several months preceding my final defense.

I thank my industry mentor, David Hartman, for his knowledge and guidance during my earlier years as a Navigation Engineer. I would not have pursued this field of study without your encouragement.

I give my special thanks to my wife Elizabeth, my family, and my Creator. Your love, support and guidance, provided me the strength to see this task through.

I dedicate this work to my wife and family.

ABSTRACT OF THE DISSERTATION

Robust GPS-INS Outlier Accommodation
in
Nonlinear Bayesian Optimal Estimation

by

Paul F. Roysdon

Doctor of Philosophy, Graduate Program in Electrical Engineering
University of California, Riverside, September 2017
Professor Jay A. Farrell, Chairperson

Many highway vehicle applications require reliable, high precision navigation (error less than meter level) while using low-cost consumer-grade inertial and global navigation satellite systems (GNSS). The application environment causes numerous GNSS measurement outliers. Common implementations use a single epoch Extended Kalman Filter (EKF) combined with the Receiver Autonomous Integrity Monitoring (RAIM) for GNSS outlier detection. However, if the linearization point of the EKF is incorrect or if the number of residuals is too low, the outlier detection decisions may be incorrect. False alarms result in good information not being incorporated into the state and covariance estimates. Missed detections result in incorrect information being incorporated into the state and covariance estimates. Either case can cause subsequent incorrect decisions, possibly causing divergence, due to the state and covariance now being incorrect. This dissertation formulates a sliding-window estimator containing multiple GNSS epochs, and solves the full-nonlinear Maximum A Posteriori estimate in real-time. By leveraging the resulting window of residual

als, an improved fault detection and removal strategy is implemented. Experimental sensor data is used to demonstrate the interval RAIM (iRAIM) performance improvement.

Contents

List of Figures	xii
List of Tables	xv
1 Introduction	1
1.1 Background and Perspective	1
1.2 Main Contributions	4
2 Sensors	5
2.1 Preliminary Notation	5
2.2 IMU Background and Theory	7
2.2.1 IMU Background	7
2.2.2 IMU General Measurement Model	8
2.2.3 IMU Measurement Model for Aided INS	10
2.3 GPS/DGPS Background and Theory	11
2.3.1 GPS Background	11
2.3.2 GPS Measurement Models	13
2.3.2.1 Pseudorange Observable	13
2.3.2.2 Carrier Phase Observable	16
2.3.2.3 Delta Pseudorange Observable	18
2.3.3 DGPS Background	19
2.3.4 DGPS Measurement Models	21
2.3.4.1 DGPS Single Differencing	21
2.3.4.2 DGPS Double Differencing	24
2.3.4.3 DGPS Triple Differencing	26
3 Aided Inertial Navigation System	28
3.1 Aided Inertial Navigation	28
3.2 GPS/DGPS Aiding	30
3.3 INS Temporal Propagation	31
3.3.1 Problem Formulation	31
3.3.2 INS Time Propagation Equations	33
3.3.2.1 Attitude Update	33

3.3.2.2	Velocity Update	34
3.3.2.3	Position Update	35
3.3.2.4	Gravity Model	35
3.4	State Correction	36
3.4.1	Problem Formulation	36
3.4.2	Position Velocity and Bias Updates	37
3.4.3	Attitude Update	37
3.4.3.1	Rotation Matrix	37
3.4.3.2	Quaternion	38
3.5	INS Error Model	39
3.6	INS Noise Propagation	40
3.6.1	Problem Formulation	40
3.6.2	Propagation of State Error	42
3.6.2.1	Propagation of Initial State Error	42
3.6.2.2	Noise Propagation	44
3.6.2.3	Summary	46
3.7	Extended Kalman Filtering for GPS-aided INS	46
4	Estimation Theory	51
4.1	Theoretical Solution	52
4.2	Numerical Solution	53
4.3	Optimization: Iterated Solution	56
5	Computational Cost	58
5.1	Computational cost for KF	60
5.2	Computational cost for CRT using Normal Equations	60
5.2.1	Dense Jacobian	61
5.2.2	Sparse Jacobian	63
5.3	Computational cost for CRT using QR Factorization	63
5.3.1	Theory	64
5.3.2	Dense Jacobian	65
5.3.3	Sparse Jacobian	65
5.4	Discussion	67
5.4.1	Normal Equations vs. QR	67
5.4.2	Sparse vs. Dense	67
5.4.3	Estimator Comparison	68
6	Residual Space Outlier Detection	69
6.1	Problem Formulation	71
6.1.1	Null-Hypothesis	72
6.1.2	Alternate-Hypothesis	74
6.2	Complexity	76
6.3	Comparison of DOF's	77

7 CRT using the Soft-Thresholding Operator	79
7.1 Problem Formulation	80
7.1.1 Outlier Model	80
7.1.2 Theoretical Solution	80
7.1.3 Numerical Solution	82
7.2 Solution of CRT with Soft-Thresholding	83
7.2.1 Part 1: Estimate X, holding S constant	83
7.2.2 Part 2: Estimate S, holding X constant	84
7.2.3 CRT-LSS Summary	85
8 Experimental Results	87
8.1 Background	87
8.1.1 Synthetic Data	87
8.1.2 Experimental Data	88
8.1.3 Ground Truth	89
8.1.4 Final Comments	89
8.2 CRT-HT Performance	90
8.2.1 CRT-HT Performance using Synthetic Data	90
8.2.2 CRT-HT Performance using Experimental Data	92
8.3 CRT-LSS Performance	95
8.3.1 Specification of Laplacian Parameters	95
8.3.2 CRT-LSS Performance using Synthetic Data	96
8.3.3 CRT-LSS Performance using Experimental Data	97
8.4 Comparison: CRT-LSS vs. CRT-HT	98
9 Conclusion and Future Work	107
9.1 Contributions	108
9.2 Publication List	108
9.3 Future Work	109
Bibliography	110
A Proofs & Derivations	117
A.1 Attitude Update Derivation	117
A.2 Quaternion Update Approximation	118
A.3 Quaternion Gradient & Hessian Derivation	119
A.4 Proof of Idempotent P	120
A.5 Proof of Rank P	120
A.6 Proof of Idempotent Q	122
A.7 Proof of Rank Q	123
A.8 Physical Interpretation of P & Q	124
A.9 Soft-Thresholding Operator Proof	125

B Neyman-Pearson Lemma	127
B.1 Problem Formulation	127
B.2 Illustrative Example	128
B.3 Relation to ROC Plots	131
C Generalized Likelihood Ratio Test	133
C.1 Problem Formulation	133
C.2 GLRT relation to PFA and Chi-Square	136

List of Figures

1.1	The “Urban Canyon”. (Modified image from [9].)	2
2.1	Typical IMU with signal processing front-end. [5]	9
2.2	Single difference geometry. (Combined image from [6–8].)	23
2.3	Double difference geometry. (Combined image from [6–8].)	25
2.4	Triple difference geometry. (Combined image from [6–8].)	27
3.1	Block diagram of the ECEF referenced INS equations.	32
3.2	Case 1: Divergence of the GPS-INS EKF under poor yaw initialization. . .	50
3.3	Case 2: Divergence of the GPS-INS EKF under worst-case yaw initialization.	50
8.1	Test trajectory around UCR campus. The corner photos identify a variety of real-world environmental factors which adversely affect the performance of a GPS receiver, e.g. trees and tall buildings. The center image shows the number of satellites <i>available</i> along the trajectory for estimation and outlier detection. The UCR base station antenna position is shown with a red ‘X’.	101
8.2	Test set-up. Modern vehicle with GPS antenna located on the center of the roof, and navigation system located inside the cabin.	101
8.3	Satellite ID, elevation angles, and number of satellites available (after double differencing), versus trajectory time.	102

8.4	Receiver Operating Characteristic curves for each CRT-HT algorithm, outlier magnitude and γ . Values for γ correspond to curve ($O = 1.5m$, $L = 1$), however the same values apply to the corresponding tick marks on the other curves. Outlier magnitudes $> 2.5m$ have $P_{CD} = 100\%$. Increasing window length L improves P_{CD} regardless of outlier magnitude. Tick-mark style (e.g. circle, star, etc.) and line color correspond to outlier magnitude. Line style (e.g. solid, dashed, etc.) correspond to CRT window length.	102
8.5	Position error cumulative distributions for each HT algorithm. Based on synthetic data results, the value $\gamma = 1.25$ was selected for all curves to guarantee minimum $P_{CD} > 50\%$	103
8.6	Attitude error cumulative distributions for each HT algorithm. Based on synthetic data results, the value $\gamma = 1.25$ was selected for all curves to guarantee minimum $P_{CD} > 50\%$	103
8.7	Optimization Statistics for experimental data trajectory using CRT-HT with $L = 20$ and $\gamma = 1.00$, including: total number of iterations, final $\ \mathcal{C}(\hat{\mathbf{X}})\ _2$, number of available and number of removed SVs, $\ 2D\ Pos.\ Error\ _2$ and estimated position standard deviation, and both per-epoch GDOP and CRT-window GDOP (i.e. computed using all SVs in the CRT window).	104
8.8	CRT optimal yaw estimation.	104
8.9	Receiver Operating Characteristic curves for each CRT-LSS algorithm, outlier magnitude, and λ_ρ . Values for λ_ρ correspond to curve ($O = 1.5m$, $L = 1$), however the same values apply to the corresponding tick marks on the other curves. Outlier magnitudes $> 2.5m$ have $P_{CD} = 100\%$. Increasing window length L improves P_{CD} regardless of outlier magnitude. Tick-mark style (e.g. circle, star, etc.) and line color correspond to outlier magnitude. Line style (e.g. solid, dashed, etc.) correspond to CRT window length.	105
8.10	Position error cumulative distributions for each LSS algorithm. Based on synthetic data results, the value $\lambda_\rho = 1.00$ was selected for all curves to guarantee minimum $P_{CD} > 50\%$	105
8.11	Attitude error cumulative distributions for each LSS algorithm. Based on synthetic data results, the value $\lambda_\rho = 1.00$ was selected for all curves to guarantee minimum $P_{CD} > 50\%$	106
8.12	Optimization Statistics for experimental data trajectory using CRT-LSS with $L = 20$ and $\gamma = 1.00$, including: total number of iterations, final $\ \mathcal{C}(\mathbf{X}, \mathbf{S})\ _2$ and final $\ \hat{\mathbf{S}}\ _1$, number of available and number of thresholded SVs, $\ 2D\ Pos.\ Error\ _2$ and estimated position standard deviation, and both per-epoch GDOP and CRT-window GDOP (i.e. computed using all SVs in the CRT window). . .	106

A.1	For a general space in \mathbb{R}^3 , the mapping $\mathbf{P}\mathbf{y} = \hat{\mathbf{y}}$ is the estimate for \mathbf{y} , and $\mathbf{Q}\mathbf{y} = \mathbf{r}$ is the estimation residual for \mathbf{y}	124
B.1	Signal spread due to noise, and resulting overlap.	129
B.2	The four regions of hypothesis testing, defined by two overlapping distributions (a & b) and the vertical line of the decision threshold γ	129
B.3	An example result of <i>hits</i> versus <i>false alarms</i> , due to shifting the threshold γ	130
B.4	ROC plot for Hits (P_D) versus False Alarms (P_{FA}).	131

List of Tables

2.1	Notational conventions.	7
2.2	User Range Error (URE) standard deviation & time correlation [25].	16
5.1	Computational cost for dense and sparse matrices.	59
5.2	Computational cost for matrix decompositions.	59
5.3	Computational cost for LS algorithms (Section 5.5.9 [41]).	59
5.4	Computational cost for the KF (Section 3.3.1 [43]).	60

Chapter 1

Introduction

1.1 Background & Perspective

The past decades have seen the rapid rise and adoption of ubiquitous navigation systems. This has been driven by the availability of low cost sensors (e.g., GNSS and cameras), inertial instruments, and computation. With sensor fusion, these systems can exhibit very good accuracy (e.g. sub-meter error). However, further improvements in the reliability and continuity of this accuracy are required to fully support autonomous vehicle operations, especially in urban environments, where variations in the operating conditions can have critical effects. In GNSS applications such outlier measurements can be caused by multi-path, non-line of sight signals, or foliage (see Fig. 1.1). In the design of a reliable, high-performance system, it is critical to remove the effects of outlier measurements before they degrade performance.

RAIM is a set of techniques designed to detect and remove with GNSS receiver

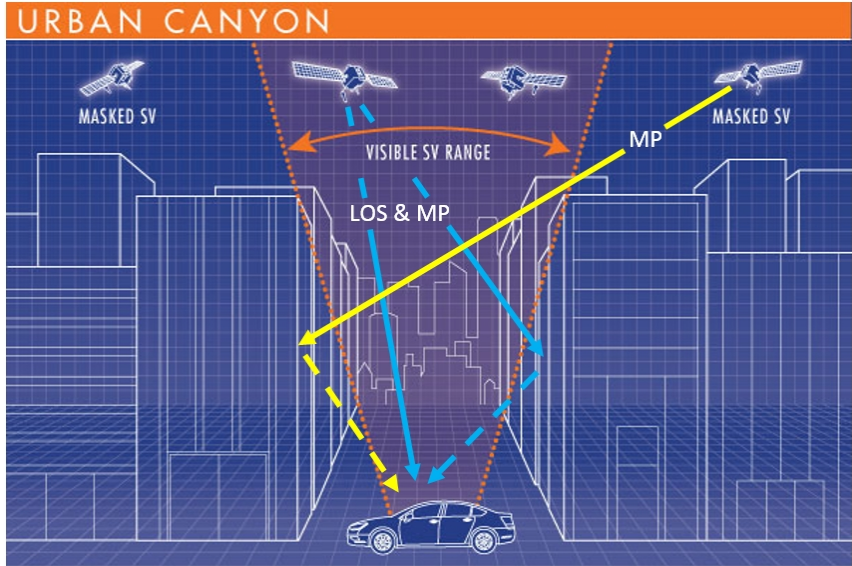


Figure 1.1: The “Urban Canyon”. (Modified image from [9].)

outlier measurements [16, 17, 51, 91]. Successful accommodation requires measurement redundancy [16]. Many RAIM implementations assume that only a single outlier occurs in any epoch. Multiple outlier detection has also been well developed [3, 17, 51]. The authors of [48] included an inertial measurement unit (IMU) and a Kalman filter to “extend” the RAIM capabilities. Their method is called eRAIM. Both RAIM and eRAIM are based on measurements from a single epoch, limiting data redundancy. Furthermore, the residual generation algorithm in RAIM and eRAIM assumes a linear system.

Data redundancy, quantified by the number of degrees-of-freedom (DOFs), is critical to successful outlier accommodation. Redundancy can be enhanced both by adding additional sensors or by solving the estimation problem using all sensor data within a sliding temporal window. Herein we consider the sliding window approach. We build on theoretical and computational methods developed within the control [52], robotics [73],

simultaneous localization and mapping (SLAM) [22, 24, 55], and receding horizon estimation [46, 69, 75, 106] literatures. The resulting full nonlinear *Maximum A Posteriori* (MAP) estimator, without outlier accommodation, is presented in [105]. This dissertation extends [105] with two methods to accommodate outlier measurements within the temporal window. The first method builds on traditional residual space methods which also form the basis for RAIM and eRAIM. An earlier version of the residual space method was presented in [91, 101–103]. The second method is motivated by the Least Soft-thresholded Squares (LSS) approach, building on l_1 -regularization, that was recently presented in the computer vision literature [71, 97, 104]. An earlier version of the LSS approach was presented in [50, 79]. The contributions of this dissertation relative to [3, 104] and [49] are multiple outlier accommodation using an iterated nonlinear optimal estimator with a multi-epoch sliding window.

The theoretical approach presented in Chapters 4–7 is general. It applies to any set of aiding sensors (e.g., cameras, GNSS, Radar, LiDAR) combined with kinematic integration for high-bandwidth based on data from an IMU or encoders. The focus on GNSS and INS herein should be thought of as a particular example, both to demonstrate the application of the theory and to allow experimental analysis of performance. Both theoretical and computational trade-off’s are discussed. Both estimators are evaluated using both simulated data and real-world experimental data involving urban canyons and overhead foliage.

1.2 Main Contributions

1. The first literature report comparing window length (of a sliding-window nonlinear optimal estimator for a tightly coupled DGPS-INS) versus position and attitude performance, and contrasts to both the extended Kalman filter (EKF) and the iterated extended Kalman filter (IEKF).
2. The first literature report of a sliding-window nonlinear optimal estimator for a tightly coupled DGPS-INS, using Residual Space for measurement outlier accommodation in a GPS-challenged urban environment.
3. The first literature report of a sliding-window nonlinear optimal estimator for a tightly coupled DGPS-INS, using l_1 -regularization for measurement outlier accommodation in a GPS-challenged urban environment.

Chapter 2

Sensors

This chapter introduces the practical and theoretical background on the sensors used in this dissertation. An IMU, discussed in Section 2.2, is used for short-term navigation and full state propagation, while a GPS receiver, discussed in Section 2.3, is used for long-term navigation and state correction.

2.1 Preliminary Notation

The primary references for this section are [25, 43, 66]. Conventions and symbols are provided in Table 2.1. The following list defines the notation and equations used in this dissertation:

- $\mathbf{p}_{ab} \in \mathbb{R}^3$ denotes the translation from the origin of frame a to that of frame b .
- $\mathbf{v}_{ab} \in \mathbb{R}^3$ denotes the relative velocity of frame b with respect to frame a .
- $\boldsymbol{\omega}_{ab} \in \mathbb{R}^3$ denotes the relative rate of rotation of frame b with respect to frame a .

- The superscript indicates the frame of reference, e.g., \mathbf{p}_{ab}^c denotes \mathbf{p}_{ab} represented in frame c .
- $\mathbf{R}_a^b \in SO(3)$ ¹ denotes the rotation matrix transforming vectors from frame b to frame a , e.g., $\mathbf{p}_{ab}^b = \mathbf{R}_a^b \mathbf{p}_{ab}^a$. The rotation matrix has the following properties: $|\mathbf{R}_a^b| = 1$ and $(\mathbf{R}_a^b)^\top \mathbf{R}_a^b = \mathbf{I}_3$.
- Let $\boldsymbol{\omega} = [\boldsymbol{\omega}_1, \boldsymbol{\omega}_2, \boldsymbol{\omega}_3]^\top$, then

$$[\boldsymbol{\omega} \times] \triangleq \begin{bmatrix} 0 & -\boldsymbol{\omega}_3 & \boldsymbol{\omega}_2 \\ \boldsymbol{\omega}_3 & 0 & -\boldsymbol{\omega}_1 \\ -\boldsymbol{\omega}_2 & \boldsymbol{\omega}_1 & 0 \end{bmatrix} \in so(3)^2,$$

denotes the skew-symmetric matrix associated to $\boldsymbol{\omega}$. A skew-symmetric matrix has the property $[\boldsymbol{\omega} \times]^\top = -[\boldsymbol{\omega} \times]$.

- For the angular rate $\boldsymbol{\omega}_{ab}^b$, it is often defined that $\boldsymbol{\Omega}_{ab}^b \triangleq [\boldsymbol{\omega}_{ab}^b \times]$.
- The derivative of the rotation matrix \mathbf{R}_a^b has the following relation with the angular rate $\boldsymbol{\omega}_{ab}$ (and then $\boldsymbol{\Omega}_{ab}$),

$$\dot{\mathbf{R}}_a^b(t) = \mathbf{R}_a^b(t) \boldsymbol{\Omega}_{ab}^a = -\boldsymbol{\Omega}_{ab}^b \mathbf{R}_a^b(t). \quad (2.1)$$

- Suppose that the rotation from frame a to frame b is an infinitesimal rotation denoted by $\delta\boldsymbol{\theta} = [\delta\theta_1, \delta\theta_2, \delta\theta_3]^\top$, then the rotation matrix from frame a to frame b can be approximated as

$$\mathbf{R}_a^b = \mathbf{I}_3 - \delta\boldsymbol{\Theta}, \quad (2.2)$$

where $\delta\boldsymbol{\Theta} \triangleq [\delta\boldsymbol{\theta} \times]$.

¹ $SO(3) = \{\mathbf{R} \in \mathbb{R}^{3 \times 3} | \mathbf{R}^\top \mathbf{R} = \mathbf{I}, \det(\mathbf{R}) = +1\}$ denotes the group of *special orthogonal matrix*, see [66].
² $so(3) = \{[\boldsymbol{\omega} \times] \in \mathbb{R}^{3 \times 3} | \boldsymbol{\omega} \in \mathbb{R}^3\}$ denotes the space of all skew-symmetric matrices, see [66].

- Let $\theta \in [-\pi, \pi]$ be an angle, in this dissertation the following notation is used for simplicity: $s\theta \triangleq \sin(\theta)$, $c\theta \triangleq \cos \theta$ and $t\theta \triangleq \tan \theta$.

Table 2.1: Notational conventions.

x	non-bold face variables denote <i>scalars</i>
\mathbf{x}	boldface lower-case denotes <i>vector</i> quantities
\mathbf{X}	boldface upper-case denotes <i>matrix</i> quantities
\bar{x}	true value of \mathbf{x}
\hat{x}	calculated or estimated value of \mathbf{x}
\tilde{x}	measured value of \mathbf{x}
$\delta \mathbf{x}$	error $\mathbf{x} - \hat{\mathbf{x}}$
\mathbf{R}_a^b	transformation matrix from reference frames a to b
\mathbf{x}^a	vector \mathbf{x} represented with respect to frame a
$\mathbb{R}, \mathbb{R}^+, \mathbb{R}^n$	real numbers, reals greater than 0, n -tuples of reals
\mathbb{N}	natural numbers $\{0, 1, 2, \dots\}$
\mathbb{C}	complex numbers
\mathbb{Z}	integer numbers
$(a .. b), [a .. b]$	open interval, closed interval
$\langle \dots \rangle$	sequence (a list in which order matters)
$\{ \dots \}$	set (a list in which order does not matter)
$x_{i,j}$	row i and column j entry of matrix \mathbf{X}
$\mathbf{0}_{n \times m}$ or $\mathbf{0}$	zero matrix
$\mathbf{I}_{n \times n}$ or \mathbf{I}	identity matrix
$ \mathbf{X} $	determinant of matrix \mathbf{X}
R, N	range space, null space
R_∞, N_∞	generalized range space and null space
\mathcal{N}	Normal or Gaussian random variable
\mathcal{L}	Laplace random variable

2.2 IMU Background and Theory

2.2.1 IMU Background

Common industry terms place IMUs into four major categories which stem from US military requirements: Strategic, Tactical, Industrial and Consumer. Strategic typically

refers to systems which are designed for free-inertial navigation, with stability that maintain system accuracy for weeks to months. These are typically used on ships and submarines, but also apply to inter-continental ballistic missiles (ICBMs). Tactical systems are also designed for free-inertial (unaided) navigation, but operate on the order of seconds to minutes, and are typically used on missiles, and unmanned aerial vehicles (UAVs). Industrial systems span the range above and below the ability to sense Earth rate ($\sim 15 \text{ deg/hr}$), and are typically used in a variety of robotics applications. Below Earth rate, it is possible to use a gyro for detecting true heading, without the aid of a magnetometer or GPS. However the in-run bias stability must be significantly below 15 deg/hr to make a good estimation of Earth rate, typically $< 0.1 \text{ deg/hr}$ will suffice. Above 40 deg/hr is considered consumer or automotive grade, and consists of rate gyros which cannot be used to determine heading or roll/pitch angles, but are sufficient to measure angular velocity such as yaw-rate.

2.2.2 IMU General Measurement Model

The IMU is a triad (i.e. three orthogonal axes) angular rate sensor (gyroscope) and a triad linear specific force sensor (accelerometer), thus providing measurements in body frame related to six degree-of-freedom (6DOF) three-dimensional (3D) spatial behavior. The INS will integrate those measurements through the kinematic equations to compute the attitude, velocity, and position of the IMU (see Chapter 3).

A typical IMU contains integrated electronics for calibration, compensation and digital signal processing, as shown in Fig. 2.1.

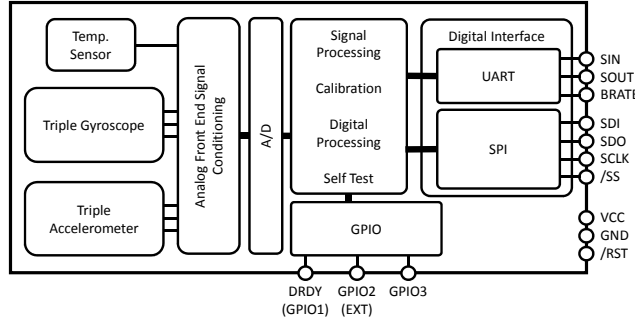


Figure 2.1: Typical IMU with signal processing front-end. [5]

When evaluating an IMU for a specific INS application, one must consider a few key IMU parameters which have an effect on the system-level position, velocity and attitude accuracy. The general form of the equation which represents a single axis sensor (e.g. single-axis gyro), is

$$y(t) = (1 + \epsilon_k) \cdot [u(t) + b(t) + \omega(t) + \eta_{MA} + \eta_Q + \eta_{RRW} + \eta_{RR} + \dots] \quad (2.3)$$

where $y(t)$ is the result of input $u(t)$, which is multiplied by some scale factor ϵ_k , and summed with an in-run bias $b(t)$ and additive stochastic error $\omega(t)$, as well as other errors like misalignment η_{MA} , quantization noise η_Q , rate random walk η_{RRW} , rate ramp η_{RR} , etc. [25].

A simplified model of eqn. (2.3) is

$$\tilde{y}(t) = u(t) + b(t) + n(t),$$

where $\tilde{y}(t)$ is the real-time measurement $y(t)$. Errors like scale factor and misalignment are fixed, given by the manufacturer, and are typically calibrated by the manufacturer and compensated to the extent possible in the signal processing front-end. Whereas, random

walk and bias instability (both are contained in $n(t)$) are random, will cause errors to accumulate over time, and thus need to be characterized and modeled. While some residual calibration errors can also be addressed through on-line optimal estimation, those terms are not within the scope of this dissertation.

2.2.3 IMU Measurement Model for Aided INS

In this dissertation, an IMU is integrated within a GPS-aided INS, and employs some form of optimal estimation (e.g. Extended Kalman Filter (EKF), Maximum A Posteriori (MAP) [35]). For aided INS, the IMU measurement models for the accelerometer $\tilde{\mathbf{y}}_a \in \mathbb{R}^3$ and gyro $\tilde{\mathbf{y}}_g \in \mathbb{R}^3$ are,

$$\tilde{\mathbf{y}}_a = \mathbf{f}_{ib}^b + \mathbf{b}_a + \mathbf{n}_a, \quad (2.4)$$

$$\tilde{\mathbf{y}}_g = \boldsymbol{\omega}_{ib}^b + \mathbf{b}_g + \mathbf{n}_g, \quad (2.5)$$

where $\mathbf{f}_{ib}^b \in \mathbb{R}^3$ is the specific force of the body b -frame with respect to the i -frame resolved in the b -frame, $\boldsymbol{\omega}_{ib}^b \in \mathbb{R}^3$ is the angular rate of the body b -frame with respect to the i -frame resolved in the b -frame, $\mathbf{b}_a, \mathbf{b}_g \in \mathbb{R}^3$ are bias vectors, and $\mathbf{n}_a, \mathbf{n}_g \in \mathbb{R}^3$ are noise vectors. It is common to assume that \mathbf{n}_a and \mathbf{n}_g are white Gaussian processes and

$$\mathbf{n}_a \sim \mathcal{N}(\mathbf{0}, \sigma_a^2 \mathbf{I}), \quad \mathbf{n}_g \sim \mathcal{N}(\mathbf{0}, \sigma_g^2 \mathbf{I}).$$

Furthermore, the bias \mathbf{b}_a and \mathbf{b}_g are often modeled with random walks as

$$\dot{\mathbf{b}}_a = \boldsymbol{\nu}_a, \quad \dot{\hat{\mathbf{b}}}_a = \mathbf{0}, \quad (2.6)$$

$$\dot{\mathbf{b}}_g = \boldsymbol{\nu}_g, \quad \dot{\hat{\mathbf{b}}}_g = \mathbf{0}, \quad (2.7)$$

where the driving noise ν_a and ν_g are also assumed white Gaussian,

$$\nu_a \sim \mathcal{N}(\mathbf{0}, \sigma_{ba}^2 \mathbf{I}), \quad \nu_g \sim \mathcal{N}(\mathbf{0}, \sigma_{bg}^2 \mathbf{I}).$$

Thus, with the IMU measurements and the estimated bias vectors, the specific force and the angular rate can be evaluated as

$$\hat{\mathbf{f}}_{ib}^b = \tilde{\mathbf{y}}_a - \hat{\mathbf{b}}_a, \quad (2.8)$$

$$\hat{\omega}_{ib}^b = \tilde{\mathbf{y}}_g - \hat{\mathbf{b}}_g. \quad (2.9)$$

2.3 GPS/DGPS Background and Theory

This section provides the background on GPS and DGPS, as well as the measurement models which are used in later sections of this dissertation.

2.3.1 GPS Background

The United States Global Positioning System is the most widely applied Global Navigation Satellite System, providing global Positioning-Velocity-Timing (PVT) services. Modern inexpensive GPS receivers with ceramic patch antennas typically achieve 3-8 meter positioning accuracy with the Standard Positioning Service (SPS) [10].

There are four GPS segments:

- Space Segment: the constellation of GPS satellites.
- Control Segment: run by the U.S. Air Force and responsible for the monitoring and operation of the Space Segment.

- User Segment: the user hardware and processing software for positioning, navigation, and timing.
- Ground Segment: the civilian tracking networks that provide the User Segment with reference stations, precise ephemeris, and real time services for differential GPS.

The satellite constellation is designed to have at least four satellites in view at all times. Therefore there are 24 satellites distributed on 6 orbital (elliptical) planes, with a semi-major axis (largest radius) of $26,600\ km$, inclination angle of 55° to the equator, and orbital period approximately $11\ hr.\ 58\ min..$ The signals from the GPS satellites are driven by an atomic clock (typically cesium which has the best long-term stability), with a fundamental frequency of $10.23\ MHz$, from which two carrier signals are generated. The L1 channel (frequency = $1575.42\ MHz$; wavelength = $19.0\ cm$) multiplies the fundamental frequency by 154, while the L2 channel (frequency = $1227.60\ MHz$; wavelength = $24.4\ cm$) multiplies the frequency by 120. The second signal is designed for self-calibration of the signal delay due to the Earth's ionosphere. There are three types of information in the carrier signals:

- The Coarse Acquisition (C/A) code.
- The Precise (P) code.
- The Navigation Message.

The C/A code, on the L1 channel, which repeats every $1\ ms$, is a pseudo-random code generated by a known algorithm. The carrier can transmit the C/A code at $1.023\ Mbps$ (million bits per second). The “chip length”, or physical distance between binary transitions

(between digits +1 and -1), is 293 meters. The C/A code contains the satellite clock time at which the signal was transmitted (with an ambiguity of 1 *ms*).

The P code, identical on both the L1 and L2 channels, which repeats every 267 days, is transmitted at 10.23 *Mbps*, with a chip length of 29.3 meters. Like the C/A code, the P code contains the satellite clock time at which the signal was transmitted, except with ten times the resolution. Unlike the C/A code, the P code is encrypted by a process known as “anti-spoofing”.

The Navigation Message on the L1 channel, is transmitted at 50 *bps* on the L1 channel. This message is a 1500 bit sequence, and therefore takes 30 seconds to transmit. The Navigation Message includes information on the Broadcast Ephemeris (satellite orbital parameters), satellite clock corrections, almanac data (a crude ephemeris for all satellites), ionosphere information, and satellite health status. Obtaining the Broadcast Ephemeris for the entire visible constellation takes 12 minutes. The Broadcast Ephemeris is updated every two hours by the Control Segment, and the Ephemeris message contains a sub-message indicating the time at which the Ephemeris parameters are valid.

2.3.2 GPS Measurement Models

GPS measurements are made through estimating the travel time of the electro-magnetic signals broadcast from the satellite vehicle antenna to the rover antenna.

2.3.2.1 Pseudorange Observable

To calculate user position, the range to each satellite must be determined. However, due to atmospheric effects and clock errors, a pseudorange is modeled. The L1 and

L2 pseudorange measurements for the i -th satellite at time t can be modeled as

$$\tilde{\rho}_{r_1}^i(t) = \|\mathbf{p}_r(t) - \mathbf{p}^i(t)\|_2 + c\delta t_r(t) + \frac{f_2}{f_1} I_r^i(t) + T_r^i(t) + M_{\rho_1}^i(t) + n_{\rho_1}^i(t), \quad (2.10)$$

$$\tilde{\rho}_{r_2}^i(t) = \|\mathbf{p}_r(t) - \mathbf{p}^i(t)\|_2 + c\delta t_r(t) + \frac{f_1}{f_2} I_r^i(t) + T_r^i(t) + M_{\rho_2}^i(t) + n_{\rho_2}^i(t), \quad (2.11)$$

where

- $\|\mathbf{p}_r - \mathbf{p}^i\|_2$ is the geometric distance between the rover position $\mathbf{p}_r \in \mathbb{R}^3$ and the i -th satellite vehicle position $\mathbf{p}^i \in \mathbb{R}^3$,
- $c = 2.99792458 \times 10^8 \text{ m/s}$ is the speed of light,
- $\delta t_r \in \mathbb{R}$ is the receiver clock bias which is identical to all channels of the receiver,
- $f_1 = 1575.42 \text{ MHz}$ is the L1 carrier frequency,
- $f_2 = 1227.60 \text{ MHz}$ is the L2 carrier frequency,
- I_r^i is the Ionospheric error due to dispersive atmospheric effects in the layer of the atmosphere with altitude between 50 and 1000 km,
- T_r^i is the Tropospheric error due to non-dispersive atmospheric effects in the lower part of the atmosphere extending from the surface to 50 km above the surface of the planet,
- $M_{\rho_1}^i$ and $M_{\rho_2}^i$ are the pseudorange multipath errors caused by signal reflections,
- $n_{\rho_1}^i, n_{\rho_2}^i \sim \mathcal{N}(0, \sigma_\rho^{i2})$ are the (non-common mode) pseudorange measurement noise.

In practice, the position of the satellite vehicle is estimated from the orbital data which is broadcast continuously, and updated every two hours, in a data format called

Ephemeris. Updated orbital information, is valid for two hours, and is uplinked to each GPS satellite at 1783.74MHz by the U.S. Air Force Control Center at Schriever Air Force Base, Colorado Springs, USA. Based on the Ephemeris data, the satellite orbit can be fit through the Kepler model [4]. Small fit errors of each satellite orbit is unavoidable, and called ephemeris error E^i . The clock on the satellite is also estimated with error. Thus, the true range between the satellite vehicle and the rover can be represented as

$$\|\mathbf{p}_r - \mathbf{p}^i\|_2 = \|\mathbf{p}_r - \hat{\mathbf{p}}^i\|_2 + E^i + c\delta t^i, \quad (2.12)$$

where $\hat{\mathbf{p}}^i$ is the estimated satellite vehicle position from the ephemeris and δt^i is the residual satellite clock error after performing the correction by model coefficients contained in the Ephemeris message.

The various errors in eqns. (2.10) and (2.11) can be divided into two categories: common mode and non-common mode. The satellite related errors E^i and $c\delta t^i$ are common to all receivers using the same ephemeris. The atmospheric errors I_r^i and T_r^i are common to spatial nearby ($< 15\text{-}20\text{km}$) receivers. The multipath errors ($M_{\rho_1}^i, M_{\rho_2}^i$) and receiver noise ($n_{\rho_1}^i, n_{\rho_2}^i$) depending on the local electromagnetic environment are not common between different receivers. Rewriting the common mode error for the i -th satellite as

$$E_{cm1}^i \triangleq E^i + c\delta t^i + \frac{f_2}{f_1} I_r^i + T_r^i, \quad (2.13)$$

$$E_{cm2}^i \triangleq E^i + c\delta t^i + \frac{f_1}{f_2} I_r^i + T_r^i, \quad (2.14)$$

eqns. (2.10) and (2.11) can be simplified as

$$\tilde{\rho}_{r_1}^i(t) = \|\mathbf{p}_r(t) - \hat{\mathbf{p}}^i(t)\|_2 + c\delta t_r(t) + E_{cm1}^i(t) + M_{\rho_1}^i(t) + n_{\rho_1}^i(t), \quad (2.15)$$

$$\tilde{\rho}_{r_2}^i(t) = \|\mathbf{p}_r(t) - \hat{\mathbf{p}}^i(t)\|_2 + c\delta t_r(t) + E_{cm2}^i(t) + M_{\rho_2}^i(t) + n_{\rho_2}^i(t). \quad (2.16)$$

Table 2.3.2.1 from [25] indicates the magnitude of the above errors and their respective time correlation.

Table 2.2: User Range Error (URE) standard deviation & time correlation [25].

Common Mode Errors	L1, σ	Time correlation
Ionosphere	7-10 m	> 6 hr.
Troposphere	1 m	> 6 hr.
Sv Clock	2 m	2 hr.
Sv Ephemeris	2 m	2 hr.
Non-common Mode Errors		
Multipath	0.1-3.0 m	3-10 min.
Receiver Noise	0.1-0.7 m	< 1 min.

2.3.2.2 Carrier Phase Observable

The GPS carrier phase or *phase* is simply an *angle of rotation*, which is in units of *cycles*, and is directly related to the *frequency*, which is expressed in units of *cycles per second*.

The L1 and L2 carrier phase measurements $\tilde{\varphi}_{r1}^i$ and $\tilde{\varphi}_{r2}^i$ for the i -th satellite at time t can be modeled as

$$\lambda_1 \tilde{\varphi}_{r1}^i(t) = \|\mathbf{p}_r(t) - \hat{\mathbf{p}}^i(t)\|_2 + c\delta t_r(t) + \lambda_1 N_1^i(t) + E_{cm3}^i(t) + M_{\varphi_1}^i(t) + n_{\varphi_1}^i(t), \quad (2.17)$$

$$\lambda_2 \tilde{\varphi}_{r2}^i(t) = \|\mathbf{p}_r(t) - \hat{\mathbf{p}}^i(t)\|_2 + c\delta t_r(t) + \lambda_2 N_2^i(t) + E_{cm4}^i(t) + M_{\varphi_2}^i(t) + n_{\varphi_2}^i(t), \quad (2.18)$$

where

- λ_1 and λ_2 are the wavelength of the corresponding carrier signals,
- N^i is the ambiguous integers representing the unknown number of whole cycles,
- E_{cm3}^i and E_{cm4}^i are common mode errors similar to E_{cm1}^i and E_{cm2}^i detailed in Section [2.3.2.1](#), defined as

$$E_{cm3}^i = E^i + c\delta t^i - \frac{f_2}{f_1}I_r^i + T_r^i, \quad (2.19)$$

$$E_{cm4}^i = E^i + c\delta t^i - \frac{f_1}{f_2}I_r^i + T_r^i, \quad (2.20)$$

- $M_{\varphi_1}^i, n_{\varphi_1}^i, M_{\varphi_2}^i, n_{\varphi_2}^i$ are non-common mode errors similar to those of pseudorange measurements.

The magnitude of $M_{\varphi_1}^i, n_{\varphi_1}^i, M_{\varphi_2}^i, n_{\varphi_2}^i$ are typically less than 1% of the magnitude of the respective errors in pseudorange measurements [25]. When common mode errors can be mitigated, the carrier phase measurements allow position estimation at the centimeter level. While carrier phase measurements have much lower noise level, they are biased by the unknown (usually large) integer ambiguity $\{N^i\}$, because there is no direct measure of the total number phase cycles of the incoming GPS signal. If the GPS receiver loses count of the oscillations (because of signal obstruction or excessive noise), then a new integer parameter must be introduced to the model. This integer discontinuity in phase data is called *cycle-slip*.

It is important to note that the integer value $N^i(t) \equiv N^i$ and is constant when the Phase-Lock-Loop (PLL) of the receiver for the corresponding channel of the i -th satellite is maintained (i.e., no cycle-slip). Thus, if N^i is estimated in previous epoch and no cycle-slip

occurs, the estimated integer should be used for current and later epochs. In practice, the GPS receiver reports the lock status of the PLL.

The noise $\mathbf{n}_\varphi^i \sim \mathcal{N}(0, \sigma_\varphi^{i,2})$ introduces centimeter ($10^{-2}m$) level range errors.

2.3.2.3 Delta Pseudorange Observable

The Delta Pseudorange observable, often referred to as the Doppler observable, is actually a quantity of subsequent pseudorange measurements over a consecutive time interval.

The Doppler frequency can be expressed as a function of the frequency received by a user f_r to the rate of change of the range between the receiver and the transmitter:

$$f_r = f_T \left(1 - \frac{\dot{R}}{c} \right) \quad (2.21)$$

where f_T is the transmitted frequency, and \dot{R} is the geometric range between the user and the transmitter, and the Doppler shift is defined as $f_r - f_T = f_T \frac{\dot{R}}{c}$.

The delta pseudorange measurement is

$$\Delta\rho(\tau_r(t)) = \rho_r^s(\tau_r(t)) - \rho_r^s(\tau_r(t) - T) \quad (2.22)$$

where $T \leq 1.0$. Eqn. (2.22) defined over the time interval $\tau_r \in [\tau_r(t) - T, \tau_r(t)]$ is

$$\Delta\rho(\tau_r(t)) = \int_{\rho_r^s(\tau_r(t) - T)}^{\rho_r^s(\tau_r(t))} \dot{\rho}_r^s(q) dq. \quad (2.23)$$

If Eqn. (2.22) is divided by T , then the quantity defines an average rate of change of the pseudorange over the interval τ_r

The Doppler observable can be defined as the rate of change of the pseudorange at the midpoint of the interval $\tau_r \in [\tau_r(t) - T, \tau_r(t)]$. For the Doppler observable to be valid,

the receiver must maintain phase lock over the interval, wherein the Doppler observable can be computed as

$$\Delta\rho(\tau_r(t)) = \lambda (\phi_r^i(\tau_r(t)) - \phi_r^i(\tau_r(t) - T)). \quad (2.24)$$

The measurement of the Doppler shift (in Hz) at the receiver is

$$D(\tau_r(t)) = \frac{\Delta\rho(\tau_r(t))}{\lambda T}. \quad (2.25)$$

The Doppler measurement model is

$$\lambda T D_r^s(\tau_r(t)) = (\rho_r^s(\tau_r(t)) - \rho_r^s(\tau_r(t) - T)) - c\Delta\dot{t}^i + \epsilon(\tau_r(t)). \quad (2.26)$$

Temporal differences for E^i , I_r^i , and T_r^i are small relative to other terms, and therefore neglected. The measurement error due to multipath and receiver noise is $\epsilon(\tau_r(t))$. The (uncorrected) satellite clock drift rate is $\Delta\dot{t}^i = \Delta t^i(\tau_r) - \Delta t^i(\tau_r - T)$, where $\Delta\dot{t}^i$ is the correction of the Doppler measurement accounting for satellite clock drift rate (see Section C.1 of [25]). A linearized model for the Doppler measurement is

$$\lambda D_r^i = \mathbf{h}^\top(\mathbf{v}_r - \mathbf{v}^i) + c\Delta\dot{t}_r - c\Delta\dot{t}^i + \epsilon. \quad (2.27)$$

where \mathbf{h}^\top is the line-of-sight vector from the satellite to the user position, \mathbf{v}_r is the velocity of the receiver, \mathbf{v}^i is the i -th satellite velocity (see Section C.4 of [25]).

2.3.3 DGPS Background

To achieve reliable high precision positioning, DGPS may be employed, using either satellite-based corrections via the Wide Area Augmentation Service (WAAS) transmitted on the L1 channel by civilian geo-stationary satellites [11], or ground-based corrections

via publicly available correction service, e.g. Continuously Operating Reference Station (CORS) [88], and Nationwide Differential Global Positioning System (NDGPS) [33].

The DGPS technique removes (most of) the spatial-common errors between the rover receiver and the base receiver. Standard DGPS requires that the global position of the base station is well-surveyed such that the spatial-common errors can be calculated precisely. With a base station in the range of a few tens of kilometers, DGPS accuracy is on the order of $1m$ (1σ), growing at the rate of $1m$ per $150km$ of separation [57].

To transmit the differential GNSS message, a non-proprietary and efficient protocol was defined by the Special Committee 104 on DGNSS of the Radio Technical Commission for Maritime Services (RTCM) [83]. This standard is referred as the RTCM standard, and the current version is 3.2.

“Networked Transport of RTCM via Internet Protocol” (NTRIP) [34] is an application-level protocol on the Transmission Control Protocol/Internet Protocol (TCP/IP) stack, which is used to stream GNSS data over the Internet. NTRIP is a generic, stateless protocol based on the Hypertext Transfer Protocol (HTTP/1.1) and the Real Time Streaming Protocol (RTSP). NTRIP is designed for disseminating differential correction data (e.g. in RTCM format) or other kinds of GNSS streaming data, to stationary or mobile users, over the Internet.

NTRIP consists of three system software components: clients, servers, and casters. An implementation of an NTRIP system includes the NTRIP servers which transmit the RTCM message, generated from base station receivers, to the NTRIP Caster. The rover NTRIP Clients, with valid authorizations, request single or multiple NTRIP streams from the NTRIP Caster. By parsing the RTCM message in the NTRIP stream, the differential

information (e.g. base station GNSS receiver measurements or corrections) can be obtained.

As the mobile communication networks (4G LTE or WiFi) become readily available, the DGPS technique can be used in various scenarios.

While this dissertation will focus on CORS DGPS via NTRIP, a robust system should employ both WAAS and CORS data, if the mobile communication data-link is unavailable.

2.3.4 DGPS Measurement Models

This section reviews the differential GPS technique, where single-differencing (SD) removes user-range errors, double-differencing (DD) removes GPS receiver clock bias, and triple-differencing (or other more efficient methods e.g. [19, 20, 92]) remove the integer ambiguity from the carrier phase measurement.

2.3.4.1 DGPS Single Differencing

In this section and the two sections that follow, the SD pseudorange measurement is presented to demonstrate the DGPS method, while the SD phase measurement is presented to identify methods with which to resolve the integer ambiguity. Note that the SD technique applies to Doppler measurements, with appropriate modifications, however only the SD pseudorange and phase measurements are presented herein.

In DGPS, it is assumed that there exists a nearby (within 15-20km) stationary (i.e., $\mathbf{p}_b(t) \equiv \mathbf{p}_b \in \mathbb{R}^3$) base station that can provide GPS measurements from the base station receiver to the rover. The following pseudorange and phase measurements are available to the rover,

$$\tilde{\rho}_{b_1}^i(t) = \|\mathbf{p}_b - \hat{\mathbf{p}}^i(t)\|_2 + c\delta t_b(t) + E_{cm1}^{ib}(t) + M_{\rho_1}^{ib}(t) + n_{\rho_1}^{ib}(t), \quad (2.28)$$

$$\tilde{\rho}_{b_2}^i(t) = \|\mathbf{p}_b - \hat{\mathbf{p}}^i(t)\|_2 + c\delta t_b(t) + E_{cm2}^{ib}(t) + M_{\rho_2}^{ib}(t) + n_{\rho_2}^{ib}(t), \quad (2.29)$$

$$\lambda_1 \tilde{\varphi}_{b_1}^i(t) = \|\mathbf{p}_b - \hat{\mathbf{p}}^i(t)\|_2 + c\delta t_b(t) + \lambda_1 N_1^{ib}(t) + E_{cm3}^{ib}(t) + M_{\varphi_1}^{ib}(t) + n_{\varphi_1}^{ib}(t), \quad (2.30)$$

$$\lambda_2 \tilde{\varphi}_{b_2}^i(t) = \|\mathbf{p}_b - \hat{\mathbf{p}}^i(t)\|_2 + c\delta t_b(t) + \lambda_2 N_2^{ib}(t) + E_{cm4}^{ib}(t) + M_{\varphi_2}^{ib}(t) + n_{\varphi_2}^{ib}(t). \quad (2.31)$$

Base stations should be established in a good electromagnetic environment (e.g. on the top of the hill or high building with open sky, no multipath effects), such that it is valid to assume that $M_{\rho_1}^{ib} = M_{\rho_2}^{ib} = M_{\varphi_1}^{ib} = M_{\varphi_2}^{ib} \equiv 0$. Furthermore, the base position \mathbf{p}_b should be well surveyed with respect to the global frame, such that with the differential technique, more precise global positioning can be realized. If the base station is close to the rover, the following identity is valid $E_{cm1}^i(t) = E_{cm1}^{ib}(t)$, $E_{cm2}^i(t) = E_{cm2}^{ib}(t)$, $E_{cm3}^i(t) = E_{cm3}^{ib}(t)$, $E_{cm4}^i(t) = E_{cm4}^{ib}(t)$. Since the satellite related errors E^i and $c\delta t^i$ are common to all receivers at the same epoch, only the atmospheric errors I_r^i and T_r^i depend on the locations.

With the known base station position \mathbf{p}_b , the SD L1 pseudorange and phase models are defined as

$$\begin{aligned} \Delta \tilde{\rho}_1^i(t) &= \tilde{\rho}_{r_1}^i(t) - \tilde{\rho}_{b_1}^i(t) \\ &= (\|\mathbf{p}_r(t) - \hat{\mathbf{p}}^i(t)\|_2 - \|\mathbf{p}_b - \hat{\mathbf{p}}^i(t)\|_2) + (c\delta t_r(t) - c\delta t_b(t)) \\ &\quad + (E_{cm1}^i(t) - E_{cm1}^{ib}(t)) + (M_{\rho_1}^i(t) - M_{\rho_1}^{ib}(t)) \\ &\quad + (n_{\rho_1}^i(t) - n_{\rho_1}^{ib}(t)) \\ &= \Delta R(\mathbf{p}(t), \hat{\mathbf{p}}^i(t)) + c\Delta\delta t(t) + \Delta T^i(t) - \frac{f_2}{f_1} \Delta I^i(t) + \Delta M_{\rho_1}^i(t) + \Delta n_{\rho_1}^i(t) \end{aligned} \quad (2.32)$$

$$\begin{aligned}
\lambda_1 \Delta \tilde{\varphi}_1^i(t) &= \tilde{\varphi}_{r_1}^i(t) - \tilde{\varphi}_{b_1}^i(t) \\
&= (\|\mathbf{p}_r(t) - \hat{\mathbf{p}}^i(t)\|_2 - \|\mathbf{p}_b - \hat{\mathbf{p}}^i(t)\|_2) + (c\delta t_r(t) - c\delta t_b(t)) \\
&\quad + (\lambda_1 N_1^i(t) - \lambda_1 N_1^{ib}(t)) + (E_{cm3}^i(t) - E_{cm3}^{ib}(t)) \\
&\quad + (M_{\varphi_1}^i(t) - M_{\varphi_1}^{ib}(t)) + (n_{\varphi_1}^i(t) - n_{\varphi_1}^{ib}(t)) \\
&= \Delta R(\mathbf{p}(t), \hat{\mathbf{p}}^i(t)) + c\Delta\delta t(t) + \lambda_1 \Delta N_1^i(t) + \Delta T^i(t) \\
&\quad - \frac{f_2}{f_1} \Delta I^i(t) + \Delta M_{\varphi_1}^i(t) + \Delta n_{\varphi_1}^i(t)
\end{aligned} \tag{2.33}$$

where the function $R(\mathbf{p}(t), \hat{\mathbf{p}}^i(t)) = \|\mathbf{p}_r(t) - \hat{\mathbf{p}}^i(t)\|_2$. The Δ symbol is a mnemonic device to emphasize that the difference is made between two points on the ground for the same satellite i . The SD L2 pseudorange and phase models are similarly defined. An example of the single difference geometry is shown in Fig. 2.2.

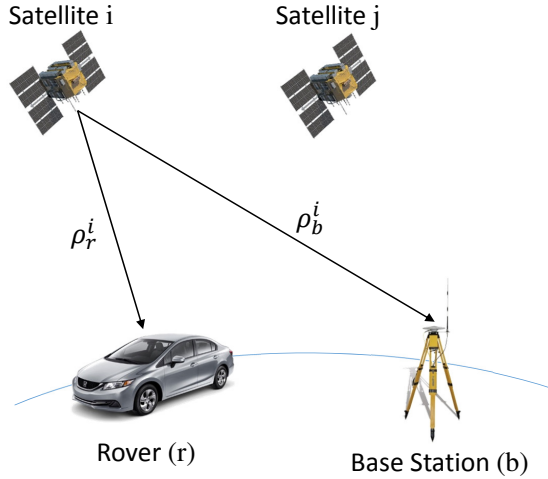


Figure 2.2: Single difference geometry. (Combined image from [6–8].)

While the difference in transmission time of the satellite to each base station can be as much as a few milli-seconds: over a milli-second (10^{-3} sec.) the satellite clock error will differ by 10^{-12} sec., which translates to a distance error of $10^{-12}c$, or 0.3 mm . Differential troposphere can be ignored for horizontal separations less than 30 km , however the differences in height should be modeled. Differential ionosphere can be ignored for separations less than 30 km , depending on ionospheric conditions, however it is recommended to calibrate the ionospheric uncertainty using a dual-frequency receiver for separation distances larger than a few kilometers. While the SD method reduces or eliminates many of the error sources, only a relative position can be calculated. Furthermore, the receiver clock bias is still unknown.

2.3.4.2 DGPS Double Differencing

The double difference is used to remove GPS receiver clock bias. The SD observations for two receivers, r and b , observing satellites, i and j , forms the DD measurement models such that

$$\begin{aligned}
 \nabla \Delta \tilde{\rho}_1^{ij}(t) &= \Delta \tilde{\rho}_1^i(t) - \Delta \tilde{\rho}_1^j(t) \\
 &= (\Delta R(\mathbf{p}(t), \hat{\mathbf{p}}^i(t)) - \Delta R(\mathbf{p}(t), \hat{\mathbf{p}}^j(t))) + (c\Delta\delta t(t) - c\Delta\delta t(t)) \\
 &\quad + (\Delta T^i(t) - \Delta T^j(t)) - \left(\frac{f_2}{f_1} \Delta I^i(t) - \frac{f_2}{f_1} \Delta I^j(t) \right) \\
 &\quad + (\Delta M_{\rho_1}^i(t) - \Delta M_{\rho_1}^j(t)) + (\Delta n_{\rho_1}^i(t) - \Delta n_{\rho_1}^j(t)) \\
 &= \nabla \Delta R(\mathbf{p}(t), \hat{\mathbf{p}}^i(t)) + \nabla \Delta T^{ij}(t) - \frac{f_2}{f_1} \nabla \Delta I^{ij}(t) \\
 &\quad + \nabla \Delta M_{\rho_1}^{ij}(t) + \nabla \Delta n_{\rho_1}^{ij}(t)
 \end{aligned} \tag{2.34}$$

$$\begin{aligned}
\lambda_1 \nabla \Delta \tilde{\varphi}_1^i(t) &= \lambda_1 \Delta \tilde{\varphi}_1^i(t) - \lambda_1 \Delta \tilde{\varphi}_1^j(t) \\
&= (\Delta R(\mathbf{p}(t), \hat{\mathbf{p}}^i(t)) - \Delta R(\mathbf{p}(t), \hat{\mathbf{p}}^j(t))) + (c \Delta \delta t(t) - c \Delta \delta t(t)) \\
&\quad + (\lambda_1 \Delta N_1^i(t) - \lambda_1 \Delta N_1^j(t)) \\
&\quad + (\Delta T^i(t) - \Delta T^j(t)) - (\frac{f_2}{f_1} \Delta I^i(t) - \frac{f_2}{f_1} \Delta I^j(t)) \\
&\quad + (\Delta M_{\varphi_1}^i(t) - \Delta M_{\varphi_1}^j(t)) + (\Delta n_{\varphi_1}^i(t) - \Delta n_{\varphi_1}^j(t)) \\
&= \nabla \Delta R(\mathbf{p}(t), \hat{\mathbf{p}}^{ij}(t)) + \lambda_1 \nabla \Delta N_1^{ij}(t) + \nabla \Delta T^{ij}(t) - \frac{f_2}{f_1} \nabla \Delta I^{ij}(t) \\
&\quad + \nabla \Delta M_{\varphi_1}^{ij}(t) + \nabla \Delta n_{\varphi_1}^{ij}(t) \tag{2.35}
\end{aligned}$$

The double-superscript denotes the quantities identified with two satellites, and the symbol ∇ is a mnemonic device to emphasize that the difference is made between two points in the sky. The DD L2 pseudorange and phase models are similarly defined. An example of the DD geometry is shown in Fig. 2.3.

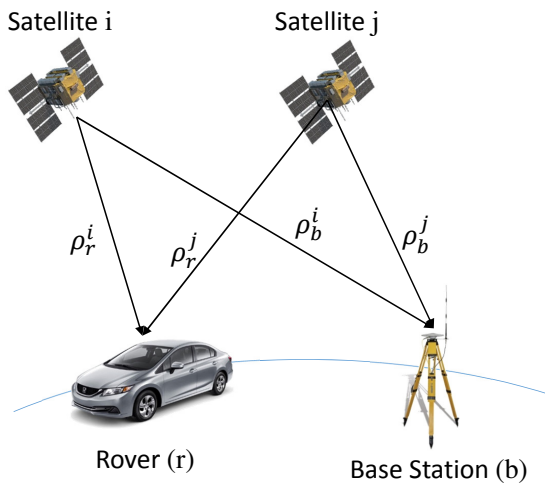


Figure 2.3: Double difference geometry. (Combined image from [6–8].)

While the receiver clock error, $c\Delta\delta t(t)$, is eliminated to first-order, the residual effect due to *time tag bias* on the computation of the range term does not completely cancel. Also, any systematic effects due to un-modeled atmospheric errors are increased slightly by double differencing. Similarly, random errors due to noise or multipath are increased.

Note, DD reduces the phase ambiguity to an integer value represented as $\lambda_1 \nabla \Delta N_1^{ij}(t)$. While the sign of $\lambda_1 \nabla \Delta N_1^{ij}(t)$ is not important, the partial derivative must have a consistent sign.

2.3.4.3 DGPS Triple Differencing

The triple difference (TD) is used to remove the integer ambiguity, thus a TD pseudorange model is ignored. The TD phase model is

$$\begin{aligned}
\delta(t_k, t_{k+1}) \lambda_1 \nabla \Delta \tilde{\varphi}_1^{ij} &= \lambda_1 \nabla \Delta \tilde{\varphi}_1^{ij}(t_k) - \lambda_1 \nabla \Delta \tilde{\varphi}_1^{ij}(t_{k+1}) \\
&= (\nabla \Delta R(\mathbf{p}(t_k), \hat{\mathbf{p}}^{ij}(t_k)) - \nabla \Delta R(\mathbf{p}(t_{k+1}), \hat{\mathbf{p}}^{ij}(t_{k+1}))) \\
&\quad + (\lambda_1 \nabla \Delta N_1^{ij}(t_k) - \lambda_1 \nabla \Delta N_1^{ij}(t_{k+1})) \\
&\quad + (\nabla \Delta T^{ij}(t_k) - \nabla \Delta T^{ij}(t_{k+1})) \\
&\quad - \left(\frac{f_2}{f_1} \nabla \Delta I^{ij}(t_k) - \frac{f_2}{f_1} \nabla \Delta I^{ij}(t_{k+1}) \right) \\
&\quad + (\nabla \Delta M_{\varphi_1}^{ij}(t_k) - \nabla \Delta M_{\varphi_1}^{ij}(t_{k+1})) \\
&\quad + (\nabla \Delta n_{\varphi_1}^{ij}(t_k) - \nabla \Delta n_{\varphi_1}^{ij}(t_{k+1})) \\
&= \delta(t_k, t_{k+1}) \nabla \Delta R(\mathbf{p}, \hat{\mathbf{p}}^{ij}) \\
&\quad + \delta(t_k, t_{k+1}) \nabla \Delta T^{ij} - \delta(t_k, t_{k+1}) \frac{f_2}{f_1} \nabla \Delta I^{ij} \\
&\quad + \delta(t_k, t_{k+1}) \nabla \Delta M_{\varphi_1}^{ij} + \delta(t_k, t_{k+1}) \nabla \Delta n_{\varphi_1}^{ij} \tag{2.36}
\end{aligned}$$

The $\delta(t_k, t_{k+1})$ denotes the quantities identified two epochs. An example of the TD geometry is shown in Fig. 2.4, where the DD observations for two receivers, r and b , observing satellites, i and j , over two successive epochs ($k, k+1$), are used.

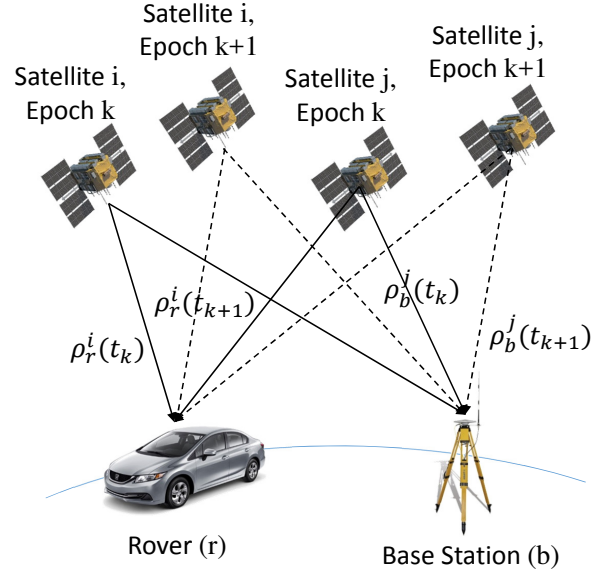


Figure 2.4: Triple difference geometry. (Combined image from [6–8].)

Note that TD only removes the integer ambiguity if the integer has not changed during the time interval between epochs. Any cycle-slips will appear as outliers. While TD introduces time correlations between observations, it is useful for determining the ambiguous integer for DD processing.

Efficient methods for solving the integer ambiguity are presented in [19], [20], and [92]. This dissertation uses [20] because of theoretical similarities to the nonlinear optimization framework presented in Chapter 4. Solving the integer ambiguity is necessary to achieve centimeter-level ground truth accuracy for navigation performance analysis [96].

Chapter 3

Aided Inertial Navigation System

In this chapter, the background and notation for a Global Positioning System (GPS) aided inertial navigation system (INS) [25] is reviewed. To make this dissertation self-contained, this chapter first reviews the INS notation and mechanization. To improve the accuracy and reliability of the INS, aiding is performed using an optimal estimator. It is common to perform optimal estimation using an EKF framework, thus an introduction to the EKF is presented in Section 3.7. Additional accuracy and reliability is achieved through the nonlinear MAP optimization based INS, which is presented in Chapter 4.

3.1 Aided Inertial Navigation

Let $\mathbf{x} \in \mathbb{R}^{n_s}$ denote the rover state vector, where

$$\mathbf{x}(t) = [\mathbf{p}^\top(t), \mathbf{v}^\top(t), \mathbf{q}^\top(t), \mathbf{b}_a^\top(t), \mathbf{b}_g^\top(t)]^\top \in \mathbb{R}^{n_s},$$

where \mathbf{p} , \mathbf{v} , \mathbf{b}_a , \mathbf{b}_g each in \mathbb{R}^3 represent the position, velocity, accelerometer bias and gyro bias vectors, respectively, and $\mathbf{q} \in \mathbb{R}^4$ represents the attitude quaternion ($n_s = 16$), each at

time t .

The kinematic equations for the rover state are

$$\dot{\mathbf{x}}(t) = \mathbf{f}(\mathbf{x}(t), \mathbf{u}(t)), \quad (3.1)$$

where $\mathbf{f} : \mathbb{R}^{n_s} \times \mathbb{R}^6 \mapsto \mathbb{R}^{n_s}$ represents the kinematic model, and $\mathbf{u} \in \mathbb{R}^6$ is the vector of specific forces and angular rates. The function \mathbf{f} is accurately known (see eqns. 11.31-11.33 in [25], derivations specific to this dissertation are provided in Section 3.3). The user applies forces and torques causing accelerations and angular rates which determine $\mathbf{u}(t)$. The kinematic integration of $\mathbf{u}(t)$ through eqn. (3.1) determines $\mathbf{x}(t)$.

Let τ_i denote the time instants of the i^{th} IMU measurements of \mathbf{u} . The IMU measurements are modeled as

$$\tilde{\mathbf{u}}(\tau_i) = \mathbf{u}(\tau_i) - \mathbf{b}(\tau_i) - \boldsymbol{\omega}_u(\tau_i), \quad (3.2)$$

with stochastic errors $\boldsymbol{\omega}_u(\tau_i) \sim \mathcal{N}(\mathbf{0}, \mathbf{Qd})$ and $\mathbf{b} = [\mathbf{b}_a^\top, \mathbf{b}_g^\top]^\top$.

Given the initial condition $\mathbf{x}(t_0) \sim \mathcal{N}(\mathbf{x}_0, \mathbf{P}_0)$ and measurements $\tilde{\mathbf{u}}$, an inertial navigation system propagates an estimate of the vehicle state as the solution of

$$\dot{\hat{\mathbf{x}}}(t) = \mathbf{f}(\hat{\mathbf{x}}(t), \tilde{\mathbf{u}}(t)), \quad (3.3)$$

where $\hat{\mathbf{x}}(t)$ denotes the real-time estimate of $\mathbf{x}(t)$, and $\hat{\mathbf{x}}(0) = x_0$.

Let \mathbf{x}_i and \mathbf{u}_i denote $\mathbf{x}(\tau_i)$ and $\mathbf{u}(\tau_i)$. The solution of eqn. (3.3) over the interval $t \in [\tau_{i-1}, \tau_i]$ from the initial condition $\hat{\mathbf{x}}_{i-1}$ is $\hat{\mathbf{x}}_i \doteq \phi(\hat{\mathbf{x}}_{i-1}, \hat{\mathbf{u}}_{i-1})$, where $\hat{\mathbf{u}}_{i-1} \doteq \tilde{\mathbf{u}}_{i-1} - \hat{\mathbf{b}}_{i-1}$ and

$$\phi(\mathbf{x}_{i-1}, \mathbf{u}_{i-1}) = \mathbf{x}_{i-1} + \int_{\tau_{i-1}}^{\tau_i} \mathbf{f}(\mathbf{x}(\tau), \mathbf{u}(\tau)) d\tau. \quad (3.4)$$

In this dissertation, the equality symbol ‘=’ will be used in its normal sense. The symbol ‘ \doteq ’ will be used to indicate computations that are implemented in software.

Define $\mathbf{U}_{k-1} = \{\tilde{\mathbf{u}}(\tau_i) \text{ for } \tau_i \in [t_{k-1}, t_k]\}$. The integral operator in (3.4) can be iterated for all IMU measurements in \mathbf{U}_{k-1} to propagate the state from t_{k-1} to t_k . Denote this iterative application of eqn. (3.4) as $\hat{\mathbf{x}}_k \doteq \Phi(\hat{\mathbf{x}}_{k-1}, \mathbf{U}_{k-1})$.

3.2 GPS/DGPS Aiding

Let $t_k = kT$ denote the time instants at which GPS measurements are valid, and \mathbf{x}_k denote the state $\mathbf{x}(kT)$ at t_k . It is typically the case that there are numerous IMU measurements available between GPS epochs: $T \gg [\tau_i - \tau_{i-1}]$.

For $(m+1)$ satellites, \mathbf{y}_k represents the double-differenced code (pseudorange) and Doppler measurement vector, as defined in Section 8.8 of [25]. For notational simplicity, it is assumed that the double difference approach removes all common-mode errors (e.g., ionosphere, troposphere, satellite clock and ephemeris errors), as well as the receiver clock biases. The double-differenced measurement vector at t_k is modeled as

$$\mathbf{y}_k = \mathbf{h}_k(\mathbf{x}_k) + \boldsymbol{\eta}_{y,k} + \mathbf{s}_k \quad (3.5)$$

where $\boldsymbol{\eta}_{y,k} = [\boldsymbol{\eta}_{\rho,k}, \boldsymbol{\eta}_{d,k}]$, and $\mathbf{y}_k, \boldsymbol{\eta}_{y,k} \in \mathbb{R}^{2m}$. The symbol $\boldsymbol{\eta}_{\rho,k} \sim \mathcal{N}(\mathbf{0}, \mathbf{R}_{\rho,k})$ represents the pseudorange measurement noise, and $\boldsymbol{\eta}_{d,k} \sim \mathcal{N}(\mathbf{0}, \mathbf{R}_{d,k})$ represents the Doppler measurement noise. Depending on receiver design, environmental factors and the performance of multipath mitigation techniques, the noise level \mathbf{R}_ρ and \mathbf{R}_d can vary for each available satellite. The measurement noise covariance $\mathbf{R} = \text{blkdiag}(\mathbf{R}_\rho, \mathbf{R}_d) \in \mathbb{R}^{2m \times 2m}$.

The symbol $\mathbf{s}_k = [\mathbf{s}_{\rho,k}^\top, \mathbf{s}_{d,k}^\top]^\top \in \mathbb{R}^{2m}$ represents the error due to outliers, where $\mathbf{s}_{\rho,k} = [\mathbf{s}_{\rho,1}, \dots, \mathbf{s}_{\rho,m}]^\top$ and $\mathbf{s}_{d,k} = [\mathbf{s}_{d,1}, \dots, \mathbf{s}_{d,m}]^\top$. Throughout this dissertation, the ability to accommodate outliers will be considered from different perspectives. In Chapter 4, the estimation approach is presented in the ideal case where $\mathbf{s}_k = \mathbf{0}$. In Chapter 6, the ability to detect and remove outliers is considered from the hypothesis testing point-of-view. Alternatively, in Chapter 7, the outliers will be directly accommodated from the Least Soft-thresholded Squares (LSS) perspective.

Using the state estimate, the GPS measurements at t_k are predicted to be $\hat{\mathbf{y}}_k \doteq \mathbf{h}_k(\hat{\mathbf{x}}_k)$. The GPS measurement residual vector is computed as $\delta\mathbf{y}_k \doteq \mathbf{y}_k - \hat{\mathbf{y}}_k$.

3.3 INS Temporal Propagation

3.3.1 Problem Formulation

While many reference frames may be used, the Earth-centered Earth-fixed (ECEF) reference frame is a convenient reference frame for GPS-aided INS. One reason for this choice is that satellite navigation solutions are resolved in the ECEF reference frame. Another is that the ECEF frame works globally, not yielding singularities in the polar regions.

Define the e -frame as the ECEF-frame (or Earth-frame), and the i -frame as the Earth-Centered-Inertial (ECI) frame (or inertial-frame). The direction cosine matrix (DCM), or rotation matrix, from body-frame to Earth-frame is \mathbf{R}_b^e . The position of the body b -frame with respect to the Earth e -frame resolved in the e -frame is \mathbf{r}_{eb}^e . Similarly the velocity of the b -frame with respect to the e -frame resolved in the e -frame is \mathbf{v}_{eb}^e . The rotation matrix from b -frame to e -frame is \mathbf{R}_b^e .

Expanding eqn. (3.1), the INS kinematic equations defining $\mathbf{f}(\mathbf{x}(t), \mathbf{u}(t))$ in the ECEF frame (see Section 11.2.2 of [25]) are

$$\dot{\mathbf{r}}_{eb}^e = \mathbf{v}_{eb}^e \quad (3.6)$$

$$\dot{\mathbf{v}}_{eb}^e = \mathbf{R}_b^e \mathbf{f}_{ib}^b + \mathbf{g}_b^e - 2\Omega_{ie}^e \mathbf{v}_{eb}^e \quad (3.7)$$

$$\dot{\mathbf{R}}_b^e = \mathbf{R}_b^e (\Omega_{ib}^e - \Omega_{ie}^e). \quad (3.8)$$

The inputs \mathbf{u} , are specific force \mathbf{f}_{ib}^b and angular rate $[\omega_{ib}^b \times] = \Omega_{ib}^b$, with respect to the inertial-frame i . The local gravity vector is \mathbf{g}^e , and the Earth-rotation rate is $[\omega_{ie}^e \times] = \Omega_{ie}^e$. The notation $[\mathbf{a} \times]$ represents the skew-symmetric matrix corresponding to the vector \mathbf{a} .

Fig. 3.1 is a block diagram showing how the angular-rate and specific-force measurements, of an Inertial Measurement Unit (IMU), are used to update the Earth-referenced attitude, velocity, and position states at t_i .

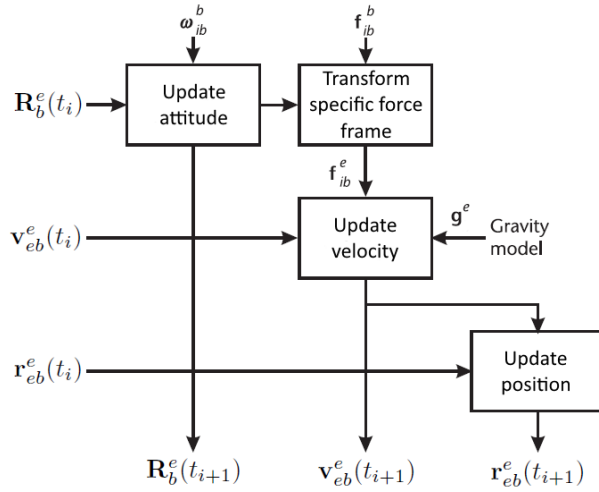


Figure 3.1: Block diagram of the ECEF referenced INS equations.

3.3.2 INS Time Propagation Equations

3.3.2.1 Attitude Update

Using eqn. (2.54) in [25], the time derivative of the rotation matrix \mathbf{R}_b^e is

$$\dot{\mathbf{R}}_b^e = \mathbf{R}_b^e \boldsymbol{\Omega}_{eb}^b, \quad (3.9)$$

where $\boldsymbol{\Omega}_{eb}^b = [\boldsymbol{\omega}_{eb}^b \times]$.

Let the attitude increment over the IMU measurement interval τ_i be defined as $\boldsymbol{\alpha}_{ib}^b = \boldsymbol{\omega}_{ib}^b \tau_i$. Appendix A.1 shows that the discrete-time rotation matrix update that is equivalent to eqn. (3.9) can be computed as

$$\mathbf{R}_b^e(t_{i+1}) = \mathbf{R}_b^e(t_i) \mathbf{R}_{b(t)}^{b(t+\tau_i)} - \boldsymbol{\Omega}_{ie}^b \mathbf{R}_b^e(t_i) \tau_i + \mathbf{R}_b^e(t_i). \quad (3.10)$$

The integrating factor $\mathbf{R}_{b(t)}^{b(t+\tau_i)}$ represents the effect of the angle rotation corresponding to $\boldsymbol{\Omega}_{ib}^b$ over the interval $[t, t + \tau_i]$, and $\mathbf{R}_b^e(t_i)$ and $\mathbf{R}_b^e(t_{i+1})$ are the prior and updated rotation matrix, respectively.

Attitude Increment

The IMU angular rate has two components $\boldsymbol{\omega}_{ib}^b$ and $\boldsymbol{\omega}_{ie}^b$. The body rate portion $\boldsymbol{\omega}_{ib}^b$ can be large and change rapidly, which is the reason its portion of the attitude increment receives special treatment.

By eqn. (2.62) of [25],

$$\mathbf{R}_{b(t)}^{b(t+\tau_i)} = \mathbf{R}_{b-}^{b+} = \exp[\boldsymbol{\alpha}_{ib}^b \times]. \quad (3.11)$$

The power-series expansion of the matrix exponential is

$$\exp[\boldsymbol{\alpha}_{ib}^b \times] = \sum_{r=0}^{\infty} \frac{[\boldsymbol{\alpha}_{ib}^b \times]^r}{r!}. \quad (3.12)$$

As shown in eqns. (2.66) and (2.67) of [25], the odd and even powers of the attitude increment skew-symmetric matrix are,

$$[\boldsymbol{\alpha}_{ib}^b \times]^{2r+1} = (-1)^r \|\boldsymbol{\alpha}_{ib}^b\|^r [\boldsymbol{\alpha}_{ib}^b \times] \quad (3.13)$$

$$[\boldsymbol{\alpha}_{ib}^b \times]^{2r} = (-1)^r \|\boldsymbol{\alpha}_{ib}^b\|^{2r} [\boldsymbol{\alpha}_{ib}^b \times]^2, \quad (3.14)$$

where $r = 1, 2, 3, \dots$. Expanding eqn. (3.11) using eqns. (3.12)-(3.14),

$$\mathbf{R}_{b-}^{b+} = \mathbf{I}_3 + \left(\sum_{r=0}^{\infty} (-1)^r \frac{\|\boldsymbol{\alpha}_{ib}^b\|^{2r}}{(2r+1)!} \right) [\boldsymbol{\alpha}_{ib}^b \times] + \left(\sum_{r=0}^{\infty} (-1)^r \frac{\|\boldsymbol{\alpha}_{ib}^b\|^{2r}}{(2r+2)!} \right) [\boldsymbol{\alpha}_{ib}^b \times]^2. \quad (3.15)$$

Eqn. (3.15) is equivalent to (see eqn. (2.69) of [25], and [85, 86]),

$$\mathbf{R}_{b-}^{b+} = \mathbf{I}_3 + \frac{\sin(\|\boldsymbol{\alpha}_{ib}^b\|)}{\|\boldsymbol{\alpha}_{ib}^b\|} [\boldsymbol{\alpha}_{ib}^b \times] + \frac{1 - \cos(\|\boldsymbol{\alpha}_{ib}^b\|)}{\|\boldsymbol{\alpha}_{ib}^b\|^2} [\boldsymbol{\alpha}_{ib}^b \times]^2. \quad (3.16)$$

When the CPU requires tradeoffs related to implementation, computation of trigonometric functions can be prohibitive. In these cases, the Taylor series expansions may be truncated. For example, the fourth-order approximation of eqn. (3.15) is

$$\mathbf{R}_{b-}^{b+} = \mathbf{I}_3 + \left(1 - \frac{\|\boldsymbol{\alpha}_{ib}^b\|^2}{6} \right) [\boldsymbol{\alpha}_{ib}^b \times] + \left(\frac{1}{2} - \frac{\|\boldsymbol{\alpha}_{ib}^b\|^2}{24} \right) [\boldsymbol{\alpha}_{ib}^b \times]^2. \quad (3.17)$$

Such tradeoffs should be thoroughly evaluated in simulation.

3.3.2.2 Velocity Update

Neglecting acceleration in the ECEF frame, assume the ECI frame instantaneously coincides with the ECEF frame, such that $\ddot{\mathbf{r}}_{ib}^e = \ddot{\mathbf{r}}_{eb}^e$, $\dot{\mathbf{r}}_{ib}^e = \dot{\mathbf{r}}_{eb}^e$, and $\mathbf{r}_{ib}^e = \mathbf{r}_{eb}^e$. The velocity update in the ECEF frame is

$$\mathbf{v}_{eb}^e(t_{i+1}) = \mathbf{v}_{eb}^e(t_i) + (\mathbf{f}_{ib}^e + \mathbf{g}_b^e(\mathbf{r}_{eb}^e(t_i)) - 2\boldsymbol{\Omega}_{ie}^e \mathbf{v}_{eb}^e(t_i)) \tau_i \quad (3.18)$$

where $\mathbf{r}_{eb}^e(t_i)$ and $\mathbf{v}_{eb}^e(t_i)$ are the prior position and velocity, respectively, and $\mathbf{v}_{eb}^e(t_{i+1})$ is the updated velocity for the IMU interval τ_i .

Specific-Force Frame Transformation

The frame transformation of specific-force takes the form

$$\mathbf{f}_{ib}^e = \mathbf{R}_b^e \mathbf{f}_{ib}^b. \quad (3.19)$$

Incorporating the updated rotation matrix $\mathbf{R}_b^e(t_{i+1})$ from eqn. (3.10), the specific force transformation is

$$\mathbf{f}_{ib}^e = \mathbf{R}_b^e(t_{i+1}) \mathbf{f}_{ib}^b. \quad (3.20)$$

3.3.2.3 Position Update

Using eqn. (3.6), the position update is derived as follows:

$$\mathbf{r}_{eb}^e(t_{i+1}) = \mathbf{r}_{eb}^e(t_i) + (\mathbf{v}_{eb}^e(t_i) + \mathbf{v}_{eb}^e(t_{i+1})) \frac{\tau_i}{2}, \quad (3.21)$$

$$= \mathbf{r}_{eb}^e(t_i) + \mathbf{v}_{eb}^e(t_i) \tau_i + (\mathbf{f}_{ib}^e + \mathbf{g}^e(\mathbf{r}_{eb}^e(t_i)) - 2\boldsymbol{\Omega}_{ie}^e \mathbf{v}_{eb}^e(t_i)) \frac{\tau_i^2}{2}. \quad (3.22)$$

where $\mathbf{r}_{eb}^e(t_i)$ and $\mathbf{r}_{eb}^e(t_{i+1})$ are the prior and updated positions, respectively.

3.3.2.4 Gravity Model

A precise gravity model [98] formulated in the ECEF frame, is defined as

$$\boldsymbol{\gamma}_{ib}^e = -\frac{\mu}{||\mathbf{r}_{eb}^e||^3} \times \left\{ \mathbf{r}_{eb}^e + \frac{3}{2} J_2 \frac{R_0^2}{||\mathbf{r}_{eb}^e||^2} \begin{bmatrix} (1 - 5(\mathbf{r}_{eb,z}^e)^2 / ||\mathbf{r}_{eb}^e||) \mathbf{r}_{eb,x}^e \\ (1 - 5(\mathbf{r}_{eb,z}^e)^2 / ||\mathbf{r}_{eb}^e||) \mathbf{r}_{eb,y}^e \\ (3 - 5(\mathbf{r}_{eb,z}^e)^2 / ||\mathbf{r}_{eb}^e||) \mathbf{r}_{eb,z}^e \end{bmatrix} \right\}, \quad (3.23)$$

where the Earth's second gravitational constant $J_2 = 1.082627E^{-3}$ (m^3/s^2), the Equatorial radius is $R_0 = 6.378137E^{+6}$ (m), the gravitational constant $\mu = 3.986004418E^{+14}$ (m^3/s^2), and the Earth-rotation rate is $\omega_{ie} = 7.292115E^{-5}$ (rad/s).

3.4 State Correction

3.4.1 Problem Formulation

Let $\hat{\mathbf{x}} \in \mathbb{R}^{n_s}$ denote the estimate of the rover state vector:

$$\hat{\mathbf{x}}(t) = [\hat{\mathbf{p}}^\top(t), \hat{\mathbf{v}}^\top(t), \hat{\mathbf{q}}^\top(t), \hat{\mathbf{b}}_a^\top(t), \hat{\mathbf{b}}_g^\top(t)]^\top \in \mathbb{R}^{n_s}.$$

The error between $\mathbf{x}(t)$ and $\hat{\mathbf{x}}(t)$ is denoted as $\delta\mathbf{x}$. The error vector is

$$\delta\mathbf{x} = [\delta\mathbf{p}^\top, \delta\mathbf{v}^\top, \boldsymbol{\rho}^\top, \delta\mathbf{b}_a^\top, \delta\mathbf{b}_g^\top]^\top \in \mathbb{R}^{n_e},$$

where $\delta\mathbf{p}$ and $\delta\mathbf{v}$, each in \mathbb{R}^3 , represent the error between the true and computed position and velocity, respectively. The small-angle error state, denoted as $\boldsymbol{\rho} \in \mathbb{R}^{3 \times 1}$, is defined in Section 2.5.5 of [25], and discussed in Section 3.4.3. The errors $\delta\mathbf{b}_a$ and $\delta\mathbf{b}_g$, each in \mathbb{R}^3 , represent the accelerometer bias, and gyro bias errors, respectively. Therefore $\delta\mathbf{x} \in \mathbb{R}^{15}$ (i.e. $n_e = 15$). The fact that $n_s = 16$ and $n_e = 15$ is discussed in Section 3.4.3.

Let $\delta\hat{\mathbf{x}}$ denote an estimate of $\delta\mathbf{x}$. The state correction to the state vector $\hat{\mathbf{x}}$ is denoted as

$$\hat{\mathbf{x}}^+ = \hat{\mathbf{x}}^- \oplus \delta\hat{\mathbf{x}}.$$

The symbol $(-)$ denotes the prior estimate, whereas $(+)$ is the updated estimate. The symbol \oplus is discussed in Sections 3.4.2 and 3.4.3

3.4.2 Position, Velocity, and Bias Updates

Position, velocity, accelerometer bias and gyro bias, each have corrections which are additive. The state correction step is

$$\hat{\mathbf{p}}^+ = \hat{\mathbf{p}}^- + \delta\mathbf{p}$$

$$\hat{\mathbf{v}}^+ = \hat{\mathbf{v}}^- + \delta\mathbf{v}$$

$$\hat{\mathbf{b}}_a^+ = \hat{\mathbf{b}}_a^- + \delta\mathbf{b}_a$$

$$\hat{\mathbf{b}}_g^+ = \hat{\mathbf{b}}_g^- + \delta\mathbf{b}_g.$$

3.4.3 Attitude Update

When the attitude error is sufficiently small (see Section 2.5.5 of [25]), the attitude can be represented as a set of small-angle planar rotations $\{\rho_x, \rho_y, \rho_z\}$ about three orthogonal axes $\{x, y, z\}$, thus the attitude error can be defined in \mathbb{R}^3 .

3.4.3.1 Rotation Matrix

Let $\mathbf{R}_b^n \in \mathbb{R}^{3 \times 3}$ represent the true rotation from body-frame (b) to navigation-frame (n) that is equivalent to $\mathbf{q}(t)$ (see eqn. D.13 in [25]). Let $\hat{\mathbf{R}}_b^n \in \mathbb{R}^{3 \times 3}$ represent the computed rotation that is equivalent to $\hat{\mathbf{q}}(t)$. The error between the true and computed rotation is

$$\mathbf{R}_{\hat{n}}^n = (\mathbf{R}_b^n)(\hat{\mathbf{R}}_b^n),$$

where $\mathbf{R}_{\hat{n}}^n$ represents the rotation matrix from the computed to actual navigation frame.

When the error between the true and computed rotation is zero, then $\mathbf{R}_{\hat{n}}^n = \mathbf{I}$. Otherwise,

as discussed in Section 2.6.1 of [25],

$$\mathbf{R}_{\hat{n}}^n = [\mathbf{I} - \mathbf{P}]$$

where $\mathbf{P} = [\boldsymbol{\rho} \times]$, and $\boldsymbol{\rho} = [\rho_x, \rho_y, \rho_z]^\top \in \mathbb{R}^3$ (see eqn. 10.28 of [25]).

Using this notation, the attitude update (as defined in eqn. 10.29 of [25]) is

$$(\mathbf{R}_b^n)^+ = [\mathbf{I} - \mathbf{P}](\hat{\mathbf{R}}_b^n)^-.$$

Note that the attitude correction is multiplicative.

3.4.3.2 Quaternion

A similar approach to Section 3.4.3.1 is valid when the attitude error is represented by a quaternion. Let \mathbf{q}_b^n represent the true quaternion from b -frame to n -frame. Let $\hat{\mathbf{q}}_b^n$ represent the computed quaternion. The error may be represented as

$$\mathbf{q}_n^n = \mathbf{q}_b^n \otimes \hat{\mathbf{q}}_n^n$$

where $\mathbf{q}_{\hat{n}}^n$ represents the quaternion from the computed to actual navigation frame. The symbol \otimes represents the quaternion multiplication operation defined in Section D of [25].

When the error between the true and computed rotation is zero, then $\mathbf{q}_{\hat{n}}^n = [1, 0, 0, 0]^\top$, otherwise $\mathbf{q}_{\hat{n}}^n$ may be represented as

$$\mathbf{q}_{\hat{n}}^n = \begin{bmatrix} \hat{\mathbf{q}}_s \\ \hat{\mathbf{q}}_v \end{bmatrix} = \begin{bmatrix} \sqrt{1 - \left\| \frac{1}{2}\boldsymbol{\rho} \right\|_2^2} \\ \frac{1}{2}\boldsymbol{\rho} \end{bmatrix} \approx \begin{bmatrix} 1 \\ \frac{1}{2}\boldsymbol{\rho} \end{bmatrix}, \quad (3.24)$$

where the scalar part of the quaternion is $\hat{\mathbf{q}}_s = 1$, and the vector part is $\hat{\mathbf{q}}_v = \boldsymbol{\rho}$. The approximation on the right-hand side of eqn. (3.24) is derived in Appendix A.2.

Using this notation, the multiplicative quaternion update is

$$\hat{\mathbf{q}}_b^n{}^+ = \mathbf{q}_{\hat{n}}^n \otimes \hat{\mathbf{q}}_b^n{}^-.$$

Quaternion operations are defined in Section D of [25].

3.5 INS Error Model

Due to initial condition errors, system calibration errors, and measurement noise, estimation error develops over time such that $\mathbf{x}(t)$ are not equal $\hat{\mathbf{x}}(t)$. The error state vector is

$$\delta\mathbf{x} = [\delta\mathbf{p}^\top, \delta\mathbf{v}^\top, \delta\boldsymbol{\theta}^\top, \delta\mathbf{b}_a^\top, \delta\mathbf{b}_g^\top]^\top \in \mathbb{R}^{n_e},$$

where $\delta\mathbf{p}$, $\delta\mathbf{v}$, $\delta\boldsymbol{\theta}$, $\delta\mathbf{b}_a$, and $\delta\mathbf{b}_g$ each in \mathbb{R}^3 are the position, velocity, attitude, accelerometer bias and gyro bias error vectors, respectively.

The error state $\delta\mathbf{x}(t)$ is related to $\mathbf{x}(t)$ and $\hat{\mathbf{x}}(t)$ by $\delta\mathbf{x}(t) = \mathbf{x}(t) \ominus \hat{\mathbf{x}}(t)$. The symbol ‘ \ominus ’, which is similar to the discussion in Section 3.4, represents the subtraction operation for position, velocity and bias states, and the multiplication operation of the attitude states. The fact that $n_s = 16$ and $n_e = 15$ is discussed in Section 3.4. The dynamics and stochastic properties of this estimation error vector are well understood, and can be found in Section 11.4 of [25]. The derivation and definitions of linear state transition error model is presented in Section 3.6.

3.6 INS Noise Propagation

3.6.1 Problem Formulation

Let $\mathbf{x}_v(t) = [\mathbf{p}^\top(t), \mathbf{v}^\top(t), \mathbf{q}^\top(t)]^\top \in \mathbb{R}^{10}$ represent the vehicle state comprised of position, velocity and attitude. Let $\mathbf{x}_c(t) = [\mathbf{b}_a^\top(t), \mathbf{b}_g^\top(t)]^\top \in \mathbb{R}^6$ represent the IMU calibration terms: accelerometer bias and gyro bias. Then $\mathbf{x}(t)$ can be represented as $\mathbf{x}(t) = [\mathbf{x}_v^\top(t), \mathbf{x}_c^\top(t)]^\top$.

Let τ_i denote the time instants of the i^{th} IMU measurements of \mathbf{u} , as defined in Section 3.1. Let $\mathbf{x}_i = \mathbf{x}(\tau_i)$ and $\mathbf{u}_i = \mathbf{u}(\tau_i)$.

Let the state estimate time propagation be represented as

$$\hat{\mathbf{x}}_{i+1} \doteq \phi(\hat{\mathbf{x}}_i, \tilde{\mathbf{u}}_i),$$

where the vehicle state estimate is $\hat{\mathbf{x}}_{v,i+1} \doteq \phi_v(\hat{\mathbf{x}}_{v,i}, \tilde{\mathbf{u}}_i)$.

Let the true state time propagation be represented as

$$\mathbf{x}_{i+1} = \phi(\mathbf{x}_i, \mathbf{u}_i),$$

and the true vehicle state as $\mathbf{x}_{v,i+1} = \phi_v(\mathbf{x}_{v,i}, \mathbf{u}_i)$.

Define the state error as

$$\delta\mathbf{x}_i = \mathbf{x}_i \ominus \hat{\mathbf{x}}_i \in \mathbb{R}^{n_e},$$

where the symbol ‘ \ominus ’ is discussed in Section 3.5. Let $\delta\mathbf{x}_{v,i} \in \mathbb{R}^9$ represent the vehicle state error for position, velocity and attitude. Let $\delta\mathbf{x}_{c,i} \in \mathbb{R}^6$ represent the error in the IMU calibration terms: accelerometer bias and gyro bias. Then $\delta\mathbf{x}_i$ can be represented as

$$\delta\mathbf{x}_i = [\delta\mathbf{x}_{v,i}^\top, \delta\mathbf{x}_{c,i}^\top]^\top.$$

Let the IMU measurement be defined as

$$\tilde{\mathbf{u}}(\tau_i) \triangleq \mathbf{u}(\tau_i) - \mathbf{b}(\tau_i) - \boldsymbol{\omega}_u(\tau_i) \in \mathbb{R}^6,$$

with additive stochastic errors $\boldsymbol{\omega}_u(\tau_i) \sim \mathcal{N}(\mathbf{0}, \mathbf{Q}_d)$ and $\mathbf{b} = [\mathbf{b}_a^\top, \mathbf{b}_g^\top]^\top$. The sensor bias \mathbf{b} represents time correlated measurement errors, and $\boldsymbol{\omega}_u(\tau_i)$ represents the white measurement errors. Let the estimate $\hat{\mathbf{u}}_i \triangleq \tilde{\mathbf{u}}_i + \hat{\mathbf{b}}_i$, where $\hat{\mathbf{b}}_i$ is the estimate of \mathbf{b}_i (i.e. $\hat{\mathbf{x}}_{c,i}$). Let the measurements $\tilde{\mathbf{u}}(\tau_i)$ be defined for IMU measurement times i , between aiding measurement times k , such that $\tau_i \in [t_{k-1}, t_k]$.

Define

$$\begin{aligned}\delta\mathbf{u}_i &\triangleq \mathbf{u}_i - \hat{\mathbf{u}}_i \\ &= \mathbf{u}_i - \tilde{\mathbf{u}}_i - \hat{\mathbf{b}}_i \\ &= \mathbf{u}_i - (\mathbf{u}_i - \mathbf{b}_i - \boldsymbol{\omega}_{u,i}) - \hat{\mathbf{b}}_i \\ &= \delta\mathbf{b}_i + \boldsymbol{\omega}_{u,i},\end{aligned}$$

where $\delta\mathbf{b}_i \triangleq \mathbf{b}_i - \hat{\mathbf{b}}_i$, and $\delta\mathbf{b}_i$ (i.e. $\delta\mathbf{b}_i = \delta\mathbf{x}_{c,i}$) is a state calibration term.

Linearization of the state error, using Taylor series to first order, yields

$$\begin{aligned}\delta\mathbf{x}_{v,i+1} &= \phi_v(\mathbf{x}_{v,i}, \mathbf{u}_i) - \phi_v(\hat{\mathbf{x}}_{v,i}, \hat{\mathbf{u}}_i) \\ &= \phi_v(\hat{\mathbf{x}}_{v,i}, \hat{\mathbf{u}}_i) + \frac{\partial\phi_v}{\partial\mathbf{x}_{v,i}} \Big|_{\hat{\mathbf{x}}_{v,i}} \delta\mathbf{x}_{v,i} + \frac{\partial\phi_v}{\partial\mathbf{u}_i} \Big|_{\hat{\mathbf{u}}_i} \delta\mathbf{u}_i - \phi_v(\hat{\mathbf{x}}_{v,i}, \hat{\mathbf{u}}_i) \\ &= \frac{\partial\phi_v}{\partial\mathbf{x}_{v,i}} \Big|_{\hat{\mathbf{x}}_{v,i}} \delta\mathbf{x}_{v,i} + \frac{\partial\phi_v}{\partial\mathbf{u}_i} \Big|_{\hat{\mathbf{u}}_i} \delta\mathbf{u}_i \\ &= \mathbf{A}_i \delta\mathbf{x}_{v,i} + \mathbf{B}_i \delta\mathbf{u}_i \\ &= \mathbf{A}_i \delta\mathbf{x}_{v,i} + \mathbf{B}_i \delta\mathbf{b}_i + \mathbf{B}_i \boldsymbol{\omega}_{u,i},\end{aligned}\tag{3.25}$$

where $\mathbf{A}_i = \frac{\partial\phi_v}{\partial\mathbf{x}_{v,i}} \Big|_{\hat{\mathbf{x}}_{v,i}, \hat{\mathbf{u}}_i} \in \mathbb{R}^{9 \times 9}$, and $\mathbf{B}_i = \frac{\partial\phi_v}{\partial\mathbf{u}_i} \Big|_{\hat{\mathbf{x}}_{v,i}, \hat{\mathbf{u}}_i} \in \mathbb{R}^{9 \times 6}$.

Let the model of the sensor bias be defined as a first-order Gauss-Markov process

$$\delta \mathbf{b}_{i+1} = \mathbf{F}_b \delta \mathbf{b}_i + \boldsymbol{\nu}, \quad (3.26)$$

where $\mathbf{F}_b \in \mathbb{R}^{6 \times 6}$ is selected such that the bias errors are modeled as either random constants or random walk plus constants (see eqns. 11.106 and 11.107 of [25]), and $\boldsymbol{\nu} \sim \mathcal{N}(\mathbf{0}, \sigma_\nu \mathbf{I})$.

Rewriting eqns. (3.25) and (3.26) in matrix form:

$$\begin{bmatrix} \delta \mathbf{x}_{v,i+1} \\ \delta \mathbf{x}_{c,i+1} \end{bmatrix} = \begin{bmatrix} \mathbf{A}_i & \mathbf{B}_i \\ \mathbf{0} & \mathbf{F}_b \end{bmatrix} \begin{bmatrix} \delta \mathbf{x}_{v,i} \\ \delta \mathbf{b}_i \end{bmatrix} + \begin{bmatrix} \mathbf{B}_i & \mathbf{0} \\ \mathbf{0} & \mathbf{I} \end{bmatrix} \begin{bmatrix} \boldsymbol{\omega}_{u,i} \\ \boldsymbol{\nu} \end{bmatrix}. \quad (3.27)$$

For analysis, in the following section let $\mathbf{F}_b = \mathbf{I}$.

3.6.2 Propagation of State Error

This section analyzes the error accumulation over the time interval $t \in [k-1, k]$ using superposition.

3.6.2.1 Propagation of Initial State Error

Consider eqn. (3.27) over the interval $t \in [k-1, k]$, where $\boldsymbol{\omega}_{u,i-1} = \mathbf{0}$ and $\boldsymbol{\nu} = \mathbf{0}$. Without loss of generality let $k = 1$, such that $t \in [0, 1]$. For each time instant, eqn. (3.27)

can be represented in terms of \mathbf{A}_i , and \mathbf{B}_i , with initial condition errors $\delta\mathbf{x}_{v,0}$, and $\delta\mathbf{b}_0$:

$$\begin{aligned}
 \delta\mathbf{x}_1 &= \begin{bmatrix} \mathbf{A}_0 & \mathbf{B}_0 \\ \mathbf{0} & \mathbf{I} \end{bmatrix} \begin{bmatrix} \delta\mathbf{x}_{v,0} \\ \delta\mathbf{b}_0 \end{bmatrix} \\
 \delta\mathbf{x}_2 &= \begin{bmatrix} \mathbf{A}_1 & \mathbf{B}_1 \\ \mathbf{0} & \mathbf{I} \end{bmatrix} \begin{bmatrix} \delta\mathbf{x}_{v,1} \\ \delta\mathbf{b}_1 \end{bmatrix} \\
 &= \begin{bmatrix} \mathbf{A}_1 & \mathbf{B}_1 \\ \mathbf{0} & \mathbf{I} \end{bmatrix} \begin{bmatrix} \mathbf{A}_0 & \mathbf{B}_0 \\ \mathbf{0} & \mathbf{I} \end{bmatrix} \begin{bmatrix} \delta\mathbf{x}_{v,0} \\ \delta\mathbf{b}_0 \end{bmatrix} \\
 &= \begin{bmatrix} \mathbf{A}_1\mathbf{A}_0 & \mathbf{A}_1\mathbf{B}_0 + \mathbf{B}_1 \\ \mathbf{0} & \mathbf{I} \end{bmatrix} \begin{bmatrix} \delta\mathbf{x}_{v,0} \\ \delta\mathbf{b}_0 \end{bmatrix} \\
 \delta\mathbf{x}_3 &= \begin{bmatrix} \mathbf{A}_2 & \mathbf{B}_2 \\ \mathbf{0} & \mathbf{I} \end{bmatrix} \begin{bmatrix} \delta\mathbf{x}_{v,2} \\ \delta\mathbf{b}_2 \end{bmatrix} \\
 &= \begin{bmatrix} \mathbf{A}_2 & \mathbf{B}_2 \\ \mathbf{0} & \mathbf{I} \end{bmatrix} \begin{bmatrix} \mathbf{A}_1\mathbf{A}_0 & \mathbf{A}_1\mathbf{B}_0 + \mathbf{B}_1 \\ \mathbf{0} & \mathbf{I} \end{bmatrix} \begin{bmatrix} \delta\mathbf{x}_{v,0} \\ \delta\mathbf{b}_0 \end{bmatrix} \\
 &= \begin{bmatrix} \mathbf{A}_2\mathbf{A}_1\mathbf{A}_0 & \mathbf{A}_2\mathbf{A}_1\mathbf{B}_0 + \mathbf{A}_2\mathbf{B}_1 + \mathbf{B}_2 \\ \mathbf{0} & \mathbf{I} \end{bmatrix} \begin{bmatrix} \delta\mathbf{x}_{v,0} \\ \delta\mathbf{b}_0 \end{bmatrix}. \tag{3.28}
 \end{aligned}$$

Define F_s as the sample frequency of the sensor (e.g. IMU). Let $\mathbf{U}_k = \{\tilde{\mathbf{u}}(\tau_i)\}$ for $\tau_i \in [t_{k-1}, t_k]\}$. Let $\mathbf{X}_k = [\mathbf{x}(t_{k-L})^\top, \dots, \mathbf{x}(t_k)^\top]^\top \in \mathbb{R}^{n_s(L+1)}$ denote the vehicle trajectory over a sliding time window that contains L one second GPS measurement epochs: $[\mathbf{y}_{k-L+1}, \dots, \mathbf{y}_k]$.

After F_s IMU time steps (i.e. $F_{s,k=1}$)

$$\delta\mathbf{x}_{F_s} = \left\{ \prod_{i=1}^{F_s} \begin{bmatrix} \mathbf{A}_i & \mathbf{B}_i \\ \mathbf{0} & \mathbf{I} \end{bmatrix} \right\} \begin{bmatrix} \delta\mathbf{x}_{v,0} \\ \delta\mathbf{b}_0 \end{bmatrix} \quad (3.29)$$

$$= \boldsymbol{\Upsilon}(\hat{\mathbf{X}}_k, \mathbf{U}_k)[\delta\mathbf{x}_{v,0}, \delta\mathbf{b}_0]^\top, \quad (3.30)$$

where the operator $\boldsymbol{\Upsilon}(\hat{\mathbf{X}}_k, \mathbf{U}_k)$ in eqn. (3.30) represents the product operation in eqn. (3.29), and $\hat{\mathbf{X}}_k$ is the estimate of \mathbf{X}_k . The product operation in eqn. (3.29) must follow the order of multiplications shown in eqn. (3.28).

3.6.2.2 Noise Propagation

Again consider eqn. (3.27) over the interval $t \in [k-1, k]$. Now analyze the effect of the noise terms $\boldsymbol{\omega}_u$ and $\boldsymbol{\nu}$, with $\delta\mathbf{x}_{v,0}$ and $\delta\mathbf{b}_0$ both zero.

To simplify notation, let

$$\mathbf{C}_i \triangleq \begin{bmatrix} \mathbf{A}_i & \mathbf{B}_i \\ \mathbf{0} & \mathbf{I} \end{bmatrix}, \quad \mathbf{D}_i \triangleq \begin{bmatrix} \mathbf{B}_i & \mathbf{0} \\ \mathbf{0} & \mathbf{I} \end{bmatrix},$$

and

$$\delta\mathbf{x}_i \triangleq \begin{bmatrix} \delta\mathbf{x}_{v,i} \\ \delta\mathbf{x}_{c,i} \end{bmatrix}, \quad \mathbf{n}_i \triangleq \begin{bmatrix} \boldsymbol{\omega}_{u,i} \\ \boldsymbol{\nu} \end{bmatrix}.$$

Defining eqn. (3.27) using the terms above,

$$\delta\mathbf{x}_{i+1} = \mathbf{C}_i \delta\mathbf{x}_i + \mathbf{D}_i \mathbf{n}_i. \quad (3.31)$$

Performing operations on eqn. (3.31) (similar to the operations leading up to eqn. (3.28)),

$$\begin{aligned}
\delta \mathbf{x}_1 &= \mathbf{C}_0 \delta \mathbf{x}_0 + \mathbf{D}_0 \mathbf{n}_0 \\
\delta \mathbf{x}_2 &= \mathbf{C}_1 \delta \mathbf{x}_1 + \mathbf{D}_1 \mathbf{n}_1 \\
&= \mathbf{C}_1 (\mathbf{C}_0 \delta \mathbf{x}_0 + \mathbf{D}_0 \mathbf{n}_0) + \mathbf{D}_1 \mathbf{n}_1 \\
&= \mathbf{C}_1 \mathbf{C}_0 \delta \mathbf{x}_0 + \mathbf{C}_1 \mathbf{D}_0 \mathbf{n}_0 + \mathbf{D}_1 \mathbf{n}_1 \\
\delta \mathbf{x}_3 &= \mathbf{C}_2 \delta \mathbf{x}_2 + \mathbf{D}_2 \mathbf{n}_2 \\
&= \mathbf{C}_2 (\mathbf{C}_1 \mathbf{C}_0 \delta \mathbf{x}_0 + \mathbf{C}_1 \mathbf{D}_0 \mathbf{n}_0 + \mathbf{D}_1 \mathbf{n}_1) + \mathbf{D}_2 \mathbf{n}_2 \\
&= \mathbf{C}_2 \mathbf{C}_1 \mathbf{C}_0 \delta \mathbf{x}_0 + \mathbf{C}_2 \mathbf{C}_1 \mathbf{D}_0 \mathbf{n}_0 + \mathbf{C}_2 \mathbf{D}_1 \mathbf{n}_1 + \mathbf{D}_2 \mathbf{n}_2. \tag{3.32}
\end{aligned}$$

For $i = F_s$, and $\delta \mathbf{x}_0 = \mathbf{0}$, the terms in eqn. (3.32) can be defined as

$$\begin{aligned}
\mathbf{w}_{k-1} &= \left\{ \sum_{i=0}^{F_s-2} \left(\prod_{j=i+1}^{F_s-1} \mathbf{C}_j \right) \mathbf{D}_i \mathbf{n}_i \right\} + \mathbf{D}_{F_s-1} \mathbf{n}_{F_s-1} \\
&= \boldsymbol{\Gamma} \boldsymbol{\eta}.
\end{aligned} \tag{3.33}$$

Let the product of \mathbf{C}_j in eqn. (3.33) be defined as

$$\mathbf{C}_j^p \triangleq \begin{cases} \prod_{j=q}^p \mathbf{C}_j = \mathbf{C}_p \cdots \mathbf{C}_{q-1} \mathbf{C}_q & \text{for } q \neq p \\ \mathbf{C}_q & \text{for } q = p \end{cases} \tag{3.34}$$

where product operation in eqn. (3.34) must follow the order of operations shown in eqn. (3.32). Let $\boldsymbol{\Gamma}$ and $\boldsymbol{\eta}$ be defined as

$$\begin{aligned}
\boldsymbol{\Gamma} &\triangleq \left[\mathbf{C}_1^{F_s-1} \mathbf{D}_0, \mathbf{C}_2^{F_s-1} \mathbf{D}_1, \dots, \mathbf{C}_{F_s-1}^{F_s-1} \mathbf{D}_{F_s-2}, \mathbf{D}_{F_s-1} \right] \\
\boldsymbol{\eta} &\triangleq [\mathbf{n}_0, \mathbf{n}_1, \dots, \mathbf{n}_{F_s-1}].
\end{aligned}$$

3.6.2.3 Summary

Combining the results from Sections 3.6.2.1 and 3.6.2.2, the linear state transition error model over $t \in [t_{k-1}, t_k]$ is

$$\delta \mathbf{x}_k = \boldsymbol{\Upsilon}_{k-1} \delta \mathbf{x}_{k-1} + \mathbf{w}_{k-1}. \quad (3.35)$$

with

$$\begin{aligned} \mathbf{Q}_{\mathbf{D}} &= \text{Cov}(\mathbf{w}_{k-1}) \in \mathbb{R}^{n_e \times n_e} \\ &= E \langle \boldsymbol{\Gamma} \boldsymbol{\eta} \boldsymbol{\eta}^T \boldsymbol{\Gamma}^T \rangle \\ &= E \left\langle \boldsymbol{\Gamma} \begin{bmatrix} \boldsymbol{\eta}_0 \\ \boldsymbol{\eta}_1 \\ \vdots \\ \boldsymbol{\eta}_{F_s-1} \end{bmatrix} [\boldsymbol{\eta}_0 \ \boldsymbol{\eta}_1 \ \cdots \ \boldsymbol{\eta}_{F_s-1}] \boldsymbol{\Gamma}^T \right\rangle \\ &= \boldsymbol{\Gamma} \begin{bmatrix} \mathbf{Q}_{\mathbf{d},0} & & \\ & \ddots & \\ & & \mathbf{Q}_{\mathbf{d},F_s-1} \end{bmatrix} \boldsymbol{\Gamma}^T, \end{aligned} \quad (3.36)$$

where $\mathbf{Q}_{\mathbf{d},i} = \boldsymbol{\eta}_i \boldsymbol{\eta}_i^T$. The stochastic properties of eqn. (3.36) are well understood, and can be found in Sections 4.7 and 7.2.5.2 of [25].

3.7 Extended Kalman Filtering for GPS-aided INS

When GPS aiding measurements of the form (repeating eqn. (3.5) for clarity)

$$\tilde{\mathbf{y}}(t) = \mathbf{h}(\mathbf{x}(t)) + \boldsymbol{\eta}_y(t), \quad \boldsymbol{\eta}_y \sim \mathcal{N}(\mathbf{0}, \mathbf{R}_y), \quad (3.37)$$

are available, various methods use the initial state, inertial measurements, and aiding measurement information to estimate the vehicle state vector [18, 25, 59]. The Extended Kalman Filter (EKF) is a widely used method in aided INS, due to its implementation simplicity and real-time efficiency [26].

The standard EKF can be reformulated in Weighted Least Square (WLS) form [25, 26, 48]. Given the INS prior and the aiding measurements at time step t_k ,

$$\hat{\mathbf{x}}_k^- = \mathbf{x}_k + \delta\mathbf{x}_k^-, \quad \delta\mathbf{x}_k^- \sim \mathcal{N}(\mathbf{0}, \mathbf{P}_k^-), \quad (3.38)$$

$$\tilde{\mathbf{y}}_k = \mathbf{h}_k(\mathbf{x}_k) + \boldsymbol{\eta}_k, \quad \boldsymbol{\eta}_k \sim \mathcal{N}(\mathbf{0}, \mathbf{R}_k), \quad (3.39)$$

where the process noise \mathbf{w}_k and the measurement noise \mathbf{n}_k [18, 25, 59] are assumed White-Gaussian-Noise (WGN). A *Maximum Likelihood* estimation of the state correction $\delta\mathbf{x}_k$ at t_k can be formulated as

$$\delta\mathbf{x}_k^+ = \underset{\delta\mathbf{x}_k}{\arg\max} \left\{ p_{\delta\mathbf{x}_k^-}(\delta\mathbf{x}_k) p_{\mathbf{n}_k}(\tilde{\mathbf{y}}_k - \mathbf{H}_k \hat{\mathbf{x}}_k^- - \mathbf{H}_k \delta\mathbf{x}_k) \right\}, \quad (3.40)$$

where $\mathbf{H}_k = \frac{\partial \mathbf{h}_k}{\partial \mathbf{x}}|_{\mathbf{x}=\hat{\mathbf{x}}_k^-}$ is the Jacobian matrix of the measurement model evaluated at the INS prior $\hat{\mathbf{x}}_k^-$.

A Least Square problem can be derived by evaluating the negative log-likelihood of the right hand side of eqn. (3.40),

$$\delta\mathbf{x}_k^+ = \underset{\delta\mathbf{x}_k}{\arg\min} \left\{ \|\delta\mathbf{x}_k\|_{\mathbf{P}_k^-}^2 + \|\delta\mathbf{y}_k - \mathbf{H}_k \delta\mathbf{x}_k\|_{\mathbf{R}_k}^2 \right\}, \quad (3.41)$$

where $\delta\mathbf{y}_k \triangleq \tilde{\mathbf{y}}_k - \mathbf{H}_k \hat{\mathbf{x}}_k^-$ is the measurement residual (i.e. innovation) and the notation $\|\mathbf{x}\|_{\mathbf{C}}^2 \triangleq \mathbf{x}^\top \mathbf{C}^{-1} \mathbf{x}$ is defined as the squared Mahalanobis distance.

Let

$$\mathbf{A}_k = \begin{bmatrix} \mathbf{I} \\ \mathbf{H}_k \end{bmatrix}, \quad \mathbf{C}_k = \begin{bmatrix} \mathbf{P}_k^- & \mathbf{0} \\ \mathbf{0} & \mathbf{R}_k \end{bmatrix} \quad \text{and} \quad \delta \mathbf{Y}_k = \begin{bmatrix} \mathbf{0} \\ \delta \mathbf{y}_k \end{bmatrix},$$

the Kalman Filter measurement update can be derived by solving a Weighted Least Square problem:

$$\min_{\delta \mathbf{x}} \| \delta \mathbf{Y}_k - \mathbf{A}_k \delta \mathbf{x} \|_{\mathbf{C}_k}. \quad (3.42)$$

The solution of eqn. (3.42) is

$$\delta \mathbf{x}_k^+ = (\mathbf{A}_k^\top \mathbf{C}_k^{-1} \mathbf{A}_k)^{-1} \mathbf{A}_k^\top \mathbf{C}_k^{-1} \delta \mathbf{Y}_k, \quad (3.43)$$

and the corresponding covariance of $\delta \mathbf{x}_k^+$ is $\mathbf{P}_k^+ = (\mathbf{A}_k^\top \mathbf{C}_k^{-1} \mathbf{A}_k)^{-1}$. With $\delta \mathbf{x}_k^+$, the INS state is updated as

$$\hat{\mathbf{x}}_k^+ = \hat{\mathbf{x}}_k^- \oplus \delta \mathbf{x}_k^+,$$

where the \oplus operator is discussed in Section 3.4, and the Kalman gain is

$$\begin{aligned} \mathbf{K}_k &= (\mathbf{A}_k^\top \mathbf{C}_k^{-1} \mathbf{A}_k)^{-1} \mathbf{A}_k^\top \mathbf{C}_k^{-1} \\ &= \mathbf{P}_k^- \mathbf{H}_k^\top (\mathbf{R}_k + \mathbf{H}_k \mathbf{P}_k^- \mathbf{H}_k^\top)^{-1}, \end{aligned} \quad (3.44)$$

where eqn. (3.44) is derived by expanding $(\mathbf{A}_k^\top \mathbf{C}_k^{-1} \mathbf{A}_k)^{-1} \mathbf{A}_k^\top \mathbf{C}_k^{-1}$.

The EKF works well for many aided INS applications, e.g. GPS-INS [25], Underwater-INS [72], Vision-Inertial-Odometry (VIO) [60–63]. However, the performance of the EKF depends on initial conditions and nonlinearities (see [22]), and prior EKF linearization points cannot be corrected at later times.

Two test cases are provided in Figs. 3.2 and 3.3, wherein the EKF divergence due to incorrect yaw initialization is shown. In both cases the EKF uses double-differenced

GPS pseudorange and Doppler measurements and a consumer-grade IMU. Both Figs. 3.2 and 3.3 display norm of the position, velocity and attitude error, where error is defined as ground-truth minus the estimate. In the experiment, the vehicle is level and at $t = 20\text{sec}$. accelerates (from stationary) with a heading of North. In Case 1, Fig. 3.2, the INS is initialized with 45° yaw error. While the EKF is able to remove most of the yaw error within a few GPS epochs, both position and velocity errors are large, and never recover. In Case 2, Fig. 3.3, the INS is initialized with 180° yaw error (worst-case). Here the EKF position, velocity, and attitude estimates diverge (oscillating indefinitely), and never recover.

To overcome the limitations of the EKF, a sliding window smoother is proposed for the GPS-INS problem, based on recent advances in the Simultaneous Localization and Mapping (SLAM) research community [22, 54, 55]. In Chapter 4, the MAP optimization based smoothing method is extended to GPS-INS, to enhance the navigation performance accuracy and reliability. In Chapter 8, the ability to completely remove the yaw initialization error of Case 2 (Fig. 3.3) is demonstrated using the proposed estimator of Chapter 4.

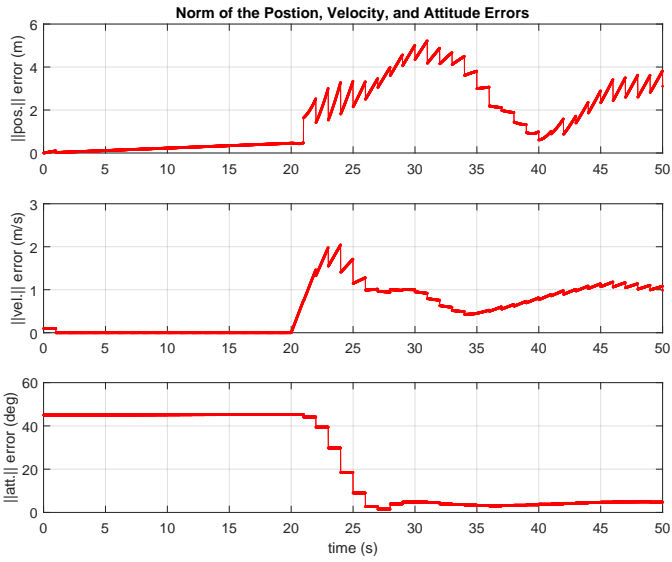


Figure 3.2: Case 1: Divergence of the GPS-INS EKF under poor yaw initialization.

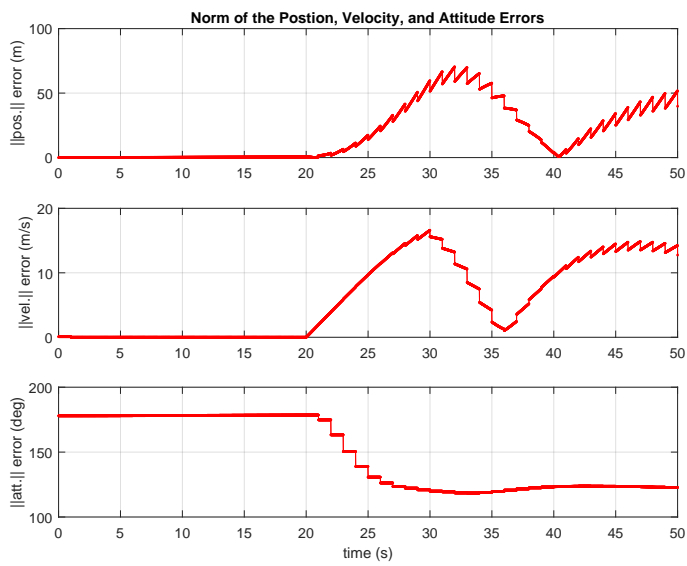


Figure 3.3: Case 2: Divergence of the GPS-INS EKF under worst-case yaw initialization.

Chapter 4

Estimation Theory

For a known linear system with white, normally distributed, and mutually uncorrelated process and measurement noise vectors with known covariance, the Kalman filter (KF) is the optimal estimator [56]. When the time propagation or measurement models are nonlinear, a variety of methods (e.g., the extended Kalman filter [68]) are available to solve the sensor fusion problem over a single GPS epoch.

This section reviews the MAP estimator [59] solved over a sliding temporal window in real-time. The problem has a long history [52]. While the theoretical motivations are distinct, the approach is also closely related to receding horizon estimation [46, 69, 75, 106]. This approach has been developed extensively in the Simultaneous Localization and Mapping (SLAM) research community [22, 24, 54, 55, 64, 74]. The approach developed for GPS-INS in [105] is referred to as a Contemplative Real Time (CRT) method due to the potential ability to evaluate and consider alternative outlier hypotheses for all data within the sliding window. That ability is demonstrated in [80] for CRT with Hypothesis Testing (CRT-HT), and for CRT with Least Soft-thresholding Squares (CRT-LSS) in [81]. The practical and

theoretical comparison of CRT-HT versus CRT-LSS is developed and demonstrated herein.

4.1 Theoretical Solution

Let $\mathbf{X} = [\mathbf{x}(t_{k-L})^\top, \dots, \mathbf{x}(t_k)^\top]^\top \in \mathbb{R}^{n_s(L+1)}$ denote the vehicle trajectory over a sliding time window that contains L GPS measurements: $[\mathbf{y}_{k-L+1}, \dots, \mathbf{y}_k]$. Assume that the window will slide one epoch upon arrival of each new GPS measurement. For presentation purposes only, assume that each GPS epoch aligns with an IMU measurement time. The results in the experimental section relax this assumption.

Estimation of the vehicle trajectory \mathbf{X} can be formulated as a MAP problem (see eqn. 11.18 in [59]):

$$\hat{\mathbf{X}} = \underset{\mathbf{X}}{\operatorname{argmax}} \{p(\mathbf{X}, \mathbf{U}, \mathbf{Y})\}, \quad (4.1)$$

where within the time window $\mathbf{U} = \{\mathbf{U}_l \mid l \in [k-L, k-1]\}$, and $\mathbf{Y} = \{\mathbf{y}_j \mid j \in [k-L+1, k]\}$ is the set of GPS measurements over the time window for satellites 1, ..., m . Both \mathbf{U} and \mathbf{Y} will be treated as concatenated vectors in the analysis that follows. The joint probability for the GPS-INS problem, $p(\mathbf{X}, \mathbf{U}, \mathbf{Y})$, can be factored as

$$p(\mathbf{X}, \mathbf{U}, \mathbf{Y}) = p(\mathbf{X}, \mathbf{U})p(\mathbf{Y} \mid \mathbf{X}, \mathbf{U}) \quad (4.2)$$

$$= p(\mathbf{X}, \mathbf{U})p(\mathbf{Y} \mid \mathbf{X}) \quad (4.3)$$

$$= p(\mathbf{X}, \mathbf{U}) \prod_{j=k-L+1}^k p(\mathbf{y}_j | \mathbf{x}_j) \quad (4.4)$$

$$= p(\mathbf{x}_{k-L}) \prod_{l=k-L}^{k-1} p(\mathbf{x}_{l+1} | \mathbf{x}_l, \mathbf{U}_l) \prod_{j=k-L+1}^k p(\mathbf{y}_j | \mathbf{x}_j), \quad (4.5)$$

where $p(\mathbf{x}_{k-L})$ is the distribution of the initial condition for the time window, $p(\mathbf{x}_{l+1} | \mathbf{x}_l, \mathbf{U}_{l+1})$ is the conditional distribution of the INS state estimate at $t = (l+1)T$, $p(\mathbf{y}_j | \mathbf{x}_j)$ is the dis-

tribution of the GPS measurement noise $\boldsymbol{\eta}_{y,k}$.

The steps for the formal proof of eqn. (4.5) are as follows: Eqn. (4.2) is obtained by applying the definition of conditional probability. Eqn. (4.3) is obtained by applying the conditional independence property. Eqn. (4.4) is obtained by assuming the noise affecting the sequence of measurements is independent. Eqn. (4.5) is obtained by assuming Markov process and temporal independence of process noise. ■

4.2 Numerical Solution

Assume that $\mathbf{x}(t_{k-L})$, \mathbf{w}_{k-1} , and $\boldsymbol{\eta}_y$ have Gaussian distributions with positive definite covariance matrices $\mathbf{P}_{(k-L)}$, $\mathbf{Q}_{\mathbf{D}}$, and \mathbf{R} , respectively. Finding \mathbf{X} that maximizes eqn. (4.5) is equivalent to minimizing the negative of its natural logarithm. This yields the equivalent nonlinear cost function:

$$\begin{aligned}\mathcal{C}(\mathbf{X}) &= \|\hat{\mathbf{x}}_{k-L} - \mathbf{x}(t_{k-L})\|_{\mathbf{P}_{(k-L)}}^2 \\ &+ \sum_{l=k-L}^{k-1} \|\Phi(\mathbf{x}(t_l), \mathbf{U}_l) - \mathbf{x}(t_{l+1})\|_{\mathbf{Q}_{\mathbf{D}}}^2 \\ &+ \sum_{j=k-L+1}^k \|\mathbf{y}(t_j) - \mathbf{h}_j(\mathbf{x}(t_j))\|_{\mathbf{R}}^2,\end{aligned}\quad (4.6)$$

which can be compactly expressed as $\mathcal{C}(\mathbf{X}) = \|\mathbf{v}(\mathbf{X})\|_{\mathbf{W}}^2$, where $\mathbf{v}(\mathbf{X}) \in \mathbb{R}^{(n_s+n_sL+2mL) \times 1}$ is defined as

$$\mathbf{v}(\mathbf{X}) = \left[\hat{\mathbf{x}}_{k-L}^\top - \mathbf{x}(t_{k-L})^\top, \Phi(\mathbf{X}, \mathbf{U})^\top - \mathbf{X}^\top, \mathbf{Y}^\top - \mathbf{h}(\mathbf{X})^\top \right]^\top.$$

In this expression, $\Phi(\mathbf{X}, \mathbf{U}) - \mathbf{X}$ represents the concatenation of the vector terms $\Phi(\mathbf{x}(t_l), \mathbf{U}_l) - \mathbf{x}(t_{l+1})$, and $\mathbf{h}(\mathbf{X})$ represents the concatenation of the vector terms $\mathbf{h}_j(\mathbf{x}(t_j))$. Using MATLAB syntax, the matrix $\mathbf{W} \in \mathbb{R}^{(n_s+n_sL+2mL) \times (n_s+n_sL+2mL)}$ is the positive definite block

diagonal matrix formed by the positive definite submatrices $\mathbf{P}_{(k-L)} \in \mathbb{R}^{n_s \times n_s}$, $\bar{\mathbf{Q}}_{\mathbf{D}} = \text{blkdiag}(\mathbf{Q}_{\mathbf{D}}) \in \mathbb{R}^{n_s L \times n_s L}$, and $\bar{\mathbf{R}} = \text{blkdiag}(\mathbf{R}) \in \mathbb{R}^{2mL \times 2mL}$. The matrix \mathbf{W} can be represented as $\mathbf{W} = \text{blkdiag}(\mathbf{P}_{(k-L)}, \bar{\mathbf{Q}}_{\mathbf{D}}, \bar{\mathbf{R}})$, and $\|\mathbf{v}\|_{\mathbf{W}}^2 = \mathbf{v}^\top \mathbf{W}^{-1} \mathbf{v}$ represents the squared Mahalanobis distance with matrix \mathbf{W} .

The cost function in eqn. (4.6) can be normalized using Cholesky Decomposition [22, 24, 54, 105]. Let $\Sigma_{\mathbf{W}}^\top \Sigma_{\mathbf{W}} = \mathbf{W}^{-1}$. Then, $\mathbf{r} \triangleq \Sigma_{\mathbf{W}} \mathbf{v}$ is the weighted residual, and $\|\mathbf{v}\|_{\mathbf{W}} = \|\mathbf{r}\|_2$. With this notation the cost function of eqn. (4.6) reduces to

$$\mathcal{C}(\mathbf{X}) = \|\mathbf{a} - \mathbf{b}(\mathbf{X})\|_2^2, \quad (4.7)$$

which will be minimized iteratively. In eqn. (4.7), the symbol

$$\mathbf{a} \doteq \Sigma_{\mathbf{W}} [\hat{x}_{k-L}^\top, \mathbf{0}^\top, \mathbf{Y}^\top]^\top \quad (4.8)$$

represents the terms that are known at each iteration, and

$$\mathbf{b}(\mathbf{X}) = \Sigma_{\mathbf{W}} [\mathbf{x}(t_{k-L})^\top, \Phi(\mathbf{X}, \mathbf{U})^\top - \mathbf{X}^\top, \mathbf{h}(\mathbf{X})^\top]^\top$$

represents the terms that are computed based on \mathbf{X} .

The optimal value of \mathbf{X} in eqn. (4.1) is

$$\mathbf{X}^* = \arg \min_{\mathbf{X}} \left\{ \|\mathbf{a} - \mathbf{b}(\mathbf{X})\|_2^2 \right\}. \quad (4.9)$$

Given an initial vector

$$\hat{\mathbf{X}} = [\hat{\mathbf{x}}(t_{k-L})^\top, \dots, \hat{\mathbf{x}}(t_k)^\top]^\top \in \mathbb{R}^{n_s(L+1)},$$

this optimization can be solved iteratively using a Taylor series expansion to approximate $\mathbf{b}(\mathbf{X})$:

$$\mathbf{b}(\mathbf{X}) = \mathbf{b}(\hat{\mathbf{X}}) + \mathbf{B} \delta \mathbf{X} + h.o.t's, \quad (4.10)$$

where the Jacobian $\mathbf{B} \doteq \frac{\partial \mathbf{b}(\mathbf{X})}{\partial \mathbf{X}} \Big|_{\mathbf{X}=\hat{\mathbf{X}}}$, and

$$\delta \mathbf{X} = [\delta \mathbf{x}(t_{k-L})^\top, \dots, \delta \mathbf{x}(t_k)^\top]^\top \in \mathbb{R}^{n_e(L+1)}.$$

Substituting eqn. (4.10) into eqn. (4.9) and ignoring the higher order terms (*h.o.t's*), yields

$$\begin{aligned} \delta \mathbf{X}^* &= \arg \min_{\delta \mathbf{X}} \|\mathbf{a} - (\mathbf{b}(\hat{\mathbf{X}}) + \mathbf{B}\delta \mathbf{X})\|_2^2 \\ &= \arg \min_{\delta \mathbf{X}} \|\mathbf{r} - \mathbf{B}\delta \mathbf{X}\|_2^2, \end{aligned} \quad (4.11)$$

where

$$\mathbf{r} \doteq \mathbf{a} - \mathbf{b}(\hat{\mathbf{X}}). \quad (4.12)$$

The optimal $\delta \mathbf{X}^*$ is found by solving

$$\mathbf{B}\delta \mathbf{X}^* = \mathbf{r} \quad (4.13)$$

in the least squares sense. The matrix $\mathbf{B} \in \mathbb{R}^{(n_e+n_eL+2mL) \times (n_e+n_eL+2mL)}$ is sparse; therefore, eqn. (4.13) can be solved efficiently by many methods, e.g. Cholesky, or QR. Further computational gains can be achieved by employing a sparse matrix library as discussed in [22, 24, 55].

The optimal $\delta \mathbf{X}$ is the solution of the normal equation:

$$\mathbf{B}^\top \mathbf{B}\delta \mathbf{X}^* \doteq \mathbf{B}^\top \mathbf{r}. \quad (4.14)$$

Eqn. (4.14) can be compactly expressed as

$$\boldsymbol{\Xi} \delta \mathbf{X} = \boldsymbol{\xi}, \quad (4.15)$$

where $\boldsymbol{\Xi} = \mathbf{B}^\top \mathbf{B}$ is the information matrix, $\boldsymbol{\xi} = \mathbf{B}^\top \mathbf{r}$ is the information vector [22, 24, 55, 105].

Given $\delta\mathbf{X}^*$, the update to the trajectory at each iteration is

$$\hat{\mathbf{X}}^+ \doteq \hat{\mathbf{X}}^- \oplus \delta\mathbf{X}^*. \quad (4.16)$$

The optimal solution is obtained by iterating eqns. (4.8), (4.10), (4.12), and (4.13) to convergence for some user defined stopping conditions. The superscript symbol ‘–’ denotes the trajectory estimate at the start of the iteration, and superscript ‘+’ is the updated trajectory estimate. The symbol ‘ \oplus ’, which is discussed in Section 3.4, represents the addition operation for position, velocity and bias states, and the multiplication operation of the attitude states. A line search is implemented in the direction of $\delta\mathbf{X}^*$ from eqn. (4.13) to determine the magnitude of the update step in eqn. (4.16) (see [24, 94]).

Solving the full MAP problem results in the optimal estimate of the vehicle trajectory \mathbf{X} . When the structure of $\boldsymbol{\Xi}$ is sparse, the computational load increases linearly with the length L of the trajectory (see [24]). The computational complexity of the CRT algorithm is discussed in Chapter 5.

4.3 Optimization: Iterated Solution

Consider the l^{th} iteration of the optimization, where l is a positive integer. Given an estimate of the solution $\hat{\mathbf{X}}^l$, the optimization algorithm computes an error vector $\delta\mathbf{X}^l$, which corrects $\hat{\mathbf{X}}^l$ using eqn. (4.16) to yield an improved solution $\hat{\mathbf{X}}^{l+1}$ to eqn. (4.6).

The fact that the trajectory \mathbf{X} must be re-integrated for each iteration, is discussed in Section 4.3 of [105]. The iterative process is terminated when either $\|\delta\mathbf{X}\|_2 \leq \epsilon$ or $l \geq l_{\max}$, where $\epsilon > 0$ is a user defined threshold, and l_{\max} is the user defined maximum number of

iterations.

The derivation of eqn. (4.11) shows that

$$\mathbf{r}(\mathbf{X}) = \mathbf{B}(\hat{\mathbf{X}})\delta\mathbf{X} + \boldsymbol{\eta}_r, \quad (4.17)$$

where $\mathbf{B}(\hat{\mathbf{X}})$ is the Jacobian of $\mathbf{r}(\mathbf{X})$ evaluated at $\hat{\mathbf{X}}$, with $\boldsymbol{\eta}_r \sim \mathcal{N}(\mathbf{0}, \mathbf{I})$. This fact will be used in Chapter 6.

Chapter 5

Computational Cost

In this chapter consider the computational cost (number of floating-point operations (FLOPs)) for each update of the CRT estimator. It is assumed that the implementation uses a sparse matrix library, and only compute and store the upper-triangular elements of all symmetric positive-definite matrices used in the CRT estimator. First define the computational cost of the Kalman Filter (KF) [25], then evaluate the most expensive operation, the computation of $\delta\mathbf{X}$ in the CRT estimator.

Consider the general matrices/vectors, $\mathbf{A} \in \mathbb{R}^{n \times n}$, $\mathbf{v} \in \mathbb{R}^{n \times 1}$, upper-triangular $\boldsymbol{\Sigma} \in \mathbb{R}^{n \times n}$, and $\mathbf{B} \in \mathbb{R}^{m \times n}$, with $m > n$. The computational cost for basic linear algebra operations on dense matrices [41] is shown in the first-half of Table 5.1. If \mathbf{A} and \mathbf{B} are sparse, a lower-bound can be determined using sparse matrix operations (see [40]), the results are shown in the second-half of Table 5.1. The computational cost for three matrix decompositions is provided in Table 5.2. The computational cost for three Least-Square

Table 5.1: Computational cost for dense and sparse matrices.

Operation	Computational Cost
Dense matrices	
\mathbf{A}^{-1}	$\approx n^3$
\mathbf{AA}	n^3
\mathbf{Av}	n^2
\mathbf{AB}^\top	mn^2
$\mathbf{B}^\top \mathbf{B}$	mn^2
\mathbf{Bv}	mn
$\Sigma \mathbf{v}$	$\frac{n^2-n}{2} + n$
$\Sigma \mathbf{A}$	$\frac{n^3-n^2}{2} + n^2$
$\Sigma \Sigma$	$\frac{n^3}{3}$
Sparse matrices	
\mathbf{A}^{-1}	n
\mathbf{AA}	n
\mathbf{Av}	n
\mathbf{AB}^\top	n
$\mathbf{B}^\top \mathbf{B}$	n
\mathbf{Bv}	n

Table 5.2: Computational cost for matrix decompositions.

Decomposition	Computational Cost
Cholesky (Section 4.2.1 [41])	$\frac{n^3}{3}$
Householder QR (Section 5.2.1 [41])	$4 \left(m^2n - mn^2 + \frac{n^3}{3} \right)$
Givens QR (Section 5.2.3 [41])	$3n^2 \left(m - \frac{n}{3} \right)$

Table 5.3: Computational cost for LS algorithms (Section 5.5.9 [41]).

LS Algorithm	Computational Cost
Normal Equations	$mn^2 + \frac{n^3}{3}$
Householder QR Orthogonalization	$2mn^2 + \frac{2n^3}{3}$
Givens QR Orthogonalization	$3mn^2 - n^3$

(LS) algorithms is provided in Table 5.3.

5.1 Computational cost for KF

For the KF state estimate $\hat{\mathbf{x}} \in \mathbb{R}^n$, and measurement $\mathbf{y} \in \mathbb{R}^m$ with $m > n$, the computational cost with dense matrices is presented in Table 5.4.

5.2 Computational cost for CRT using Normal Equations

This section is split into two primary parts: first compute $\delta\mathbf{X}$ by dense matrices, then compute $\delta\mathbf{X}$ by sparse matrices. In both cases we only consider one iteration of the optimization. Because the calculation of $\delta\mathbf{X}$ is the most expensive operation in the CRT estimator, assume the state transition matrix Φ , measurement matrix \mathbf{H} , measurement prediction $\hat{\mathbf{y}}$, integrated state vector \mathbf{x}_i , and optimized state vector \mathbf{x}^* are each given (refer to Sections 3 & 4) and are therefore not included in the cost to compute $\delta\mathbf{X}$.

Table 5.4: Computational cost for the KF (Section 3.3.1 [43]).

Operation	Computational Cost
System Propagation	
$\hat{\mathbf{x}}_k^- = \Phi_{k-1}\hat{\mathbf{x}}_{k-1}^+$	n^2
$\mathbf{P}_k^- = \Phi_{k-1}\mathbf{P}_{k-1}^-\Phi_{k-1}^\top + \mathbf{Q}\mathbf{d}_{k-1}$	$2n^3$
Measurement update	
$\mathbf{K}_k = \mathbf{P}_k^-\mathbf{H}_k^\top(\mathbf{H}_k\mathbf{P}_k^-\mathbf{H}_k^\top + \mathbf{R}_k)^{-1}$	$2mn^2 + 2mn$
$\hat{\mathbf{x}}_k^+ = \hat{\mathbf{x}}_k^- + \mathbf{K}_k(\mathbf{y}_k - \mathbf{H}_k\hat{\mathbf{x}}_k^-)$	$2mn$
$\mathbf{P}_k^+ = (\mathbf{I} - \mathbf{K}_k\mathbf{H}_k)\mathbf{P}_k^-$	$2mn^2$

5.2.1 Dense Jacobian

Given the number of error states n_e , the number of measurements n_m , and CRT window length L , the components of the normalized Jacobian matrix \mathbf{J} and residual vector \mathbf{r} , are defined below with a mapping to the number of computations required for dense matrices. Both \mathbf{J} and \mathbf{r} are normalized using Cholesky factorization¹, which has computational complexity $\frac{n^3}{3}$. Define $\delta\mathbf{X}_O$, \mathbf{r}_O , and \mathbf{J}_O as the number of operations to compute $\delta\mathbf{X}$, \mathbf{r} , and \mathbf{J} , respectively.

The components of the Jacobian are,

$$\begin{aligned}\mathbf{J}_{\mathbf{P}_0} &\triangleq \Sigma_{\mathbf{P}_0}[\mathbf{I}, \mathbf{0}] \mapsto \left(\frac{n_e^3}{3} + n_e^3 \right) \\ \mathbf{J}_{\mathbf{Qd}} &\triangleq \Sigma_{\mathbf{Qd}}[\Phi, -\mathbf{I}] \mapsto \left(\frac{n_e^3}{3} + 2n_e^3 \right) L \\ \mathbf{J}_{\mathbf{R}} &\triangleq \Sigma_{\mathbf{R}}\mathbf{H} \mapsto \left(\frac{n_m^3}{3} + n_m n_e^2 \right) L \\ \mathbf{J} &\triangleq \begin{bmatrix} \mathbf{J}_{\mathbf{P}_0} \\ \mathbf{J}_{\mathbf{Qd}} \\ \mathbf{J}_{\mathbf{R}} \end{bmatrix} \mapsto \begin{bmatrix} \frac{n_e^3}{3} + n_e^3 \\ \left(\frac{n_e^3}{3} + 2n_e^3 \right) L \\ \left(\frac{n_m^3}{3} + n_m n_e^2 \right) L \end{bmatrix},\end{aligned}$$

where, $\mathbf{J}_{\mathbf{P}_0} \in \mathbb{R}^{n_e \times n_e}$, $\mathbf{J}_{\mathbf{Qd}} \in \mathbb{R}^{n_e L \times n_e L}$, $\mathbf{J}_{\mathbf{R}} \in \mathbb{R}^{n_m L \times n_e L}$, and $\mathbf{J} \in \mathbb{R}^{(n_e(L+1)+n_m L) \times (n_e(L+1))}$.

The number of operations to compute \mathbf{J} is

$$\mathbf{J}_O = \frac{n_e^3}{3} + n_e^3 + \left(\frac{n_e^3}{3} + 2n_e^3 + \frac{n_m^3}{3} + n_m n_e^2 \right) L.$$

¹Householder QR, or Givens QR factorization may be used instead (see Table 5.2).

The components of the residual vector are,

$$\mathbf{r}_{\mathbf{P}_0} \triangleq \Sigma_{\mathbf{P}_0} [\boldsymbol{\mu} - \boldsymbol{x}^*] \mapsto n_e^2$$

$$\mathbf{r}_{\mathbf{Qd}} \triangleq \Sigma_{\mathbf{Qd}} [\boldsymbol{x}^* - \boldsymbol{x}_i] \mapsto n_e^2 L$$

$$\mathbf{r}_{\mathbf{R}} \triangleq \Sigma_{\mathbf{R}} \boldsymbol{\delta} \mathbf{y} \mapsto n_m n_e L$$

$$\mathbf{r} \triangleq \begin{bmatrix} \mathbf{r}_{\mathbf{P}_0} \\ \mathbf{r}_{\mathbf{Qd}} \\ \mathbf{r}_{\mathbf{R}} \end{bmatrix} \mapsto \begin{bmatrix} n_e^2 \\ n_e^2 L \\ n_m n_e L \end{bmatrix},$$

where, $\mathbf{r}_{\mathbf{P}_0} \in \mathbb{R}^{n_e \times 1}$, $\mathbf{r}_{\mathbf{Qd}} \in \mathbb{R}^{n_e L \times 1}$, $\mathbf{r}_{\mathbf{R}} \in \mathbb{R}^{n_m L \times 1}$, and $\mathbf{r} \in \mathbb{R}^{(n_e(L+1)+n_m L) \times 1}$. Note, the $\frac{n_e^3}{3}$ and $\frac{n_m^3}{3}$ are not included in the components \mathbf{r} , because the cost to compute the Cholesky decomposition is included in the components of \mathbf{J} . The number of operations to compute \mathbf{r} is

$$\mathbf{r}_O = n_e^2 + (n_e^2 + n_m n_e) L.$$

Given the residual vector $\mathbf{r} \in \mathbb{R}^{p \times 1}$ and (dense) Jacobian $\mathbf{J} \in \mathbb{R}^{p \times q}$ for $p > q$, where $p = (n_e \times (L + 1)) + (n_m \times L)$ and $q = (n_e \times (L + 1))$, the number of operations to compute $\boldsymbol{\delta} \mathbf{X}$ by the Normal Equations is

$$\boldsymbol{\delta} \mathbf{X} = (\mathbf{J}^\top \mathbf{J})^{-1} \mathbf{J}^\top \mathbf{r} \mapsto pq^2 + \frac{q^3}{3} = \boldsymbol{\delta} \mathbf{X}_O.$$

Expanding p and q :

$$\boldsymbol{\delta} \mathbf{X}_O = n_e^3 \left(\frac{4}{3} L^3 + 4L^2 + 4L + \frac{4}{3} \right) + n_e^2 n_m (L^3 + 2L^2 + L).$$

Define $\delta\mathbf{X}_{TO}$ as the total number of operations to compute $\delta\mathbf{X}$ by the Normal Equations.

$$\begin{aligned}
 \delta\mathbf{X}_{TO} &= \delta\mathbf{X}_O + \mathbf{r}_O + \mathbf{J}_O \\
 &= n_e^3 \left(\frac{4}{3}L^3 + 4L^2 + 4L + \frac{4}{3} \right) + n_e^2 n_m (L^3 + 2L^2 + L) + n_e^2 + (n_e^2 + n_m n_e) L \\
 &\quad + \frac{n_e^3}{3} + n_e^3 + \left(\frac{n_e^3}{3} + n_e^2 + \frac{n_m^3}{3} + n_m n_e^2 \right) L \\
 &= n_e^3 \left(\frac{4}{3}L^3 + 4L^2 + \frac{19}{3}L + \frac{8}{3} \right) + n_e^2 (n_m L^3 + 2n_m L^2 + 2n_m L + L + 1) \\
 &\quad + n_e n_m L + \frac{n_m^3}{3} L.
 \end{aligned}$$

Therefore the computation for a single iteration of the dense $\delta\mathbf{X}$ by the Normal Equations is $\mathcal{O}(n_e^3 L^3)$.

5.2.2 Sparse Jacobian

Presently, common sparse libraries do not support LS by the Normal Equations because the operations are not efficient (see [41] and [40]). By inspection, the operation $\mathbf{J}^\top \mathbf{J}$ produces a dense matrix, and the inversion of $\mathbf{J}^\top \mathbf{J}$ is $\mathcal{O}(n_e^3 L^3)$.

5.3 Computational cost for CRT using QR Factorization

This section first introduces the theory for solving systems of linear equations using QR factorization, then follows an outline similar to Section 5.2. The same assumptions of Section 5.2 apply here.

5.3.1 Theory

Let $\mathbf{A} \in \mathbb{R}^{m \times n}$ with $m \geq n$ and $\mathbf{b} \in \mathbb{R}^m$. Suppose that the orthogonal matrix $\mathbf{Q} \in \mathbb{R}^{m \times m}$ is computed such that

$$\mathbf{Q}^\top \mathbf{A} = \mathbf{R} = \begin{bmatrix} \mathbf{R}_1 \\ \mathbf{0} \end{bmatrix}$$

is upper-triangular, with $\mathbf{R}_1 \in \mathbb{R}^{n \times n}$ and $\mathbf{0} \in \mathbb{R}^{(m-n) \times n}$. If

$$\mathbf{Q}^\top \mathbf{b} = \begin{bmatrix} \mathbf{c} \\ \mathbf{d} \end{bmatrix}$$

where $\mathbf{c} \in \mathbb{R}^{n \times 1}$ and $\mathbf{d} \in \mathbb{R}^{(m-n) \times 1}$, then

$$\begin{aligned} \|\mathbf{A}\mathbf{x} - \mathbf{b}\|_2^2 &= \|\mathbf{Q}^\top \mathbf{A}\mathbf{x} - \mathbf{Q}^\top \mathbf{b}\|_2^2 \\ &= \|\mathbf{R}_1\mathbf{x} - \mathbf{c}\|_2^2 + \|\mathbf{d}\|_2^2 \end{aligned} \tag{5.1}$$

for any $\mathbf{x} \in \mathbb{R}^n$. If $\text{rank}(\mathbf{A}) = \text{rank}(\mathbf{R}_1) = n$, then the Least-Square estimate $\hat{\mathbf{x}}$ is defined by the upper-triangular system $\mathbf{R}_1\hat{\mathbf{x}} = \mathbf{c}$. Given \mathbf{R}_1 , solving this system requires $2n^2(m - \frac{n}{3})$ FLOPs. While $\mathcal{O}(mn)$ are required to update \mathbf{c} , and $\mathcal{O}(n^2)$ are required for back-substitution (see Section 5.3.2 of [41]), the most expensive operation is the QR factorization of \mathbf{A} , which requires at least $3n^2(m - \frac{n}{3})$ FLOPs (assuming Givens QR).

Modifying eqn. (5.1) for the CRT estimator, define $\mathbf{J} \in \mathbb{R}^{p \times q}$, $\mathbf{r} \in \mathbb{R}^{p \times 1}$, $\delta\mathbf{X} \in \mathbb{R}^{q \times 1}$, $\mathbf{R}_1 \in \mathbb{R}^{q \times q}$, $\mathbf{c} \in \mathbb{R}^{q \times 1}$ and $\mathbf{d} \in \mathbb{R}^{(p-q) \times 1}$. For

$$\mathbf{J}\delta\mathbf{X} = \mathbf{r}$$

the Least-Square estimate $\hat{\delta\mathbf{X}}$ of $\delta\mathbf{X}$ is found by

$$\|\mathbf{J}\delta\mathbf{X} - \mathbf{r}\|_2^2 = \|\mathbf{R}_1\delta\mathbf{X} - \mathbf{c}\|_2^2 + \|\mathbf{d}\|_2^2$$

where $\delta\hat{\mathbf{X}}$ is defined by the upper-triangular system $\mathbf{R}_1\delta\hat{\mathbf{X}} = \mathbf{c}$.

5.3.2 Dense Jacobian

Let $\mathbf{J}_{QR,d}$ denote the number of operations to compute the QR factorization of (dense) \mathbf{J} . Using the previously defined values for p and q , and the values in Table 5.2,

$$\begin{aligned}\mathbf{J}_{QR,d} &= 3q^2 \left(p - \frac{q}{3} \right) \\ &= 2n_e^3(L^3 + 3L^2 + 3L + 1) + 3n_e^2 n_m(L^3 + 2L^2 + L).\end{aligned}$$

Let $\delta\hat{\mathbf{X}}_{QR,d}$ denote the number of operations to compute the Least-Square estimate $\delta\hat{\mathbf{X}}$ with Givens QR of (dense) \mathbf{J} (see Table 5.3). Then

$$\begin{aligned}\delta\hat{\mathbf{X}}_{QR,d} &= 2q^2 \left(p - \frac{q}{3} \right) \\ &= 2n_e^3(L^3 + 3L^2 + 3L + 1) + 3n_e^2 n_m(L^3 + 2L^2 + L).\end{aligned}$$

Therefore the computation for a single iteration of the dense $\delta\mathbf{X}$ using Givens QR is $\mathcal{O}(n_e^3 L^3)$.

5.3.3 Sparse Jacobian

Let $\mathbf{J}_{QR,s}$, $\mathbf{r}_{QR,s}$, and $\delta\mathbf{X}_{QR,s}$, denote the number of operations to compute the QR factorization of (sparse) \mathbf{J} , \mathbf{r} , and $\delta\mathbf{X}$, respectively. The components of the sparse Jacobian are,

$$\begin{aligned}\mathbf{J}_{\mathbf{P}_0} &\mapsto \left(\frac{n_e^3}{3} + \frac{n_e^2 - n_e}{2} + n_e \right) \\ \mathbf{J}_{\mathbf{Qd}} &\mapsto \left(\frac{n_e^3}{3} + \frac{n_e^3 - n_e^2}{2} + n_e^2 + \frac{n_e^2 - n_e}{2} + n_e \right) L \\ \mathbf{J}_{\mathbf{R}} &\mapsto \left(\frac{n_m^3}{3} + 3n_m \right) L.\end{aligned}$$

The number of operations to compute \mathbf{J} is

$$\mathbf{J}_{QR,s} = \frac{n_e^3}{3} + \frac{n_e^2 - n_e}{2} + n_e + \left(\frac{n_e^3}{3} + \frac{n_e^3 - n_e^2}{2} + n_e^2 + \frac{n_e^2 - n_e}{2} + n_e \right) L + \left(\frac{n_m^3}{3} + 3n_m \right) L.$$

The components of the residual vector are,

$$\begin{aligned}\mathbf{r}_{\mathbf{P}_0} &\mapsto \left(\frac{n_e^2 - n_e}{2} + n_e \right) \\ \mathbf{r}_{\mathbf{Qd}} &\mapsto \left(\frac{n_e^2 - n_e}{2} + n_e \right) L \\ \mathbf{r}_{\mathbf{R}} &\mapsto n_m L.\end{aligned}$$

The number of operations to compute \mathbf{r} is

$$\mathbf{r}_{QR,s} = \frac{n_e^2 - n_e}{2} + n_e + \left(\frac{n_e^2 - n_e}{2} + n_e + n_m \right) L$$

Using a sparse library [40], the LS solution via QR factorization is proportional to the number of non-zero elements in the Jacobian (see [41] and [40]). Therefore

$$\delta\mathbf{X}_{QR,s} = n_e(L + 1) + n_m L$$

Define $\delta\mathbf{X}_{QR,TO}$ as the total number of operations to compute $\delta\mathbf{X}$ by the sparse QR factorization.

$$\begin{aligned}\delta\mathbf{X}_{QR,TO} &= \delta\mathbf{X}_O + \mathbf{r}_O + \mathbf{J}_O \\ &= n_e^3 \left(\frac{1}{3} + \frac{1}{3}L \right) + n_e^2 \left(\frac{n_e - 1}{2}L + 1 \right) + n_e(3L + 3) + n_m \left(\frac{1}{3}n_m^2 L + 5L \right).\end{aligned}$$

Therefore the computation for a single iteration of the sparse $\delta\mathbf{X}$ using QR factorization is $\mathcal{O}(n_e^3 L)$.

5.4 Discussion

5.4.1 Normal Equations vs. QR

In Section 5.3.8 of [41], the authors identify the challenge with selecting the “right” algorithm to solve a linear system of equations.

- Condition Number: while the Normal Equations effectively square the condition number, QR does not.
- Arithmetic: the Normal Equations use roughly half of the arithmetic as QR when $m \gg n$, while also requiring less storage (memory).
- Applicability: unlike the Normal Equations, QR is more widely applicable because the errors that arise in $\mathbf{A}^\top \mathbf{A}$ of the Normal Equations “break down” more quickly than the process on $\mathbf{Q}^\top \mathbf{A} = \mathbf{R}$ of LS by QR.

5.4.2 Sparse vs. Dense

Considering only LS solutions using QR, Sections 5.3.2 and 5.3.3 clearly define the cost savings using sparse matrices which are $\mathcal{O}(n_e^3 L)$, versus dense matrices which are $\mathcal{O}(n_e^3 L^3)$.

However, on modern computers with dual-precision (64-bit) floating point processors, the primary factor in computational cost is not FLOPs, rather in the storage and memory access of the data [40]. Identifying the computational complexity is important to understand the amount of storage required by a particular algorithm, as sparse representations use less memory and require fewer memory accesses.

5.4.3 Estimator Comparison

The computational cost for the calculation of $\delta\mathbf{X}$ in the Iterated Extended KF (IEKF), e.g. CRT with $L = 1$, is $\mathcal{O}(n_e^3)$, whereas the most expensive computation of the KF is the state covariance propagation, $\mathcal{O}(n_e^3)$. In contrast, the CRT estimator, with window length L , scales linearly in L with $\mathcal{O}(n_e^3L)$ when using sparse matrices.

Chapter 6

Residual Space Outlier Detection

Beard is credited for early work in the field of outlier detection in state estimation systems. Beard, in his 1971 Ph.D. thesis [14], defines two stages in outlier detection, namely residual generation and decision making.

Residual generation can be performed by many methods common to state estimation, e.g. least-squares [21, 31, 67], recursive least-squares [51], or parity space [15, 17, 23, 37–39, 70, 78, 91, 93].

The most common challenge to outlier detection is the issue of multiple outliers in a given dataset. Hampel estimates that a routine dataset contain 1-10% (or more) outliers [45]. A study, performed by Rousseeuw [79], identified that in many cases outliers go unnoticed, causing serious effects in estimation or model selection. The most popular statistical modeling method is least-squares [79], which is very sensitive to outliers, so sensitive in-fact a single outlier may cause the estimate to fail completely.

A common method for outlier detection is the *leave-one-out* approach [99]. In this iterative approach, the i 'th measurement is left out, and the residual is generated for

the remaining measurements. If there are multiple outliers in the remaining measurements, and the remaining outliers result in a large standard deviation, then the i 'th measurement does not appear as an outlier; this is called *masking* [99]. If the outliers cause the norm of the residual to be large for the non-outlier case of the i 'th measurement, the result is called *swamping* [99]. The effects of masking and swamping are the primary challenge to multiple outlier detection, making the selection of the decision making process a crucial step in outlier detection.

The decision making process can be performed by a variety of methods. In 1925, Fisher proposed a hypothesis test to evaluate measurements against their expected value, for a fixed threshold [27]. After Fisher, many threshold tests were developed to evaluate measurements against a *normal* distribution [84], a *hypothesized* distribution [2], or an *empirically derived* distribution [87,90]. However it was Neyman and Pearson who identified the limitations of a fixed threshold, particularly if based on an incorrect distribution. They proposed the “Neyman-Pearson Lemma;” an adaptive threshold hypothesis test, based on a generalized likelihood ratio test (GLRT) [76,78]. Derivations of both the NP-Lemma and the GLRT are provided in Appendix B and C, respectively.

Robustness to outlier measurements can be achieved by both sensor and analytical redundancy [12, 13, 28, 29, 36, 65, 77, 89, 103], with further improvements to modeling (less truncation of higher order terms in Taylor series expansions of nonlinear functions) or initialization errors, by using nonlinear optimization [30, 32, 39].

6.1 Problem Formulation

This section examines the Residual Space method for outlier detection and removal. The discussion in this section uses the standard notation in the hypothesis testing (HT) literature [2, 84, 87]. The mapping between the HT and CRT variables, comparing eqns. (4.17) and (6.1), is $\mathbf{y} = \mathbf{r}$, $\mathbf{H} = \mathbf{B}$, $\mathbf{x} = \delta\mathbf{X}$, and $\boldsymbol{\eta} = \boldsymbol{\eta}_r$. By eqn. (4.17), $\mathcal{N}(\mathbf{0}, \sigma_\eta^2 \mathbf{I})$ with $\sigma_\eta^2 = 1$. Complete derivations for this section are provided in Section 5 of [82]. The method developed in this section will be referred to herein as CRT-HT.

Before the optimization process discussed in Section 4.3, the state vector is integrated from the prior (optimized) state $\hat{\mathbf{X}}^0(t_{k-L})$ to the current GPS epoch t_k , giving an initial trajectory $\hat{\mathbf{X}}^0$, then the GPS residual is computed. Note we assume the prior and IMU to be outlier free, and therefore only consider GPS outliers. Consider the following hypotheses related to the GPS residual $\mathbf{r}(\hat{\mathbf{X}}^0)$:

- Null Hypothesis, \mathcal{H}_0 :

$$\mathbf{y} = \mathbf{H}\mathbf{x} + \boldsymbol{\eta}, \quad (6.1)$$

- Alternative Hypothesis, $\mathcal{H}_{i \geq 1}$:

$$\mathbf{y} = \mathbf{H}\mathbf{x} + \boldsymbol{\eta} + \mu_i \mathbf{e}_i. \quad (6.2)$$

For \mathcal{H}_i , corresponding to eqn. (3.5), the outlier model is $\mathbf{s} = \mu_i \mathbf{e}_i$ and since the prior and IMU are assumed outlier free: $i = n_e(L+1) + 1, \dots, n_e(L+1) + 2m$. When the magnitude of the outlier μ_i is nonzero, the i^{th} measurement is called an outlier. The magnitude μ_i will affect the ability to detect such outliers. The null-hypothesis assumes no outliers, i.e., $\mu_i = 0$.

In this section, $\mathbf{y} \in \mathbb{R}^{p \times 1}$ is the measurement vector, $\mathbf{H} \in \mathbb{R}^{p \times q}$, $p > q$, $\text{rank}(\mathbf{H}) = q$ is the measurement matrix, and $\mathbf{x} \in \mathbb{R}^{q \times 1}$ is the vector to be estimated. For the alternative hypothesis, $\mathbf{e}_i = [0, \dots, 0, 1, 0, \dots, 0]^\top \in \mathbb{R}^{p \times 1}$, such that only the i^{th} element is 1. To simplify notation in the following equations, let

$$\boldsymbol{\varepsilon}_i \triangleq \mu_i \mathbf{e}_i.$$

6.1.1 Null-Hypothesis, \mathcal{H}_0

Corresponding to eqn. (6.1), the minimum-variance unbiased estimator (MVUE) [59] for \mathbf{x} is

$$\hat{\mathbf{x}} = (\mathbf{H}^\top \mathbf{H})^{-1} \mathbf{H}^\top \mathbf{y}. \quad (6.3)$$

To analyze the effect of $\boldsymbol{\eta}$, substitute eqn. (6.1) into eqn. (6.3)

$$\begin{aligned} \hat{\mathbf{x}} &= ((\mathbf{H}^\top \mathbf{H})^{-1} \mathbf{H}^\top)(\mathbf{H}\mathbf{x} + \boldsymbol{\eta}) \\ &= \mathbf{I}\mathbf{x} + \mathbf{H}^*\boldsymbol{\eta}, \end{aligned} \quad (6.4)$$

where $\mathbf{H}^* \triangleq (\mathbf{H}^\top \mathbf{H})^{-1} \mathbf{H}^\top$. The state error is defined as $\delta\mathbf{x} \triangleq \mathbf{x} - \hat{\mathbf{x}}$. From eqn. (6.4) $\delta\mathbf{x} = \mathbf{H}^*\boldsymbol{\eta}$. Due to the zero mean noise assumption, the expected value of the state error is $E\langle \delta\mathbf{x} \rangle = \mathbf{0}$.

Consider the residual $\mathbf{r}_0 \triangleq \mathbf{y} - \hat{\mathbf{y}}$, where $\hat{\mathbf{y}} = \mathbf{H}\hat{\mathbf{x}} = \mathbf{H}(\mathbf{H}^\top \mathbf{H})^{-1} \mathbf{H}^\top \mathbf{y}$. Then

$$\mathbf{r}_0 = (\mathbf{I} - \mathbf{P})\boldsymbol{\eta}, \quad (6.5)$$

where $\mathbf{P} \triangleq \mathbf{H}(\mathbf{H}^\top \mathbf{H})^{-1} \mathbf{H}^\top \in \mathbb{R}^{p \times p}$ is the projection matrix onto the range-space of \mathbf{H} . The matrix \mathbf{P} is symmetric, idempotent, and $\text{rank}(\mathbf{P}) = q$ (see Appendix A.5).

Similarly, the matrix $\mathbf{Q} \triangleq (\mathbf{I} - \mathbf{P}) \in \mathbb{R}^{p \times p}$ is a real, symmetric, and idempotent matrix (i.e. $\mathbf{Q}\mathbf{Q}^\top = \mathbf{Q}$). The matrix \mathbf{Q} is a projection matrix onto the left null-space of \mathbf{H} . It has eigenvalues equal to 0 or 1, and its trace is equal to the number of non-zero eigenvalues: $(p - q)$ (see Appendix A.7).

The mean and covariance of the residual are

$$\begin{aligned} E\langle \mathbf{r}_0 \rangle &= E\langle \mathbf{Q}\boldsymbol{\eta} \rangle \\ &= \mathbf{0} \end{aligned} \tag{6.6}$$

$$\begin{aligned} \text{Cov}\langle \mathbf{r}_0 \rangle &= E\langle (\mathbf{r}_0 - E\langle \mathbf{r}_0 \rangle)(\mathbf{r}_0 - E\langle \mathbf{r}_0 \rangle)^\top \rangle \\ &= \mathbf{Q}E\langle \boldsymbol{\eta}\boldsymbol{\eta}^\top \rangle \mathbf{Q}^\top \\ &= \sigma_\eta^2 \mathbf{Q}. \end{aligned} \tag{6.7}$$

The final step is valid because \mathbf{Q} is idempotent (see Appendix A.6), and $E\langle \boldsymbol{\eta}\boldsymbol{\eta}^\top \rangle = \sigma_\eta^2 \mathbf{I}$.

The mean square error (MSE) [59] is

$$\begin{aligned} E\langle \|\mathbf{r}_0\|^2 \rangle &= E\langle \mathbf{r}_0^\top \mathbf{r}_0 \rangle \\ &= E\langle \text{tr}\{\mathbf{r}_0 \mathbf{r}_0^\top\} \rangle \\ &= E\langle \text{tr}\{\mathbf{Q}\boldsymbol{\eta}\boldsymbol{\eta}^\top \mathbf{Q}^\top\} \rangle \\ &= \text{tr}\{\mathbf{Q}\} \sigma_\eta^2 \\ &= (p - q) \sigma_\eta^2, \end{aligned} \tag{6.8}$$

where $\text{tr}\{\cdot\}$ is the trace operator.

The standard test statistic $\Gamma_{\hat{\mathbf{X}}}$ for the validity of \mathcal{H}_0 [2, 84, 87] is based on eqns. (6.5) and (6.8):

$$\begin{aligned}\Gamma_{\hat{\mathbf{X}}} &= \frac{\|\mathbf{r}_0(\hat{\mathbf{X}})\|^2}{\mathrm{E} \left\langle \|\mathbf{r}_0(\hat{\mathbf{X}})\|^2 \right\rangle} \\ &= \frac{\|\mathbf{r}_0(\hat{\mathbf{X}})\|^2}{(p-q)\sigma_\eta^2}.\end{aligned}\quad (6.9)$$

Under \mathcal{H}_0 , the statistic $\Gamma_{\hat{\mathbf{X}}}$ is a reduced chi-square [58] with expected value equal to 1 that can be used to test the validity of hypothesis \mathcal{H}_0 (i.e., detect the existence of outliers). The test statistic calculated by eqn. (6.9) is evaluated relative to a threshold computed using the one-tailed chi-square distribution with significance level α , normalized by the number of degrees-of-freedom (DOF) [27, 58]:

$$\Gamma_{\hat{\mathbf{X}}} < \frac{\chi_{\alpha/2,(p-q)}^2}{(p-q)}. \quad (6.10)$$

The threshold $\chi_{\alpha/2,(p-q)}^2$ is determined from a look-up table for α versus DOF. The significance level α is chosen by the designer for some probability of success. For example, $\alpha = 0.05$ indicates a 95% confidence level.

If the test succeeds, $\mathbf{r}_0(\hat{\mathbf{X}})$ is assumed outlier-free, and the optimization step of Section 4.2 is performed. Otherwise, outlier identification executes.

6.1.2 Alternate-Hypothesis, \mathcal{H}_i

To analyze the effect of the outlier ε_i on the state error, substitute eqn. (6.2) into eqn. (6.3)

$$\begin{aligned}\hat{\mathbf{x}} &= ((\mathbf{H}^\top \mathbf{H})^{-1} \mathbf{H}^\top)(\mathbf{H}\mathbf{x} + \boldsymbol{\eta} + \varepsilon_i) \\ &= \mathbf{I}\mathbf{x} + (\mathbf{H}^\top \mathbf{H})^{-1} \mathbf{H}^\top(\boldsymbol{\eta} + \varepsilon_i).\end{aligned}\quad (6.11)$$

Therefore, $\delta \mathbf{x} = \mathbf{H}^*(\boldsymbol{\eta} + \boldsymbol{\varepsilon}_i)$. The expected value of the state error due to the outlier is $E \langle \delta \mathbf{x} \rangle = \mathbf{H}^* \boldsymbol{\varepsilon}_i$.

To analyze the effect of the outlier on the residual, substitute eqns. (6.2) and (6.11) into eqn. (6.5):

$$\begin{aligned} \mathbf{r} &= \mathbf{H}\mathbf{x} + \boldsymbol{\eta} + \boldsymbol{\varepsilon}_i - \mathbf{H}\hat{\mathbf{x}} \\ &= \mathbf{H}\mathbf{x} + \boldsymbol{\eta} + \boldsymbol{\varepsilon}_i - \mathbf{H}(\mathbf{I}\mathbf{x} + (\mathbf{H}^\top \mathbf{H})^{-1} \mathbf{H}^\top (\boldsymbol{\eta} + \boldsymbol{\varepsilon}_i)) \\ &= \mathbf{Q}(\boldsymbol{\eta} + \boldsymbol{\varepsilon}_i). \end{aligned} \quad (6.12)$$

Note that the residual still lies in the left-null-space of \mathbf{H} . The mean and covariance of \mathbf{r} due to the outlier, are

$$E \langle \mathbf{r} \rangle = E \langle \mathbf{Q}(\boldsymbol{\eta} + \boldsymbol{\varepsilon}_i) \rangle = \mathbf{Q}\boldsymbol{\varepsilon}_i \quad (6.13)$$

$$\text{Cov} \langle \mathbf{r} \rangle = E \langle (\mathbf{r} - \mathbf{Q}\boldsymbol{\varepsilon}_i)(\mathbf{r} - \mathbf{Q}\boldsymbol{\varepsilon}_i)^\top \rangle = \sigma_y^2 \mathbf{Q}. \quad (6.14)$$

Comparing eqn. (6.7) with eqn. (6.14), we see that the covariance is the same both with and without the outlier. However, the means are different, as shown in eqns. (6.6) and (6.13), which provides a method for identifying outliers. The decision statistic under the alternate-hypothesis \mathcal{H}_i , is based on the distribution of $\mathbf{r} \sim \mathcal{N}(\mathbf{Q}\boldsymbol{\varepsilon}_i, \sigma_y^2 \mathbf{Q})$.

Consider the parity vector [16, 91]

$$\mathbf{p} \triangleq \mathbf{U}_2^\top \mathbf{r} \in \mathbb{R}^{(p-q)},$$

where the columns of $\mathbf{U}_2 \in \mathbb{R}^{p \times (p-q)}$ form an orthonormal basis for the null-space of \mathbf{H}^\top (see Appendix A.5). Thus, using eqn. (6.12)

$$\begin{aligned} \mathbf{p} &= \mathbf{U}_2^\top (\mathbf{y} - \mathbf{H}\hat{\mathbf{x}}) \\ &= (\mathbf{U}_2^\top \mathbf{e}_i)\mu_i + \mathbf{U}_2^\top \boldsymbol{\eta}; \end{aligned} \quad (6.15)$$

therefore, $\mathbf{p} \sim \mathcal{N}(\mu_i \mathbf{U}_2^\top \mathbf{e}_i, \sigma_y^2 \mathbf{I}_{p-q})$ (see [82]).

Then the magnitude of the outlier μ_i in eqn. (6.2) can be estimated as (see Section 5.6 of [58]),

$$\begin{aligned}\hat{\mu}_i &= ((\mathbf{U}_2^\top \mathbf{e}_i)^\top (\sigma_y^2 \mathbf{I})^{-1} (\mathbf{U}_2^\top \mathbf{e}_i))^{-1} (\mathbf{U}_2^\top \mathbf{e}_i)^\top (\sigma_y^2 \mathbf{I})^{-1} \mathbf{p} \\ &= \sigma_y^2 (\mathbf{e}_i^\top \mathbf{U}_2 \mathbf{U}_2^\top \mathbf{e}_i)^{-1} \frac{1}{\sigma_y^2} \mathbf{e}_i^\top \mathbf{U}_2 \mathbf{p} \\ &= \frac{\mathbf{e}_i^\top \mathbf{Q}^\top \mathbf{r}}{\mathbf{e}_i^\top \mathbf{Q}^\top \mathbf{e}_i},\end{aligned}$$

where $\mathbf{U}_2 \mathbf{U}_2^\top = \mathbf{Q} = (\mathbf{I} - \mathbf{P})$, and the covariance of $\hat{\mu}_i$ is

$$\text{Cov} \langle \hat{\mu}_i \rangle = (\mathbf{e}_i^\top \mathbf{Q}^\top \mathbf{e}_i)^{-1}.$$

Each time that \mathcal{H}_0 is rejected, outlier identification is executed iteratively for each i in the alternative hypothesis set, assuming a single outlier. Each μ_i is compared against a threshold γ , such that any $\mu_i > \gamma$ is considered an outlier. After completion of the identification process, if an outlier is identified, its' measurement is removed from the measurement-set. When \mathcal{H}_0 is accepted, then and the optimization process of Section 4.2 is performed.

6.2 Complexity

Given $2m$ GPS measurements at each time over a window of length L , there are $(2mL)$ GPS residuals in each CRT window. Therefore, there are

$$\sum_{k=1}^{2mL} \binom{2mL}{k} = \sum_{k=1}^{2mL} \frac{(2mL)!}{((2mL) - k)! k!},$$

ways that any number of satellite measurements could have outliers in any combination at one epoch (see Section 3 of [3]). For the EKF or Iterated EKF (IEKF), with $L = 1$ and $p = 9$, this results in 262,143 hypotheses, which is too large for full consideration. For the CRT with $L = 20$, consideration of all hypothesis is even more infeasible for real-time implementation. Therefore, simplified approaches are required. An example approach is to only consider single outlier occurrences, as discussed in the previous section, but to remove all measurements with residuals greater than a user defined threshold before completing the optimization.

6.3 Comparison of DOF's

This section compares the number of DOF (i.e., $(p - q)$) available for outlier detection between algorithms, where q is the total number of real variables to be estimated, p denotes the total number of available constraints, n_e is the error state dimension, and m_k is the number of satellite pseudoranges available at epoch k .

The EKF at any time step has $q = n_e$ variables to estimate (one state vector) and $p = n_e + 2m$ constraints (GPS and prior); therefore, the DOF is $2m$. The DOF of the IEKF is the same. The advantage of the IEKF is its ability to perform nonlinear iterative corrections [53, 68].

For the CRT algorithm with window length L , the number of variables to be estimated is $q = (L + 1)n_e$. The number of constraints is $p = (L + 1)n_e + 2mL$. The DOF is therefore, $2mL$. Both the outlier detection capability and the amount of required

computation increase with the DOF, which increase with L . Also, the ability to detect outliers and the potential number of outliers both increase with L .

Chapter 7

CRT using the Soft-Thresholding Operator

Recent advances in the vision-aided navigation community utilize outlier detection methods from the field of Robust Statistics, which involves alternative loss (cost) functions, and thresholding. For detection of multiple outliers simultaneously, Huber proposed a class of robust or resistant regressors based on maximum likelihood methods, called M -estimators [1, 50].

The authors of [71, 97, 104], using a sparse representation of candidate tracking sets for face recognition, demonstrate that l_1 -regularization can exploit the sparseness of outliers in a candidate dataset with redundant measurements to achieve enhanced performance.

7.1 Problem Formulation

This section develops the theory to adapt the soft-thresholding operator [71, 97] to the CRT problem in Chapter 4, we denote this as CRT-LSS. Complete derivations for this section are provided in [82].

7.1.1 Outlier Model

For the LSS approach, each component of \mathbf{s}_k in eqn. (3.5) is assumed to have *i.i.d.* Laplacian distributions [71, 97] and are assumed to be independent of \mathbf{x}_k , $\boldsymbol{\eta}_{y,k}$, \mathbf{w}_{k-1} :

$$p_{s_{\rho,k}}(s_{\rho,k}) = \frac{1}{2\nu_\rho} \exp\left[-\frac{|s_{\rho,k}|}{\nu_\rho}\right]$$

for pseudorange measurements and

$$p_{s_{d,k}}(s_{d,k}) = \frac{1}{2\nu_d} \exp\left[-\frac{|s_{d,k}|}{\nu_d}\right]$$

for Doppler measurements. Therefore

$$p_{\mathbf{s}_k}(\mathbf{s}_k) = \left(\frac{1}{4\nu_\rho\nu_d}\right)^m \prod_{j=1}^m \exp\left(-\left[\frac{|s_{\rho,j}|}{\nu_\rho} + \frac{|s_{d,j}|}{\nu_d}\right]\right).$$

To simplify notation later, let $\lambda_\rho = \frac{1}{\nu_\rho}$ and $\lambda_d = \frac{1}{\nu_d}$. The distribution of

$$p_{\mathbf{S}}(\mathbf{S}) = \prod_{n=k-L+1}^k p_{\mathbf{s}_n}(\mathbf{s}_n),$$

where $\mathbf{S} = \{\mathbf{s}_j \mid j \in [k-L+1, k]\}$ and $\mathbf{S} \in \mathbb{R}^{2mL \times 1}$.

7.1.2 Theoretical Solution

Modifying eqn. (4.1) to account for \mathbf{S} , the MAP estimate of the vehicle trajectory \mathbf{X} is:

$$\hat{\mathbf{X}} = \underset{\mathbf{X}, \mathbf{S}}{\operatorname{argmax}} \{p(\mathbf{X}, \mathbf{U}, \mathbf{Y}, \mathbf{S})\},$$

where within the time window $\mathbf{S} = \{\mathbf{s}_j \mid j \in [k - L + 1, k]\}$ and $\mathbf{S} \in \mathbb{R}^{2mL \times 1}$.

The GPS-INS joint probability of eqn. (4.5) is modified as:

$$p(\mathbf{X}, \mathbf{U}, \mathbf{Y}, \mathbf{S}) \propto p(\mathbf{X}, \mathbf{U}, \mathbf{S})p(\mathbf{Y} \mid \mathbf{X}, \mathbf{U}, \mathbf{S}) \quad (7.1)$$

$$= p(\mathbf{S})p(\mathbf{X}, \mathbf{U} \mid \mathbf{S})p(\mathbf{Y} \mid \mathbf{X}, \mathbf{U}, \mathbf{S}) \quad (7.2)$$

$$= p(\mathbf{S})p(\mathbf{X}, \mathbf{U})p(\mathbf{Y} \mid \mathbf{X}, \mathbf{U}, \mathbf{S}) \quad (7.3)$$

$$= p(\mathbf{S})p(\mathbf{X}, \mathbf{U})p(\mathbf{Y} \mid \mathbf{X}, \mathbf{S}) \quad (7.4)$$

$$= p(\mathbf{S})p(\mathbf{X}, \mathbf{U}) \prod_{j=k-L+1}^k p(\mathbf{y}_j | \mathbf{x}_j, \mathbf{s}_j) \quad (7.5)$$

$$= p(\mathbf{S})p(\mathbf{x}_{k-L}) \prod_{l=k-L}^{k-1} p(\mathbf{x}_{l+1} | \mathbf{x}_l, \mathbf{U}_l) \prod_{j=k-L+1}^k p(\mathbf{y}_j | \mathbf{x}_j, \mathbf{s}_j), \quad (7.6)$$

where $p(\mathbf{S})$ is the distribution which corresponds to the outlier.

The steps for the formal proof of eqn. (7.6) are as follows: Eqn. (7.1) is obtained by applying the definition of conditional probability. Eqn. (7.2) is obtained by applying the definition of conditional probability. Eqn. (7.3) is obtained by applying the conditional independence property. Eqn. (7.4) is obtained by applying the conditional independence property. Eqn. (7.5) is obtained by assuming the noise affecting the sequence of measurements is independent. Eqn. (7.6) is obtained by assuming Markov process and temporal independence of process noise. ■

7.1.3 Numerical Solution

Finding \mathbf{X} that maximizes eqn. (7.6) is equivalent to minimizing the negative of its natural logarithm. This yields the equivalent nonlinear cost function:

$$\begin{aligned}\mathcal{C}(\mathbf{X}, \mathbf{S}) = & \|\hat{\mathbf{x}}_{k-L} - \mathbf{x}(t_{k-L})\|_{\mathbf{P}_{(k-L)}}^2 \\ & + \sum_{l=k-L}^{k-1} \|\Phi(\mathbf{x}(t_l), \mathbf{U}_l) - \mathbf{x}(t_{l+1})\|_{\mathbf{Q}_D}^2 \\ & + \sum_{j=k-L+1}^k \left(\frac{1}{\nu_\rho} \|\mathbf{s}_\rho(t_j)\|_1 + \frac{1}{\nu_d} \|\mathbf{s}_d(t_j)\|_1 \right) \\ & + \sum_{j=k-L+1}^k \|\mathbf{y}(t_j) - \mathbf{h}_j(\mathbf{x}(t_j)) - \mathbf{s}(t_j)\|_{\mathbf{R}}^2.\end{aligned}\quad (7.7)$$

To simplify notation later, let $\psi_{\rho,j} = \frac{\mathbf{s}_\rho(t_j)}{\nu_\rho} \in \mathbb{R}^m$, and $\psi_{d,j} = \frac{\mathbf{s}_d(t_j)}{\nu_d} \in \mathbb{R}^m$, and $\psi_j = \psi(\mathbf{s}(t_j)) = [\psi_{\rho,j}^\top, \psi_{d,j}^\top]^\top$. Also, let $\Psi(\mathbf{S}) = \{\psi_j \mid j \in [k-L+1, k]\}$ and $\Psi \in \mathbb{R}^{2mL \times 1}$.

Define $\Sigma_{\mathbf{R}}^\top \Sigma_{\mathbf{R}} = \mathbf{R}^{-1}$ and $\Sigma_{\mathbf{S}} = \text{blkdiag}(\mathbf{0}, \mathbf{0}, \Sigma_{\mathbf{R}})$, where $\Sigma_{\mathbf{R}}$ is upper-triangular.

The cost function $\mathcal{C}(\mathbf{X}, \mathbf{S})$ can be normalized using Cholesky Decomposition, such that the minimization problem of eqn. (7.7) reduces to the optimization of

$$\mathcal{C}(\mathbf{X}, \mathbf{S}) = \|\mathbf{z} - \mathbf{g}(\mathbf{X}) - \Sigma_{\mathbf{S}} \mathbf{S}\|_2^2 + \|\Psi\|_1,\quad (7.8)$$

where

$$\mathbf{z} = \Sigma_{\mathbf{W}} [\hat{\mathbf{x}}_{k-L}^\top, \mathbf{0}^\top, \mathbf{Y}^\top]^\top$$

represents the terms that are known at each iteration and

$$\mathbf{g}(\mathbf{X}) = \Sigma_{\mathbf{W}} [\mathbf{x}(t_{k-L})^\top, \Phi(\mathbf{X}, \mathbf{U})^\top - \mathbf{X}^\top, \mathbf{h}(\mathbf{X})^\top]^\top$$

represents the terms that are computed based on \mathbf{X} .

Eqn. (7.8) will be minimized iteratively, by the algorithm discussed in Section 7.2.

7.2 Solution of CRT with Soft-Thresholding

The discontinuity of the l_1 -norm in eqn. (7.8) complicates its minimization. The authors of [71, 97] provide the derivation of the Soft-Thresholding Operator for the linear case. Eqn. (7.8) can be optimized by methods similar to those of [71, 97], as derived below. Because the l_1 -norm is not differentiable at its minimum, the optimal solution to $\mathcal{C}(\mathbf{X}, \mathbf{S})$ is solved in two parts.

7.2.1 Part 1: Estimate \mathbf{X} , holding $\hat{\mathbf{S}}$ constant

Given $\hat{\mathbf{S}}$, the optimal value of \mathbf{X} is

$$\begin{aligned}\mathbf{X}^* &= \arg \max_{\mathbf{X}} \mathcal{C}(\mathbf{X}, \hat{\mathbf{S}}) \\ &= \arg \max_{\mathbf{X}} \left\{ -\frac{1}{2} \|\mathbf{z} - \mathbf{g}(\mathbf{X}) - \Sigma_{\mathbf{S}} \hat{\mathbf{S}}\|_2^2 + \|\hat{\Psi}\|_1 \right\} \\ &= \arg \max_{\mathbf{X}} \left\{ -\frac{1}{2} \|(\mathbf{z} - \Sigma_{\mathbf{S}} \hat{\mathbf{S}}) - \mathbf{g}(\mathbf{X})\|_2^2 \right\},\end{aligned}\quad (7.9)$$

where $\hat{\Psi} = \Psi(\hat{\mathbf{S}})$. This optimization can be solved iteratively, starting from an initial value $\hat{\mathbf{X}}$, using a Taylor series expansion to approximate $\mathbf{g}(\mathbf{X})$,

$$\mathbf{g}(\mathbf{X}) = \mathbf{g}(\hat{\mathbf{X}}) + \mathbf{G}\delta\mathbf{X} + h.o.t's,\quad (7.10)$$

where the Jacobian $\mathbf{G} \doteq \frac{\partial \mathbf{g}(\mathbf{X})}{\partial \mathbf{X}} \Big|_{\mathbf{X}=\hat{\mathbf{X}}}$, and $\delta\mathbf{X} \in \mathbb{R}^{ne(L+1)}$. Substituting eqn. (7.10) into eqn. (7.9) and ignoring the higher order terms ($h.o.t's$), yields

$$\begin{aligned}\delta\mathbf{X}^* &= \arg \min_{\delta\mathbf{X}} \|(\mathbf{z} - \Sigma_{\mathbf{S}} \hat{\mathbf{S}}) - (\mathbf{g}(\hat{\mathbf{X}}) + \mathbf{G}\delta\mathbf{X})\|_2^2 \\ &= \arg \min_{\delta\mathbf{X}} \|\mathbf{b} - \mathbf{G}\delta\mathbf{X}\|_2^2\end{aligned}$$

where in this section \mathbf{b} is defined as

$$\mathbf{b} \doteq \mathbf{z} - \boldsymbol{\Sigma}_{\mathbf{S}} \hat{\mathbf{S}} - \mathbf{g}(\hat{\mathbf{X}}). \quad (7.11)$$

Then, the optimal $\delta\mathbf{X}$ solves

$$\mathbf{G}\delta\mathbf{X}^* = \mathbf{b}. \quad (7.12)$$

in the least squares sense. The update to the trajectory is performed using eqn. (4.16).

Optimization with respect to $\hat{\mathbf{X}}$ is obtained by iterating eqns. (7.10), (7.11), and the solution of (7.12), to convergence for some user defined stopping conditions. A line search is implemented in the direction of $\delta\mathbf{X}^*$ from eqn. (7.12) to determine the magnitude of the update step in eqn. (4.16).

7.2.2 Part 2: Estimate \mathbf{S} , holding $\hat{\mathbf{X}}$ constant

Given an estimate $\hat{\mathbf{X}}$, the optimal value of \mathbf{S} is

$$\begin{aligned} \mathbf{S}^* &= \arg \max_{\mathbf{S}} \mathcal{C}(\hat{\mathbf{X}}, \mathbf{S}) \\ &= \arg \max_{\mathbf{S}} \left\{ -\frac{1}{2} \|\mathbf{z} - \mathbf{g}(\hat{\mathbf{X}}) - \boldsymbol{\Sigma}_{\mathbf{S}} \mathbf{S}\|_2^2 + \|\boldsymbol{\Psi}(\mathbf{S})\|_1 \right\} \\ &= \arg \max_{\mathbf{S}} \left\{ -\frac{1}{2} \|\mathbf{c} - \bar{\mathbf{S}}\|_2^2 + \|\boldsymbol{\Psi}(\mathbf{S})\|_1 \right\}, \\ &= \arg \min_{\mathbf{S}} \sum_i \left[\frac{1}{2} (c_i - \bar{s}_i)^2 + \|\psi(s_i)\|_1 \right], \end{aligned} \quad (7.13)$$

where $\bar{\mathbf{S}} = \boldsymbol{\Sigma}_{\mathbf{S}} \mathbf{S}$, and $\mathbf{c} = \mathbf{z} - \mathbf{g}(\hat{\mathbf{X}})$ is independent of \mathbf{S} . In eqn. (7.13), the non-boldface quantities c_i , \bar{s}_i , and $\psi(s_i)$ denote the scalar elements of the vectors in the previous equation.

Each term in the summation in eqn. (7.13) only depends on c_i , \bar{s}_i , and $\psi(s_i)$, thus each term can be optimized independently¹:

$$\hat{s}_i = \arg \min_{s_i} \left\{ \frac{1}{2} (c_i - \bar{s}_i)^2 + |\psi(s_i)| \right\} \quad (7.14)$$

The closed-form solution of the optimization problem in eqn. (7.14) is the soft-thresholding operation (see eqn. 16 of [97]) resulting in two equations, one for pseudorange and one for Doppler:

$$\hat{s}_{\rho,i} = \sigma_\rho \operatorname{sgn}(c_i) \max \left(|c_i| - \frac{\sigma_\rho}{\nu_\rho}, 0 \right), \quad (7.15)$$

$$\hat{s}_{d,i} = \sigma_d \operatorname{sgn}(c_i) \max \left(|c_i| - \frac{\sigma_d}{\nu_d}, 0 \right), \quad (7.16)$$

where $\operatorname{sgn}(\cdot)$ represents the *signum* function. The values σ_ρ and σ_d represent the standard deviation of the pseudorange and Doppler distributions, respectively. The proof for eqn. (7.15) is provided in Appendix A.9.

7.2.3 CRT-LSS Summary

Implementation of Sections 7.2.1 and 7.2.2 is summarized in Algorithm 1.

Algorithm 1 Least Soft-threshold Squares Regression

```

1: Given initial  $\hat{\mathbf{X}}$  and  $\hat{\mathbf{S}}$ . Initialize  $i = 0$ .
2: while  $((\|\delta\mathbf{X}\|_2 \& \|\delta\hat{\mathbf{S}}\|_2) > 1 \times 10^{-3}) \& (i < 20)$ 
3:    $i = i + 1$ 
4:   Compute  $\delta\mathbf{X}$  and  $\hat{\mathbf{X}}^+ = \hat{\mathbf{X}}^- \oplus \delta\mathbf{X}$  (eqns. (7.11), (7.12)).
5:   if  $(\|\delta\mathbf{X}\|_2 < 1 \times 10^{-3})$ 
6:     Compute  $\hat{\mathbf{S}}$  using eqns. (7.15) & (7.16).
7:     (Optional) Compute  $\delta\mathbf{X}$  and  $\hat{\mathbf{X}}^+ = \hat{\mathbf{X}}^- \oplus \delta\mathbf{X}$  (eqns. (7.11), (7.12)).
8:   end
9: end
```

¹When \mathbf{R} and hence $\Sigma_{\mathbf{R}}$ are diagonal, this is obvious. When \mathbf{R} is not diagonal, the fact that $\Sigma_{\mathbf{R}}$ is upper-diagonal allows (7.13) to be solved one component at a time using back-substitution. For brevity, the algorithm below only presents the diagonal case.

In Section 7.2.1 the value of the cost function $\mathcal{C}(\mathbf{X}, \mathbf{S})$ is decreased by changing only \mathbf{X} , even if multiple nonlinear least squares iterations occur. In Section 7.2.2 the value of the cost function $\mathcal{C}(\mathbf{X}, \mathbf{S})$ is decreased by changing only \mathbf{S} , only a single iteration is required, and $\delta\hat{\mathbf{S}}$ is the final \mathbf{S} minus the initial \mathbf{S} . Therefore, at each iteration, the cost function is decreased and is bounded below. Ultimately at least a local minimum of the cost function will be attained. Note that line 7 of Algorithm 1 is not necessary, but is useful for analyzing the convergence of the cost function $\mathcal{C}(\mathbf{X}, \mathbf{S})$.

The combined operation of Sections 7.2.1 and 7.2.2 are equivalent to the Huber Loss function (see [97], [50]).

Chapter 8

Experimental Results

8.1 Background

In this chapter, both the CRT-HT and CRT-LSS algorithm performance is evaluated in two steps:

1. Synthetic-sensor data is used to evaluate algorithm performance under controlled conditions where ground truth and outliers are known.
2. Real-sensor data is used to demonstrate algorithm performance under real-world conditions, where ground truth is estimated.

8.1.1 Synthetic Data

The synthetic-data is a simulated 515 second automobile trajectory generated by a signal generator incorporating a 6DOF kinematic model to produce both ground truth and noise-corrupted IMU and GPS “measurements.” The simulated trajectory is similar to the real-world trajectory discussed below.

IMU measurements $\tilde{u}_i(t)$ for the i^{th} axis of the gyroscope and accelerometer were generated at $200Hz$ according to the sensor model (Ch. 11.6 of [25]):

$$\tilde{u}_i(t) = (1 + \epsilon_i)[u_i(t) + b_i(t) + \eta_{RW,i} + \eta_{MA,i}],$$

where $u_i(t)$ is actual acceleration (or angular rotation rate) for axis i , $\eta_{RW,i}$ is white noise, ϵ_i is the scale factor error, and $\eta_{MA,i}$ is the misalignment error. The time-correlated error (i.e., bias) $b_i(t)$ has a random initial value and performs a random walk over time with driving noise $\eta_{RRW,i}$. The accelerometer has $\sigma_{RW} = 0.05 \text{ (m/s)/}\sqrt{\text{Hr}}$, bias variation = 15 *milli-g*, and bias stability = 0.1 *milli-g*. The constant along-axis scale-factor errors are 200 *parts-per-million (ppm)*, and cross-axis scale-factor errors are 150 *ppm*. The gyro was modeled with angle random walk parameter $\sigma_{RW} = 0.1 \text{ deg}/\sqrt{\text{Hr}}$, bias variation = 3.0 *deg/Hr*, and bias stability = 1.0 *deg/Hr*. The constant along-axis g-sensitivity errors are 2 *deg/Hr/g*, along-axis scale-factor errors are 200 *ppm*, and cross-axis scale-factor errors are 150 *ppm*.

The GPS signal generator provided L1 pseudorange and Doppler measurements at 1*Hz* for both the vehicle and base station using the models in Sections 8.2 and 8.3 of [25]. Satellite vehicle orbits were produced from Receiver Independent Exchange (RINEX) ver. 2.10 [44] files downloaded from a Continuously Operating Reference Station (CORS) server [88], and valid for January 10, 2017, between 9:00-10:00 am local time.

8.1.2 Experimental Data

Real-world performance is evaluated using a 515 second drive-test data around the University of California, Riverside campus. While driving, the sensor data is time-stamped and stored. The sensor data includes: a MEMS IMU (Nav Technology Co., Ltd. NV-IMU100) which outputs specific force and angular rate measurements at 200*Hz*, and an L1/L2 GPS receiver (NovAtel OEMV3) which outputs pseudorange, Doppler, and carrier phase measurements at 1*Hz*. A GPS antenna (Leica AT502-667126) is mounted on the

vehicle roof. Differential corrections were obtained in real-time, via cellular connection, from the UC Riverside NTRIP [34] caster (`ntrip.engr.ucr.edu:2101`), which broadcasts raw dual frequency GPS measurements (Message 1004 in RTCM3.1 standard) and the base position (Message 1006 in RTCM3.1 standard) publicly over the internet at 1Hz and 0.1Hz , respectively [83]. The base station uses the same model of GPS receiver and antenna as the vehicle, and runs both the NTRIP Server and NTRIP Caster (both developed in C++) in Linux (Ubuntu 12.04) on a mini-desktop computer with an Ethernet connection. The trajectory contains a variety of real-world conditions that can adversely affect GPS receiver performance, e.g. tall buildings and trees, thereby producing measurement outliers. Fig. 8.1 shows snapshots along this trajectory. The test setup is shown in Fig. 8.2. The number of satellites available (after double differencing), satellite ID, and elevation angles are shown in Fig. 8.3.

8.1.3 Ground Truth

For the experimental data, the *ground truth* trajectory is found by solving a non-linear MAP optimization problem over the entire (515 second) trajectory using the L1/L2 integer-resolved carrier phase DGPS and IMU measurements to achieve centimeter level ground truth accuracy [96].

8.1.4 Final Comments

To allow direct comparison of the performance of various algorithms, using identical input data, the results of this section are computed during post-processing. Even though running in post-processing for this evaluation, each algorithm is written in C++ to run in real-time, using only the data and prior as would be applicable for each approach.

These real-time navigation algorithms only use L1 GPS with differential corrections, and IMU data.

At the start of the experiment, the vehicle is stationary and pointed approximately north. The estimated yaw angle is initialized to 180° (i.e., south). During the first one second of this stationary period, the initial roll and pitch are computed from the direction of the specific-force (i.e, gravity) vector. The initial position is obtained by least-squares using the first GPS double-differenced L1 pseudorange measurement. The initial biases and velocity values are all zero.

8.2 CRT-HT Performance

8.2.1 CRT-HT Performance using Synthetic Data

Using the simulated trajectory, 216 simulations were run consisting of: six injected outlier magnitudes ($O = \{1.0, 1.5, 2.0, 2.5, 5.0, 10.0\}m$), six CRT window lengths ($L = \{1, 5, 10, 20, 30, 40\}$), and six threshold values ($\gamma = \{0.75, 1.00, 1.25, 1.50, 2.00\}$).

To simulate driving near trees or past a tall building, *multiple simultaneous outliers* were added at three known trajectory locations. The outliers persisted for five seconds. The outliers were added to three of the ten available pseudorange measurements representing satellites that were visible in one quadrant of the sky. The minimum outlier magnitude of $1.0m$ was selected such that the outlier is similar in magnitude to double-differenced pseudorange measurement noise.

Fig. 8.4 presents the receiver operating characteristic (ROC) curve for several algorithms, e.g. IEKF and CRT-HT with length L . Each ROC curve plots the Probability of Correct Detection for one setting of O and L (for CRT-HT), versus Probability of False

Alarm, as a function of γ .

Since this is simulation, the correct outlier decisions are known for each satellite at each epoch. To construct the ROC curve for each algorithm and each outlier magnitude, the procedure discussed in the next paragraph is repeated once for each specified value of γ . The outlier detection decisions for each algorithm (IEKF and CRT-HT with length L) and each value of γ are compared with the known correct decisions to compute P_{CD} and P_{FA} . Each simulation for a single value of γ generates one point on the ROC curve.

For example, to evaluate the CRT-HT $L = 5$, a significance threshold α is chosen and γ is computed, then the CRT-HT is run for the entire trajectory. At the completion of the trajectory, the P_{CD} (of outliers) is calculated, as well as the P_{FA} , and the values are recorded. This provides one point on the CRT-HT $L = 5$ ROC curve. The trajectory estimation is repeated for a vector of α values. This set of values provides the CRT-HT $L = 5$ ROC curve. This process is performed for each outlier magnitude, and each estimator, e.g. IEKF, and CRT-HT with $L = \{5, 10, 20, 30, 40\}$. For clarity of the graph, only IEKF and CRT-HT $L = \{5, 10, 40\}$ are shown here, however the trends for $L = \{20, 30\}$ are similar. The outlier detection algorithm evaluates the entire residual vector before optimization of the trajectory. If outliers are detected, the corresponding measurements are removed, and the optimization is performed. Upon sliding the window, the outliers from the previous time-window are ignored and the detection procedure searches the entire residual vector.

Each curve in Fig. 8.4 displays P_{CD} vs. P_{FA} . The trends for γ are as expected. As γ increases, the next point on each curve will be below and to the left of the last point, as P_{CD} and P_{FA} both decrease as γ increases. As Fig. 8.4 shows, the rates of decrease are very different for each algorithm. Curves closer to the upper left corner show improved

ability to detect outliers with lower probability of injecting false alarms.

The advantage of increasing the CRT-HT window length is demonstrated by the increase in P_{CD} and decrease in P_{FA} as L increases. For example in Fig. 8.4, consider points P_1 and P_2 . Both points have outlier magnitude of $2.0m$ and $\gamma = 1.25$. Point P_1 for the IEKF has $P_{CD} = 48\%$ and $P_{FA} = 12\%$, whereas point P_2 for the CRT-HT $L = 5$ has $P_{CD} = 75\%$ and $P_{FA} = 8\%$. While both algorithms perform nonlinear optimization, it is the window length that contributes to the 27% increase in P_{CD} and a 4% decrease in P_{FA} . As CRT-HT window length increases, for a given value of γ P_{CD} increases and P_{FA} decreases.

This confirms the claim that the ability of the CRT-HT algorithm to discriminate outliers from valid data is enhanced with the length of the sliding window, which increases the redundancy as quantified by the number of degrees of freedom. The reliability of achieving a specified level of accuracy increases with the ability to remove outliers.

8.2.2 CRT-HT Performance using Experimental Data

For each algorithm (EKF, IEKF and CRT-HT with length L), Fig. 8.5 shows the cumulative distribution function (CDF) of the position error norm $\|\hat{\mathbf{p}}_k - \mathbf{p}_k\|$ at 1 Hz where the ground truth trajectory is used for \mathbf{p}_k and $\hat{\mathbf{p}}_k$ is the result of the optimization at the first time when the k -th epoch enters the sliding window. For outlier removal, $\gamma = 1.25$. The CRT-HT algorithm curves are included for various window lengths L .

Fig. 8.5 shows that the percentage of occurrences where the EKF position error is less than $0.1m$, is roughly 18%. Roughly 90% of the EKF trajectory has errors less than $1.0m$. Figs. 8.5 also indicate that accuracy improves from the EKF to the IEKF to

the CRT-HT. Also, CRT-HT performance (generally) improves with the window length L . For the CRT-HT with $L > 5$, 100% of the position errors are less than $1.0m$. CRT-HT algorithms with $L > 20$ each achieve $0.6m$ position accuracy on 100% of the trajectory. The EKF and IEKF CDF plots do not reach 100% until the position accuracy is greater than $3.0m$.

To gain insight into the status of the CRT-HT estimator with, for example $L = 20$, several key variables are plotted versus GPS epoch in Fig. 8.7. The figure shows the total number of iterations, the final $\|\mathcal{C}(\hat{\mathbf{X}})\|_2$, number of satellites measurements available and removed, the 2D position error, and the per-epoch Geometric Dilution of Precision (GDOP) and per-window GDOP. At the start of the trajectory it takes more iterations to converge from the initial \mathbf{X}_0 to an estimate $\hat{\mathbf{X}}$ (see eqn. (4.16)) such that $\delta\mathbf{X}$ lies within the unobservable space. Due to the initial inaccuracy of \mathbf{X}_0 , the error within the unobservable space may be large. Additionally, the initial covariance is large, and the uncertainty in the state estimate, in particular yaw, remains large until the vehicle accelerates.

For example, in Fig. 8.8 the true yaw is unknown and initialized to -179° , and remains unobservable until the vehicle accelerates at $t = 20sec$. Upon acceleration from the stationary initialization point, the biases and attitude errors become observable, and the effect of the nonlinearities can be significant. This effect is observed in the spike in the number of iterations in Fig. 8.7 shortly after acceleration. The biases and attitude errors can be more accurately estimated at this point because the unobservable subspace changes or becomes null.

To demonstrate the CRT optimization performance, in Fig. 8.8 the initial yaw error was -179° , yet just after acceleration the yaw error is less than 1° . This emphasizes

the ability of the CRT estimator to correct errors that are large relative to the curvature of the nonlinearities. In contrast, the EKF diverges with large initial yaw errors, and for this reason was not included in Fig. 8.8. The EKF is therefore initialized (for all tests) using ground truth, with an initial yaw error of approximately 1° . In real-time situations, the initial yaw can be determined from a compass.

After the CRT state estimates become accurate, fewer iterations are needed. An average of just three iterations are required for most of the trajectory, even in challenging areas, e.g. $t \in [160, 180]$ where either tall buildings and overhead foliage are present. A notable exception is at $t = 415\text{sec}$ where the vehicle traverses a narrow corridor between tall structures, and only one line-of-sight GPS satellite is available. As a consequence, additional iterations are required to accommodate likely multipathed measurements from six (of seven available) satellites just prior to the corridor. Throughout the trajectory the final $\|\delta\hat{\mathbf{X}}\|_2$ is always less than the threshold $\epsilon = 10^{-3}$. Consider both $\boldsymbol{\xi}$ and $\delta\hat{\mathbf{X}}$. The vector $\boldsymbol{\xi}$ is a projection of the residual vector onto a subspace with the same dimension as $\delta\hat{\mathbf{X}}$ (see eqns. (4.14) and (4.15)). Because $\boldsymbol{\Xi}$ is nonsingular, the final norms of $\delta\hat{\mathbf{X}}$ and $\boldsymbol{\xi}$ should both be near zero when the trajectory estimate is near any local minimum of the cost function $\mathcal{C}(\hat{\mathbf{X}})$. In practice, the inconsistent GPS data, possibly caused by multipath or overhead foliage, could explain the large values of the final $\|\mathcal{C}(\hat{\mathbf{X}})\|_2$ and final $\|\boldsymbol{\xi}\|_2$.

During $t \in [160, 180]$, initially the $\|2\text{D Pos. Error}\|_2$ increases because only one satellite is available. The $\|2\text{D Pos. Error}\|_2$ continues to increase as bad satellite measurements are removed, then returns to sub-meter error when good satellite measurements are available. Note that during this period, the per-epoch GDOP is at maximum value (set to 100) because a minimum of four satellites are necessary to compute GDOP (this

explains the other instances when GDOP is large). However, the per-window GDOP during this period is sub-meter because the computation includes all satellites available within the window.

During other periods of the trajectory, e.g. $t \in [230, 240], [380, 410], [440, 450]$, where $\|2D\text{ Pos. Error}\|_2$ is larger than one-meter, the per-epoch GDOP is large due to either too few satellites or poor constellation geometry. An example of likely poor constellation geometry is $t \in [380, 410]$, where four satellites are available, but $\|2D\text{ Pos. Error}\|_2$ is larger than one-meter. Note that position error is sub-meter for $> 95\%$ of the trajectory.

8.3 CRT-LSS Performance

8.3.1 Specification of Laplacian Parameters

The distribution of the outliers is not known. The CRT-LSS derivation of Section 7.1.1 assumed a Laplacian distribution. For implementation, reasonable values for the parameters of that distribution need to be specified. Our approach is to specify the standard deviation of the Laplacian outlier to match a multiple of the standard deviation assumed for the Gaussian noise. For the Laplacian distribution, the standard deviation $\sigma_{\mathcal{L}}$ is related to the parameter ν according to $\sigma_{\mathcal{L}} = \sqrt{2}\nu$.

Let $\sigma_{\mathcal{L}_\rho}$ and $\sigma_{\mathcal{L}_d}$ denote the standard deviation of the pseudorange and Doppler outliers. Let $\sigma_{\mathcal{N}_\rho}$ and $\sigma_{\mathcal{N}_d}$ denote the standard deviation of the pseudorange and Doppler measurements. Setting $\sigma_{\mathcal{L}_\rho} = \lambda\sigma_{\mathcal{N}_\rho}$ and $\sigma_{\mathcal{L}_d} = \lambda\sigma_{\mathcal{N}_d}$ yields $\nu_\rho = \frac{\lambda}{\sqrt{2}}\sigma_{\mathcal{N}_\rho}$ and $\nu_d = \frac{\lambda}{\sqrt{2}}\sigma_{\mathcal{N}_d}$. This selection of the Laplace distribution parameters will cause residuals $\frac{\lambda}{\sqrt{2}}$ larger than the expected Normal standard deviation to be soft-thresholded.

8.3.2 CRT-LSS Performance using Synthetic Data

Similar to the process discussed in Section 8.2.1, 216 simulations were performed, wherein the value of λ was selected and held constant for the entire trajectory. This process is repeated for a set of values of λ , for each estimator and outlier magnitude to evaluate sensitivity of P_{CD} vs. P_{FA} versus λ for each algorithm. Due to space constraints, only position and attitude error are discussed herein. The results for velocity error are provided in Section 6 of [82].

The CRT-LSS algorithm does not perform detection in the same sense as the CRT-HT algorithm. Therefore the values for P_{CD} and P_{FA} are computed relative to ground truth using the indices where $\hat{\mathbf{S}}$ is non-zero, e.g. measurements which required soft-thresholding (see line 6 of Alg. 1).

Each curve in Fig. 8.9 displays the expected P_{CD} vs. P_{FA} trends versus λ . As λ increases, the next point on each curve will be below and to the left of the last point. Therefore, P_{CD} and P_{FA} both decrease with increasing λ (this is similar to the result for γ in Section 8.2.1). This is because, with increasing the λ value, larger residuals will not be soft-thresholded, therefore both P_{CD} and P_{FA} will decrease. Curves closer to the upper left corner show improved ability to accommodate outliers with lower probability of injecting false alarms.

The advantage of increasing the CRT-LSS window length is demonstrated in the increase in P_{CD} and decrease in P_{FA} for a given value of λ . For example in Fig. 8.9, consider two points P_1 and P_2 each with the outlier magnitude of $2.0m$ and $\lambda_\rho = 1.0$. For the IEKF $P_{CD} = 52\%$ and $P_{FA} = 14\%$, whereas for the CRT-LSS $L = 5$ the $P_{CD} = 70\%$

and $P_{FA} = 12\%$. While both algorithms perform nonlinear optimization, it is the window length that contributes to the 18% increase in P_{CD} and a 2% decrease in P_{FA} . As CRT-LSS window length increases, the P_{CD} increase and P_{FA} decrease.

8.3.3 CRT-LSS Performance using Experimental Data

Figs. 8.10 shows the cumulative distribution functions (CDF) of the norm of the position error $\|\hat{\mathbf{p}}_k - \mathbf{p}_k\|$ for various estimation algorithms. For outlier accommodation in this section, $\lambda = 1.00$. The EKF curves use hypothesis testing while the IEKF and CRT curves use LSS. Fig. 8.10 shows that the CRT-LSS performance improves with the window length L . For example, in the CRT-LSS approach with $L > 5$, 97% of the position errors are less than $1.0m$. The CRT-LSS algorithms with $L > 10$ each achieve $1.0m$ position accuracy on 100% of the trajectory. Alternatively, the IEKF CDF plots do not reach 100% until the position accuracy is greater than $3.0m$.

Similar to the results discussed in Section 8.2.2 for Fig. 8.7, several key variables are plotted versus GPS epoch in Fig. 8.12 for the CRT-LSS estimator with $L = 20$. The figure shows the total number of iterations, final $\|\mathcal{C}(\mathbf{X}, \mathbf{S})\|_2$ and $\|\hat{\mathbf{S}}\|_1$, the number of available and number of thresholded satellite measurements, $\|2D\ Pos. Error\|_2$ and estimated position standard deviation, and both per-epoch GDOP and CRT-window GDOP (i.e. computed using all SVs in the CRT window). The CRT-LSS estimator initially has additional iterations until the vehicle accelerates at $t = 20sec$. An average of three iterations are needed throughout the trajectory, even during periods of probable outliers.

Consider $t \in [310, 340]$ where GPS signal path is influenced by overhead foliage or buildings. Here, the $\|\mathcal{C}(\mathbf{X}, \mathbf{S})\|_2$, $\|\hat{\mathbf{S}}\|_1$, and number of iterations increase due to suspected

outliers. This demonstrates a desired attribute of CRT-LSS method, whereby outliers are accommodated with minimal additional iterations, thereby reducing the overall (per-epoch) computational burden.

While the algorithm is different than the one used in Fig. 8.7, the position error and GDOP results are similar in both Figs 8.7 and 8.12, and discussed in detail in Section 8.2.2. Note that position error is sub-meter for $> 95\%$ of the trajectory.

8.4 Comparison: CRT-LSS vs. CRT-HT

As shown in Figs. 8.4 and 8.9, outlier magnitudes greater than $2.0m$ range error, can be accommodated with $P_{CD} > 85\%$ by either outlier detection method. In fact, for CRT-HT or CRT-LSS with $L \geq 20$, the $P_{CD} > 85\%$ with $P_{FA} < 12\%$. The primary difference between Figs. 8.4 and 8.9 is the CRT-HT has a lower overall P_{FA} rate (versus the CRT-LSS) due to the method by which outliers are determined and the values selected for γ and λ_ρ , however the difference is $< 8\%$.

Note that the range of values for γ and λ_ρ are not a recommended range for the designer, but rather a set of values which provide a clear visualization of the P_{CD} vs. P_{FA} for each CRT-HT or CRT-LSS window length. Actual values depend on the expected or measured standard deviation of the GPS pseudorange measurements.

In Figs. 8.4 and 8.9, two key results are realized.

1. Increasing CRT (LSS or HT) window length L guarantees better outlier accommodation performance, with P_{CD} approaching 100%, and P_{FA} less than 25%.
2. As outliers exceed $2.5m$, the $P_{CD} = 100\%$ regardless of the CRT (LSS or HT) window length.

Considering Figs. 8.5 and 8.10, where $\gamma = 1.25$ and $\lambda_\rho = 1.00$, both of which produce an anticipated $P_{CD} > 50\%$ (based on synthetic data test results for outlier magnitudes $> 1.5m$), the position error is $< 1.0m$ for 90% of the trajectory for all algorithms (CRT $L = \{1, 5, 10, 40\}$) regardless of the outlier detection method (either HT or LSS). This is a subtle but important result, as we desire the $P_{CD} = 100\%$ regardless of P_{FA} . Here the worst case $P_{FA} < 12\%$.

From the perspective of outlier accommodation, the data indicate that both methods (CRT-HT and CRT-LSS) produce equivalent results. However, the numerical implementation of CRT-HT is a compromise of theory and practicality, whereas the CRT-LSS is a direct numerical implementation of the theory. As discussed in Section 6.2, the complete alternate hypothesis testing procedure is infeasible in real-time with CRT-HT window $L > 1$, therefore a modified approach is implemented numerically. Alternatively, the soft-thresholding approach of [71, 97] as adapted to the CRT problem in Section 7.2 does not remove any measurements. Instead, the CRT-LSS automatically detects which residuals should be soft-thresholded in a manner that guarantees convergence of the MAP optimization for each time window, accounting for outliers.

Due to the modified approach used in CRT-HT, the computational cost is similar to CRT-LSS (see Chapter 5). Both methods have similar performance with respect to P_{FA} and P_{CD} , as well as position and attitude error for a given window length L .

The CRT estimator (HT or LSS) has several advantages over the EKF which are summarized here:

1. CRT has the ability to change the linearization point of the trajectory within the CRT window. For the EKF the linearization point is the prior. Errors in the prior if large

relative to the higher order terms of the linearization can cause the EKF to diverge.

2. In the CRT approach, multiple iterations, each with re-linearization, are possible to fully address the nonlinearities in the MAP optimization, whereas the EKF performs a single iteration per measurement.
3. The improved performance demonstrated in Figs. 8.4–8.12 is attributed to solving the full nonlinear optimization over a longer window with outlier accommodation. The longer window enhances the redundancy and allows reconsideration of fault decisions, as long as the measurement data is within the sliding window. The standard EKF utilizes a single epoch. Thus an incorrect fault decision can be catastrophic and the redundancy available is often insufficient to make confident fault decisions.

This enhanced ability to accommodate outliers to achieve reliable performance is one of the major motivations of the CRT approach.

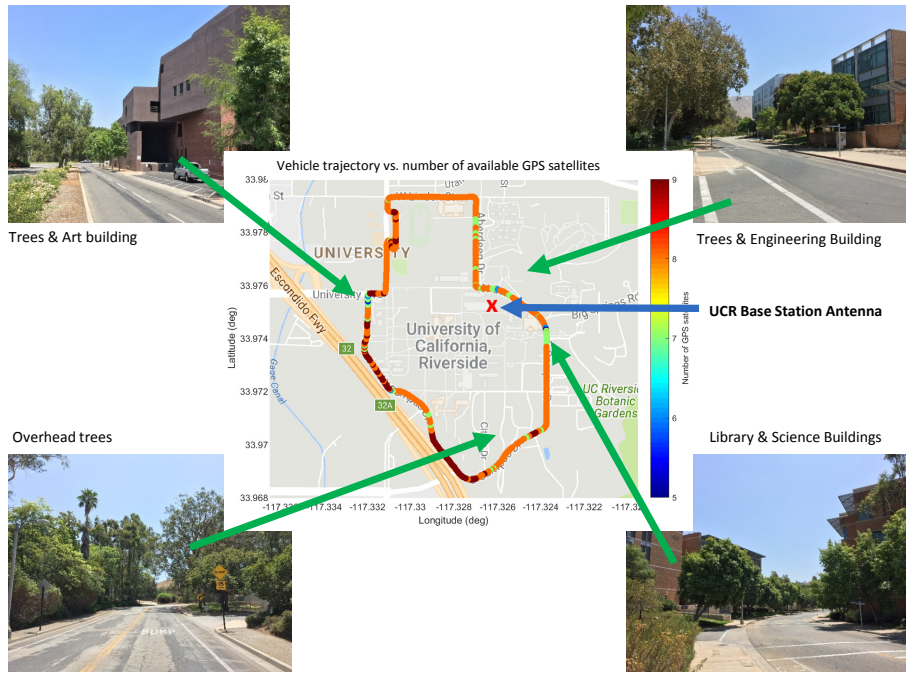


Figure 8.1: Test trajectory around UCR campus. The corner photos identify a variety of real-world environmental factors which adversely affect the performance of a GPS receiver, e.g. trees and tall buildings. The center image shows the number of satellites *available* along the trajectory for estimation and outlier detection. The UCR base station antenna position is shown with a red ‘X’.

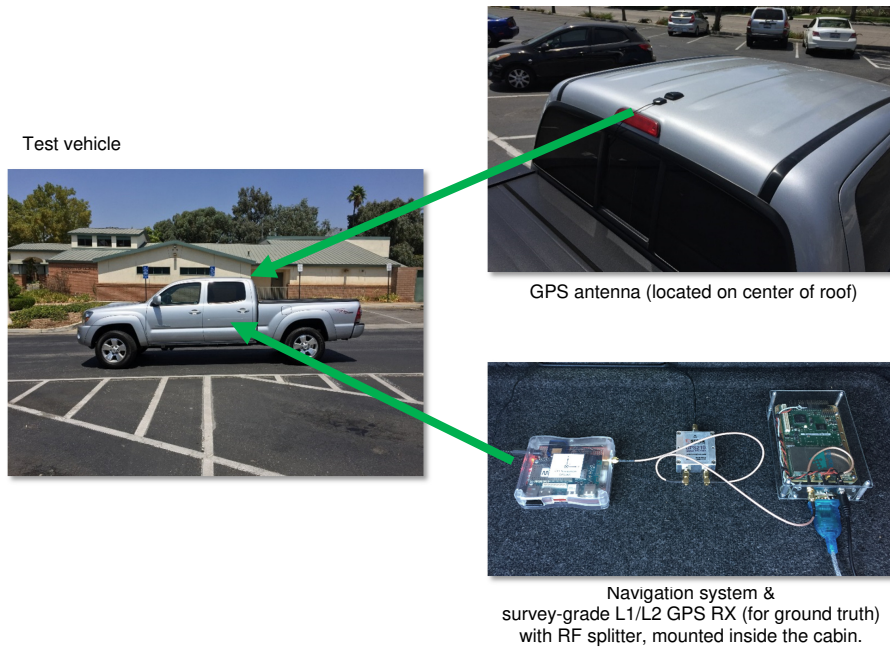


Figure 8.2: Test set-up. Modern vehicle with GPS antenna located on the center of the roof, and navigation system located inside the cabin.

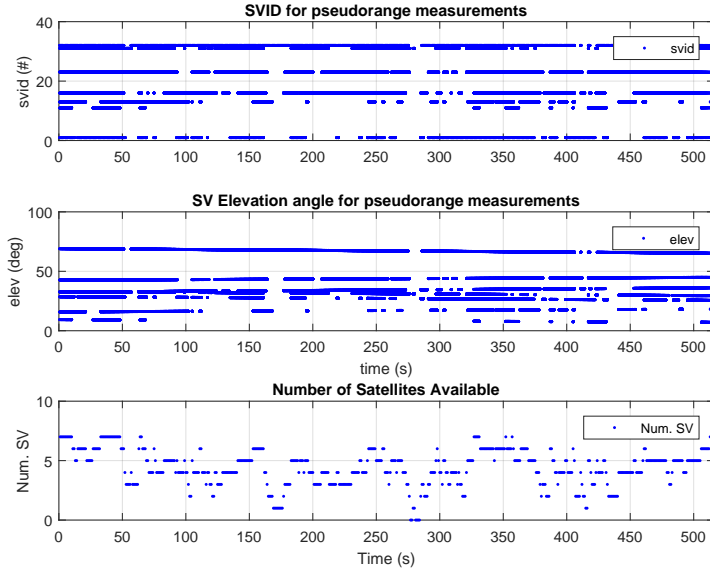


Figure 8.3: Satellite ID, elevation angles, and number of satellites available (after double differencing), versus trajectory time.

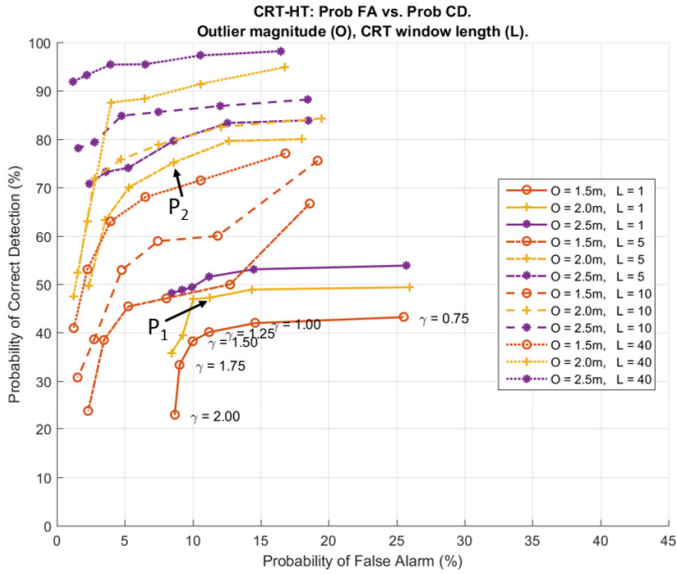


Figure 8.4: Receiver Operating Characteristic curves for each CRT-HT algorithm, outlier magnitude and γ . Values for γ correspond to curve ($O = 1.5m, L = 1$), however the same values apply to the corresponding tick marks on the other curves. Outlier magnitudes $> 2.5m$ have $P_{CD} = 100\%$. Increasing window length L improves P_{CD} regardless of outlier magnitude. Tick-mark style (e.g. circle, star, etc.) and line color correspond to outlier magnitude. Line style (e.g. solid, dashed, etc.) correspond to CRT window length.

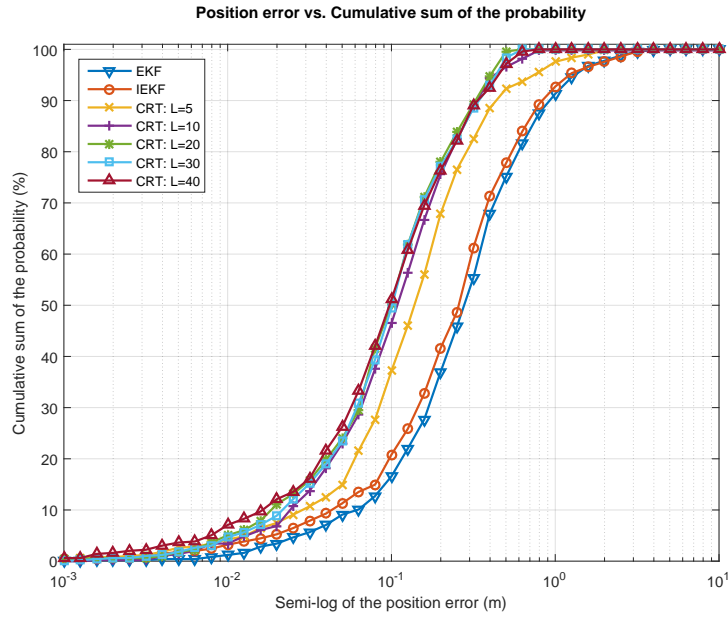


Figure 8.5: Position error cumulative distributions for each HT algorithm. Based on synthetic data results, the value $\gamma = 1.25$ was selected for all curves to guarantee minimum $P_{CD} > 50\%$.

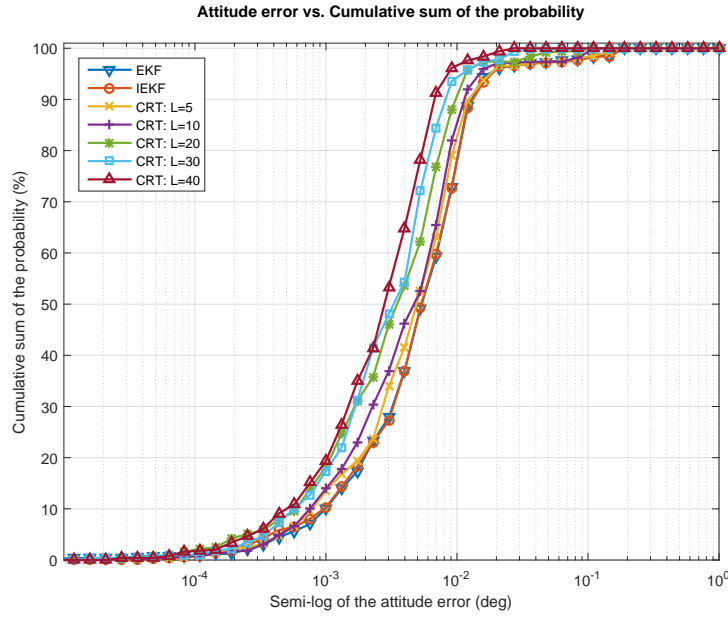


Figure 8.6: Attitude error cumulative distributions for each HT algorithm. Based on synthetic data results, the value $\gamma = 1.25$ was selected for all curves to guarantee minimum $P_{CD} > 50\%$.

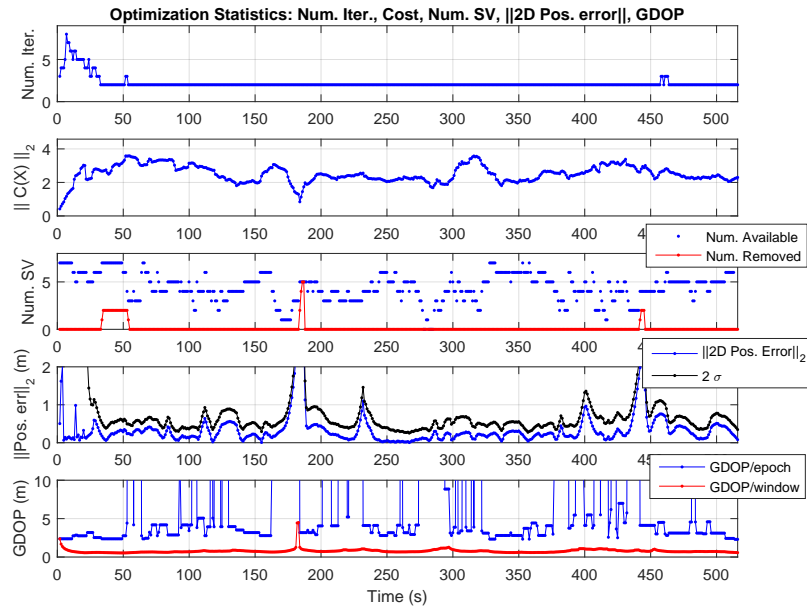


Figure 8.7: Optimization Statistics for experimental data trajectory using CRT-HT with $L = 20$ and $\gamma = 1.00$, including: total number of iterations, final $\|\mathcal{C}(\hat{\mathbf{X}})\|_2$, number of available and removed SVs, $\|2D$ Pos. Error $\|_2$ and estimated position standard deviation, and both per-epoch GDOP and CRT-window GDOP (i.e. computed using all SVs in the CRT window).

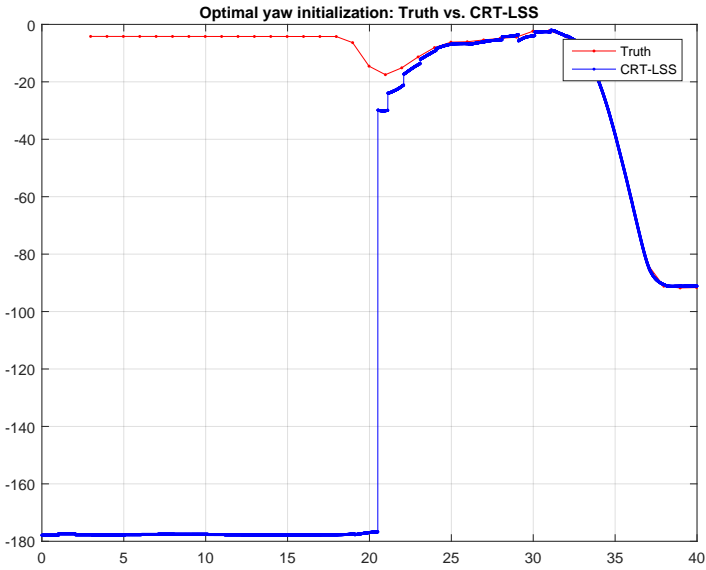


Figure 8.8: CRT optimal yaw estimation.

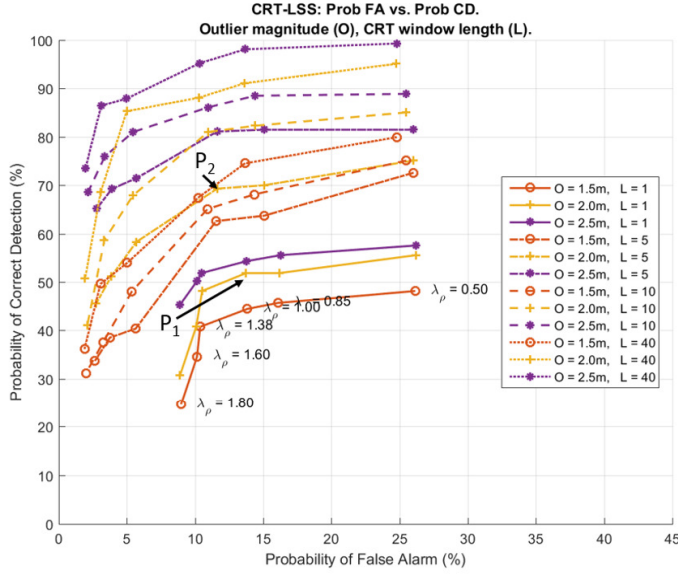


Figure 8.9: Receiver Operating Characteristic curves for each CRT-LSS algorithm, outlier magnitude, and λ_ρ . Values for λ_ρ correspond to curve ($O = 1.5m$, $L = 1$), however the same values apply to the corresponding tick marks on the other curves. Outlier magnitudes $> 2.5m$ have $P_{CD} = 100\%$. Increasing window length L improves P_{CD} regardless of outlier magnitude. Tick-mark style (e.g. circle, star, etc.) and line color correspond to outlier magnitude. Line style (e.g. solid, dashed, etc.) correspond to CRT window length.

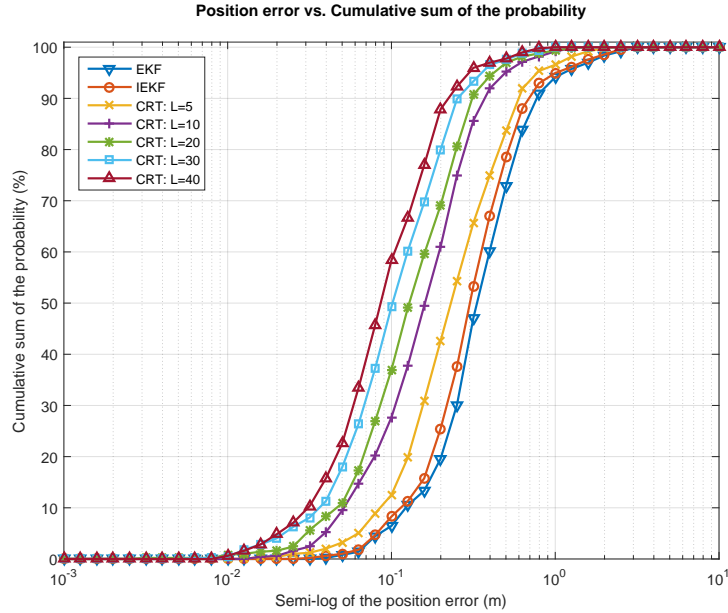


Figure 8.10: Position error cumulative distributions for each LSS algorithm. Based on synthetic data results, the value $\lambda_\rho = 1.00$ was selected for all curves to guarantee minimum $P_{CD} > 50\%$.

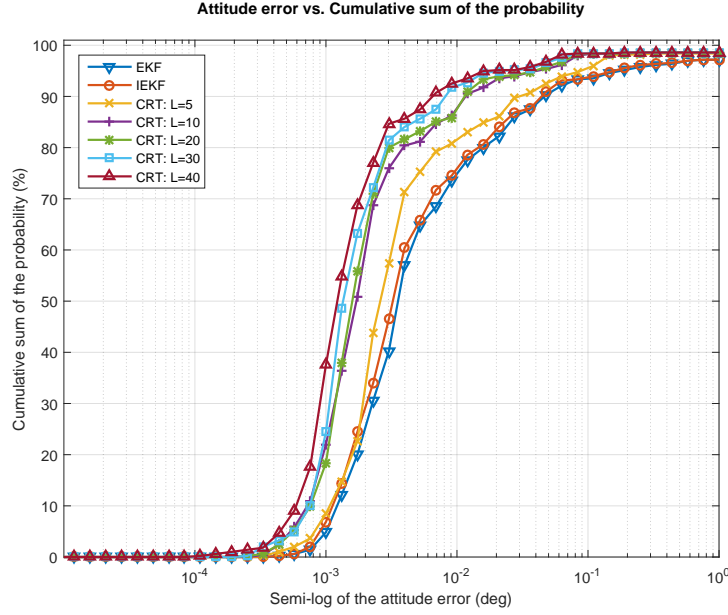


Figure 8.11: Attitude error cumulative distributions for each LSS algorithm. Based on synthetic data results, the value $\lambda_\rho = 1.00$ was selected for all curves to guarantee minimum $P_{CD} > 50\%$.

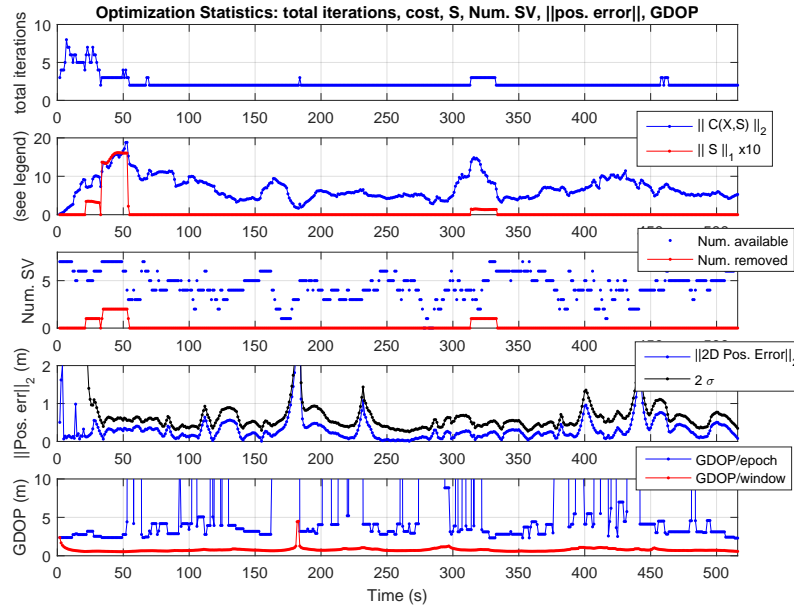


Figure 8.12: Optimization Statistics for experimental data trajectory using CRT-LSS with $L = 20$ and $\gamma = 1.00$, including: total number of iterations, final $\|\mathcal{C}(\mathbf{X}, \mathbf{S})\|_2$ and final $\|\hat{\mathbf{S}}\|_1$, number of available and number of thresholded SVs, $\|2D$ Pos. Error $\|_2$ and estimated position standard deviation, and both per-epoch GDOP and CRT-window GDOP (i.e. computed using all SVs in the CRT window).

Chapter 9

Conclusion and Future Work

This dissertation presented two methods to enhance the level of redundancy in a GNSS and IMU based navigation system to facilitate the accommodation of outlier measurements. Over a multiple epoch sliding window of data, the CRT algorithm performs MAP estimation within a nonlinear optimization framework, while maintaining a real-time estimate as necessary for control and planning purposes. Increasing the duration L of the sliding window enhances redundancy at the expense of increased computation. Enhancing redundancy improves the reliability of achieving any given accuracy specification, by better outlier removal. The MAP framework, through real-time nonlinear optimization, achieves optimal state estimation without linearization assumptions. The enhanced performance of this method is demonstrated through direct comparisons of both the accuracy and outlier detection abilities of various algorithms using experimental data from a challenging environment. Moreover, while the CRT-HT and CRT-LSS have similar outlier accommodation performance, the CRT-HT is a compromise of theory and practicality, whereas the CRT-LSS is a direct numerical implementation of the theory.

9.1 Contributions

The major contribution of this dissertation is the proposition of a novel and efficient outlier accommodation approach for a sliding window filter. This dissertation also provided the following contributions to the GNSS-INS field, and applicable to any vehicle platform and sensor suite:

- Instead of the traditional RAIM or eRAIM outlier accommodation framework which only considers one epoch of aiding measurements, a Bayesian smoothing framework is implemented with multiple epochs over a time window. With a window of IMU and GPS measurements, both accuracy and reliability are improved.
- Utilizing a nonlinear optimization approach, a novel and robust outlier accommodation framework is applied using l_1 -regularization. This outlier accommodation method is optimal, can be applied to multiple sensors, e.g. LiDAR, Radar, Rotary encoder, pressure sensors, etc..
- The CRT framework, through window length, is scalable for position and attitude accuracy requirements, at the expense of computational load. This has the advantage that additional accuracy can be gained using inexpensive modern processors instead of more expensive sensors.

9.2 Publication List

- [1] P. F. Roysdon, and J. A. Farrell, “Robust GPS-INS Outlier Accommodation using a Sliding Window Filter: A Comparative Study,” IEEE Transactions on Control Systems Technology (to be submitted).
- [2] P. F. Roysdon, and J. A. Farrell, “Robust GPS-INS Outlier Accommodation: A Soft-thresholded Optimal Estimator,” 20th World Congress of the International Federation of Automatic Control (IFAC). Toulouse, France, 2017.

- [3] J. A. Farrell, and P. F. Roysdon, “Advanced Vehicle State Estimation: A Tutorial and Comparative Study,” 20th World Congress of the International Federation of Automatic Control (IFAC). Toulouse, France, 2017.
- [4] P. F. Roysdon, and J. Farrell, “GPS-INS Outlier Detection & Elimination using a Sliding Window Filter”, American Control Conference. Seattle, WA, 2017.
- [5] J. J. Morales, P. F. Roysdon, and Z. M. Kassas, “Signals of Opportunity Aided Inertial Navigation,” Institute of Navigation (ION) GNSS+ Conference. Portland, OR, 2016.
- [6] P. F. Roysdon, J. A. Farrell, and D. Kelley, “Enhanced State Estimation for Wheeled Vehicles,” Institute of Navigation (ION) GNSS+ Conference. Tampa, FL, 2015.
- [7] P. F. Roysdon, and J. A. Farrell, “Technical Note: CRT with Hypothesis Testing,” UC Riverside, 2017.
- [8] P. F. Roysdon, and J. A. Farrell, “Technical Note: CRT with Least Soft-thresholded Squares,” UC Riverside, 2017.

9.3 Future Work

The following two items may be interesting for further research:

- Adaptation of the window length L can provide a trade-off of risk and performance. Increasing window length provides additional redundancy in the optimization for measurements that might contain outliers. If outliers do not exist within the window, the length could be reduced to improve computational performance.
- Multipath error modeling can improve the accuracy of the state estimate in a multi-path prone environment by considering the correlation between GPS measurements.

Bibliography

- [1] C. C. Aggarwal. *Outlier Analysis*. Springer, 2013.
- [2] T.W. Anderson and D.A. Darling. A Test of Goodness-of-Fit. *Journal of the American Statistical Association*, 49(765-769), 1954.
- [3] J.E. Angus. RAIM with Multiple Faults. *Journal of The Institute of Navigation*, 53(4), 2006.
- [4] Anon. Global Positioning System Standard Positioning Service Performance Standard. Technical report, U.S. Department of Defense, 2008.
- [5] Anon. Seiko-Epson M-G320PDxx Inertial Measurement Unit (IMU) Data Sheet. Technical report, Seiko-Epson, 2014.
- [6] Anon. 2015 Honda Civic, 2017. Available at: <https://www.honda.com>, URL Date: 2017-05-26.
- [7] Anon. GPS Satellite, 2017. Available at: <https://www.turbosquid.com/3d-models/gps-satellite-3d-model/664711>, URL Date: 2017-05-26.
- [8] Anon. Hero AG-542 Base Station, 2017. Available at: <https://agriculture.trimble.com/precision-ag/products/base-stations/>, URL Date: 2017-05-26.
- [9] Anon. Urban Canyon, 2017. Available at: <https://geoawesomeness.com/wp-content/uploads/2014/01/urbancanyon.jpg>, URL Date: 2017-05-26.
- [10] Anon. Global Positioning System Interface Specification. Report IS-GPS-200-H, U.S. Air Force Global Positioning Systems Directorate Systems Engineering and Integration, 21 March 2014.
- [11] Anon. Global Positioning Wide Area Augmentation System (WAAS) Performance Standard. Report, Federal Aviation Administration, 31 October 2008.
- [12] W. Baarda. Statistical Concepts in Geodesy. *Netherlands Geod. Comm.*, 2(4), 1967.
- [13] W. Baarda. A Testing Procedure for Use in Geodetic Networks. *Netherlands Geod. Comm.*, 2(5), 1968.
- [14] R. V. Beard. *Failure Accommodation in Linear Systems Through Self-Reorganization*. PhD thesis, Massachusetts Inst. of Technology, Cambridge, MA, 1971.

- [15] U. I. Bhatti and W. Y. Ochieng. Detecting Multiple failures in GPS/INS integrated system: A Novel architecture for Integrity Monitoring. *Journal of Global Positioning Systems*, 8(1):26–42, 2006.
- [16] R. G. Brown. A Baseline RAIM Scheme and a Note on the Equivalence of Three RAIM Methods. *Proceedings of the 1992 National Technical Meeting of The Institute of Navigation, San Diego, CA*, pages 127–137, January 27 - 29, 1992.
- [17] R. G. Brown. Solution of the Two-Failure GPS RAIM Problem Under Worst Case Bias Conditions: Parity Space Approach. *Navigation, Journal of The Institute of Navigation*, 44(4), Winter 1997-98.
- [18] Robert Grover Brown and Patrick Y.C. Hwang. *Introduction to Random Signals and Applied Kalman Filtering with Matlab Exercises, 4th Edition*. Wiley, 2012.
- [19] X. W. Chang and T. Zhou. MLAMBDA: a modified LAMBDA method for integer least-squares estimation. *Journal of Geodesy*, 2005.
- [20] X. W. Chang and T. Zhou. MILES: MATLAB package for solving Mixed Integer LEast Squares problems. *Journal of Geodesy*, 2007.
- [21] J. Chen. *Robust residual generation for model-based fault diagnosis of dynamic systems*. PhD thesis, University of York., 1995.
- [22] F. Dellaert and M. Kaess. Square Root SAM: Simultaneous Localization and Mapping via Square Root Information Smoothing. *Int. J. Rob. Res.*, 25(12):1181–1203, 2006.
- [23] J. Diesel and J. King. Integration of Navigation Systems for Fault Detection, Exclusion, and Integrity Determination - Without WAAS. *Proceedings of the 1995 National Technical Meeting of The Institute of Navigation, Anaheim, CA*, pages 683–692, 1995.
- [24] R. Eustice, H. Singh, and J. Leonard. Exactly Sparse Delayed-State Filters for View-Based SLAM. *IEEE Trans. Robotics*, 22(6):1552–3098, 2006.
- [25] J. A. Farrell. *Aided Navigation: GPS with High Rate Sensors*. McGraw Hill, 2008.
- [26] J. A. Farrell and P. F Roysdon. Advanced Vehicle State Estimation: A Tutorial and Comparative Study. *22th IFAC World Congress*, 2017.
- [27] R. A. Fisher. Statistical Methods for Research Workers. *Edinburgh, UK: Oliver and Boyd*, page 43, 1925.
- [28] W. Förstner. Reliability and Discernibility of Extended Gauss-Markov Models. *DGK, A. Reihe, ed., Heft 98, Munich, Germany, (translated from German into English)*, 1998.
- [29] P. M. Frank. Fault diagnosis in dynamic systems using analytical and knowledge-based redundancy a survey and some new results. *Automatica*, 26(3):459474, 1990.
- [30] P. M. Frank. On-line fault detection in uncertain nonlinear systems using diagnostic observers: A survey. *International Journal Systems Science*, 25(12):21292154, 1994.

- [31] P. M. Frank and X. Ding. Survey of robust residual generating and evaluation methods in observer-based fault detection systems. *Journal of Process Control*, 7(6):403424, 1997.
- [32] E. A. Garcia and P. M. Frank. Deterministic nonlinear observer-based approaches to fault diagnosis: A survey. *Control Engineering Practice*, 5(5):663670, 1997.
- [33] P. Gary and C. E. Fly. NDGPS assessment final report. Technical report, U.S. Department of Transportation, 2008.
- [34] P. Gary and C. E. Fly. RTCM Standard 10410.1, Networked Transport of RTCM via Internet Protocol (Ntrip), Version 2.0. Technical report, Radio Technical Commission for Maritime Services, 2011.
- [35] A. Gelb. *Applied Optimal Estimation*. The MIT Press, 2001.
- [36] J. Gertler. Analytical Redundancy Methods in Fault Detection and Isolation. In *Preprints of IFAC/IMACS Symposium on Fault Detection, Supervision and Safety for Technical Processes SAFEPROCESS91*, pages 9–21, 1991.
- [37] J. Gertler. Fault detection and isolation using parity relations. *Control Engineering Practice*, 5(5):653661, 1997.
- [38] J. Gertler and D. Singer. A new structural framework for parity equation-based failure detection and isolation. *Automatica*, 26(2):381–388, 1990.
- [39] J. Gertler and M. Staroswiecki. Structured fault diagnosis in mildly nonlinear systems: parity space and input-output formulations. In *Preprints of the 15th IFAC World Congress*, 2002.
- [40] J. R. Gilbert, C. Moler, and R. Schreiber. Sparse matrices in Matlab: Design and Implementation. *The Mathworks Incorporated*, 1991.
- [41] G. H. Golub and C. F. van Loan. *Matrix Computations*. The Johns Hopkins University Press, third edition, 1996.
- [42] Gene H. Golub and Charles F. Van Loan. *Matrix Computations (3rd ed.)*. Johns Hopkins, 1996.
- [43] P. D. Groves. *Principles of GNSS, Inertial, and Multisensor Integrated Navigation Systems*. Artech House, 2013.
- [44] W. Gurtner. “RINEX: the receiver independent exchange format, Version 2.10”, Dec 2007.
- [45] F.R. Hampel, E.M. Ronchetti, P.J. Rousseeuw, and W.A. Stahel. *Robust Statistics: The approach Based on Influence Functions*. New York: John Wiley and Sons Inc., 1986.
- [46] E. L. Haseltine and J. B. Rawlings. A critical evaluation of extended kalman filtering and moving horizon estimation. March 12, 2003.

- [47] D. Heeger. Signal Detection Theory. *Department of Psychology, New York University*, 2007.
- [48] S. Hewitson and J. Wang. Extended Receiver Autonomous Integrity Monitoring (eRAIM) for GNSS/INS Integration. *Journal of Surveying Engineering*, 136(1):13–22, 2010.
- [49] S. Hewitson and J. Wang. GNSS Receiver Autonomous Integrity Monitoring (eRAIM) for Multiple Outliers. *Journal of Geodesy*, 87(2):13–22, 2012.
- [50] P.J. Huber. *Robust Statistics*. New York: John Wiley and Sons Inc., 1986.
- [51] P. Y. Hwang and R. G. Brown. From RAIM to NIORAIM: A New Integrity Approach to Integrated Multi-GNSS Systems. *Inside GNSS*, May-June, 2008.
- [52] A. H. Jazwinski. Limited Memory Optimal Filtering. 13(5):558–563, 1968.
- [53] Andrew H. Jazwinski. *Stochastic Processes and Filtering*. Academic Press: Mathematics in Science and Engineering, 1970.
- [54] M. Kaess, H. Johannsson, R. Roberts, V. Ila, J.J. Leonard, and F. Dellaert. iSAM2: Incremental smoothing and mapping using the Bayes tree. *Intl. J. of Robotics Research*, 31(2):216–235, February 2012.
- [55] M. Kaess, A. Ranganathan, and F. Dellaert. iSAM: Incremental Smoothing and Mapping. *IEEE Trans. Robotics*, 24(6):1365–1378, 2008.
- [56] R. E. Kalman. A New Approach to Linear Filtering and Prediction Problems. *Transactions of the ASME Journal of Basic Engineering*, 82(D):35–45, 1960.
- [57] E.D. Kaplan and C.J. Hegarty. *Understanding GPS Principles and Applications*, 2nd Ed. Artch House, 2006.
- [58] Steven M. Kay. *Fundamentals of Statistical Signal Processing, Vol. II - Detection Theory*. Prentice Hall PTR, 1998.
- [59] Steven M. Kay. *Fundamentals of Statistical Signal Processing, Vol. I - Estimation Theory*. Prentice Hall PTR, 2013.
- [60] M. Li, B.H. Kim, and A. I. Mourikis. Real-time motion estimation on a cellphone using inertial sensing and a rolling-shutter camera. In *Proceedings of the IEEE International Conference on Robotics and Automation*, pages 4697–4704, Karlsruhe, Germany, May 2013.
- [61] M. Li, H. Yu, X. Zheng, and A. I. Mourikis. High-fidelity sensor modeling and self-calibration in vision-aided inertial navigation. In *Proceedings of the IEEE International Conference on Robotics and Automation*, pages 409–416, Hong Kong, June 2014.

- [62] Mingyang Li and A. I. Mourikis. Optimization-based estimator design for vision-aided inertial navigation. In *Proceedings of Robotics: Science and Systems*, Sydney, Australia, Jul. 2012.
- [63] Mingyang Li and Anastasios I. Mourikis. Vision-aided inertial navigation for resource-constrained systems. In *Proceedings of the IEEE/RSJ International Conference on Intelligent Robots and Systems*, pages 1057–1063, Vilamoura, Portugal, Oct. 2012.
- [64] Mingyang Li and Anastasios I Mourikis. High-precision, consistent EKF-based visual–inertial odometry. *Int. J. of Rob. Res.*, 32(6):690–711, 2013.
- [65] X. Lou, A. S. Willsky, and G. C. Verghese. Optimally Robust Redundancy Relations for Failure Detection in Uncertain Systems. *Automatica*, 22(3):333–344, 1986.
- [66] Yi Ma, Jana Košecká, Stefano Soatto, and Shankar Sastry. *An Invitation to 3-D Vision From Images to Models*. Springer, New York, 2004.
- [67] J. F. Magni and P. Mouyon. On residual generation by observer and parity space approaches. *IEEE Transactions on Automatic Control*, 39(2):441–447, 1994.
- [68] Peter S. Maybeck. *Stochastic Models, Estimation, and Control*. Academic Press: Mathematics in Science and Engineering, 1979.
- [69] D. Q. Mayne and H. Michalska. Adaptive receding horizon control for constrained nonlinear systems. pages 1286–1291, 1993.
- [70] A. Medvedev. Fault Detection and Isolation by a Continuous Parity Space Method. *Automatica*, 31(7):1039–1034, 1995.
- [71] X. Mei and H. Ling. Robust Visual Tracking using L-1 Minimization. *2009 IEEE 12th International Conference on Computer Vision (ICCV)*, 2009.
- [72] P.A. Miller, J.A. Farrell, Y. Zhao, and V. Djapic. Autonomous Underwater Vehicle Navigation. *IEEE J. of Oceanic Eng.*, 35(3):663 – 678, 2010.
- [73] P. E. Moraal and J. W. Grizzle. Observer design for nonlinear systems with discrete-time measurements. *IEEE TAC*, 40:1995, 395404.
- [74] A.I. Mourikis and S.I. Roumeliotis. A Multi-State Constraint Kalman Filter for Vision-aided Inertial Navigation. In *IEEE ICRA*, pages 3565–3572, 2007.
- [75] K. R. Muske, J. B. Rawlings, and J. B. Lee. Receding horizon recursive state estimation. pages 900–904, 1993.
- [76] J. Neyman and E. S. Pearson. The testing of statistical hypotheses in relation to probabilities a priori. *Mathematical Proceedings of the Cambridge Philosophical Society*, 29:492–510, 1933.
- [77] R. J. Patton. Fault detection and diagnosis in aerospace systems using analytical redundancy. *Computing and Control Engineering Journal*, 2(3):127–136, 1991.

- [78] R. J. Patton and J. Chen. A review of parity space approaches to fault diagnosis for aerospace systems. *Journal of Guidance, Control and Dynamics*, 17(2):278–285, 1994.
- [79] P.J. Rousseeuw and A.M. Leroy. *Robust regression and outlier detection*. Wiley Series in Probability and Mathematical Statistics: Applied Probability and Statistics, New York: John Wiley and Sons Inc., 1987.
- [80] P. F. Roysdon and J. A. Farrell. GPS-INS Outlier Detection and Elimination using a Sliding Window Filter. *American Control Conference, In Presc.*, 2017.
- [81] P. F. Roysdon and J. A. Farrell. Robust GPS-INS Outlier Accomodation using a Sliding Window Filter. *22th IFAC World Congress*, 2017.
- [82] P. F. Roysdon and J. A. Farrell. “Technical Note: CRT with Hypothesis Testing and Least Soft-thresholdded Squares”, 2017. Available at: www.escholarship.org/uc/item/4b0289qj, URL Date: 2017-03-31.
- [83] RTCM Special Committee No. 104. RTCM Standard 10403.1, Differential GNSS Services, Version 3. Technical report, Radio Technical Commission for Maritime Services, 2011.
- [84] S. S. Shapiro and M. B. Wilk. An analysis of variance test for normality (complete samples). *Biometrika*, 52(3):591–611, 1965.
- [85] M.D. Shuster. A survey of attitude representations. *Journal of the Astronautical Sciences*, 41(4):439–517, 1993.
- [86] M.D. Shuster. The nature of the quaternion. *Journal of the Astronautical Sciences*, 56(3):359, 2010.
- [87] N. Smirnov. Table for estimating the goodness of fit of empirical distributions. *Annals of Mathematical Statistics*, 19:279–281, 1948.
- [88] R. A. Snay and M. ASCE Tomás Soler. Continuously operating reference station (CORS): History, applications, and future enhancements. *Journal of Surveying Engineering*, 134(4), 2008.
- [89] M. Staroswiecki and G. Comtet-Varga. Analytical redundancy relations for fault detection and isolation in algebraic dynamic systems. *Automatica*, 37(5):687–699, 2001.
- [90] M. A. Stephens. EDF Statistics for Goodness of Fit and Some Comparisons. *Journal of the American Statistical Association (American Statistical Association)*, 69(374):730–737, 1974.
- [91] M. A. Sturza. Navigation System Integrity Monitoring Using Redundant Measurements. *Navigation, Journal of The Institute of Navigation*, 35(4), Winter 1988-89.
- [92] P. J. G. Teunissen. The least-squares ambiguity decorrelation adjustment: a method for fast GPS integer ambiguity estimation. *Journal of Geodesy*, 1994.

- [93] P. J. G. Teunissen. Quality Control in Integrated Navigation Systems. *IEEE Aerospace and Electronic Systems Magazine*, 5(7):35–41, August 1990.
- [94] Bill Triggs, Philip McLauchlan, Richard Hartley, and Andrew Fitzgibbon. *Bundle Adjustment - A Modern Synthesis Vision Algorithms: Theory and Practice*, volume 1883 of *Lecture Notes in Computer Science*. Springer Berlin / Heidelberg, 2000.
- [95] H. Urkowitz. Energy detection of unknown deterministic signals. *Proceedings of the IEEE*, 55(4):523–531, 1967.
- [96] A. Vu and J. A. Farrell. Feature mapping and state estimation for highly automated vehicles. *Journal of Control and Decision*, 2(1):1–25, 2015.
- [97] D. Wang, H. Lu, and M. Yang. Robust Visual Tracking via Least Soft-threshold Squares. *IEEE Transactions on Circuits and Systems for Video Technology*, 2015.
- [98] M. Wei and K. P. Schwarz. A strapdown inertial algorithm using earth-fixed cartesian frame. *Navigation: JION*, 371(2):153–167, 1990.
- [99] S. Weisberg. *Applied Linear Regression*. 2nd ed, New York, Wiley, 1985.
- [100] S. S. Wilks. The large-sample distribution of the likelihood ratio for testing composite hypotheses. *Annals of Mathematical Statistics*, 9(1):60–62, 1938.
- [101] A. S. Willsky. A Survey of Design Methods for Failure Detection in Dynamic Systems. *Automatica*, 12(6):601–611, 1976.
- [102] A. S. Willsky and E. Y. Chow. Issues in the development of a general design algorithm for reliable failure detection. pages 1006–1012, 1980.
- [103] A. S. Willsky and E. Y. Chow. Analytical Redundancy and the Design of Robust Failure Detection Systems. *IEEE Transactions of Automatic Control*, AC-29(7):603–614, 1984.
- [104] J. Wright, A. Yang, A. Ganesh, S. Sastry, and Y. Ma. Robust Face Recognition via Sparse Representation. *IEEE Transactions on Pattern Analysis and Machine Intelligence*, 31(2), 2009.
- [105] S. Zhao, Y. Chen, H. Zhang, and J. A. Farrell. Differential GPS Aided Inertial Navigation: A Contemplative Realtime Approach. *19th IFAC World Congress*, pages 8959–8964, 2014.
- [106] G. Zimmer. State observation by on-line minimization. 60(4):595–606, 1994.

Appendix A

Proofs & Derivations

A.1 Attitude Update Derivation

The goal of this section is to derive eqn. (3.10) from eqn. (3.9). The starting point of this derivation is eqn. (3.9) and the related definitions:

$$\dot{\mathbf{R}}_b^e = \mathbf{R}_b^e \boldsymbol{\Omega}_{eb}^b$$

$$\boldsymbol{\Omega}_{eb}^b \triangleq [\boldsymbol{\omega}_{eb}^b \times] = \boldsymbol{\Omega}_{ib}^b - \boldsymbol{\Omega}_{ie}^b$$

$$\boldsymbol{\alpha}_{ib}^b \triangleq \boldsymbol{\omega}_{ib}^b \delta t.$$

The definition of the derivative is

$$\dot{\mathbf{R}}_b^e = \lim_{\delta t \rightarrow 0} \frac{\mathbf{R}_b^e(t + \delta t) - \mathbf{R}_b^e(t)}{\delta t}. \quad (\text{A.1})$$

Assuming that the time increment δt is sufficiently small:

$$\begin{aligned}
\mathbf{R}_b^e(t + \delta t) &= \dot{\mathbf{R}}_b^e(t)\delta t + \mathbf{R}_b^e(t) \\
&= \mathbf{R}_b^e(t)\boldsymbol{\Omega}_{eb}^b\delta t + \mathbf{R}_b^e(t) \\
&= \mathbf{R}_b^e(t)(\boldsymbol{\Omega}_{ib}^b - \boldsymbol{\Omega}_{ie}^b)\delta t + \mathbf{R}_b^e(t) \\
&= \mathbf{R}_b^e(t)\boldsymbol{\Omega}_{ib}^b\delta t - \mathbf{R}_b^e(t)\boldsymbol{\Omega}_{ie}^b\delta t + \mathbf{R}_b^e(t) \\
&= \mathbf{R}_b^e(t)[\boldsymbol{\alpha}_{ib}^b \times] - \mathbf{R}_b^e(t)\mathbf{R}_e^b(t)\boldsymbol{\Omega}_{ie}^b\mathbf{R}_b^e(t)\delta t + \mathbf{R}_b^e(t) \\
&= \mathbf{R}_b^e(t)\mathbf{R}_{b(t)}^{b(t+\delta t)} - \boldsymbol{\Omega}_{ie}^b\mathbf{R}_b^e(t)\delta t + \mathbf{R}_b^e(t)
\end{aligned} \tag{A.2}$$

Note that $\mathbf{R}_{b(t)}^{b(t+\delta t)}$ is defined in eqn. (3.11) as the exponential of $[\boldsymbol{\alpha}_{ib}^b \times]$. The last step in deriving eqn. (A.2) is not obvious, see Section 2.71 in [25]. The only derivation in the assumption is that the IMU angular-rate measurement is constant over the integration interval.

A.2 Quaternion Update Approximation

Let $f(\boldsymbol{\rho}) = \sqrt{1 - \|\frac{1}{2}\boldsymbol{\rho}\|_2^2} \in \mathbb{R}^1$, and $\delta\boldsymbol{\rho} = \boldsymbol{\rho} - \mathbf{0} \in \mathbb{R}^{3 \times 1}$. By first-order Taylor series expansion of $f(\boldsymbol{\rho})$, assuming small-angle $\boldsymbol{\rho}$, the quantity $\mathbf{q}_{\hat{n}}^n$ is

$$\begin{aligned}
\mathbf{q}_{\hat{n}}^n &= \begin{bmatrix} f(\boldsymbol{\rho}) \\ \frac{1}{2}\boldsymbol{\rho} \end{bmatrix} \\
&= \begin{bmatrix} f(\mathbf{0}) + \left. \frac{\partial f(\boldsymbol{\rho})}{\partial \boldsymbol{\rho}} \right|_{\boldsymbol{\rho}=\mathbf{0}} \delta \boldsymbol{\rho} + \delta \boldsymbol{\rho}^\top \left. \frac{\partial^2 f(\boldsymbol{\rho})}{2 \partial \boldsymbol{\rho}^2} \right|_{\boldsymbol{\rho}=\mathbf{0}} \delta \boldsymbol{\rho} + \dots \\ \frac{1}{2}\boldsymbol{\rho} \end{bmatrix} \\
&= \begin{bmatrix} 1 + \left[\frac{-\boldsymbol{\rho}}{2\sqrt{1-\|\frac{1}{2}\boldsymbol{\rho}\|_2^2}} \right] \Big|_{\boldsymbol{\rho}=\mathbf{0}} \delta \boldsymbol{\rho} \\ \frac{1}{2}\boldsymbol{\rho} \end{bmatrix} \\
&= \begin{bmatrix} 1 \\ \frac{1}{2}\boldsymbol{\rho} \end{bmatrix},
\end{aligned}$$

where the derivation of the gradient and Hessian is provided in Section A.3. Note:

- $f(\mathbf{0}) = \sqrt{1 - \left\| \frac{1}{2}\mathbf{0} \right\|_2^2} = 1$.
- For $\boldsymbol{\rho} \ll 1$, then $\left. \delta \boldsymbol{\rho}^\top \frac{\partial^2 f(\boldsymbol{\rho})}{2 \partial \boldsymbol{\rho}^2} \right|_{\boldsymbol{\rho}=\mathbf{0}} \delta \boldsymbol{\rho} \approx 0$.
- $\hat{\mathbf{q}}_v$ is linear already.

A.3 Quaternion Gradient & Hessian Derivation

Let $\mathbf{h}(\mathbf{x}) = (\mathbf{x}^\top \mathbf{x})^{1/2}$ where $\mathbf{x} \in \mathbb{R}^{3 \times 1}$. The Jacobian of $\mathbf{h}(\mathbf{x})$ is

$$\frac{\partial \mathbf{h}(\mathbf{x})}{\partial \mathbf{x}} = \frac{\mathbf{x}^\top}{(\mathbf{x}^\top \mathbf{x})^{1/2}}.$$

The Hessian of $\mathbf{h}(\mathbf{x})$ is

$$\begin{aligned}
\frac{\partial^2 \mathbf{h}(\mathbf{x})}{\partial \mathbf{x}^2} &= \frac{\mathbf{I}}{(\mathbf{x}^\top \mathbf{x})^{1/2}} - \left(\frac{1}{2} \right) (2) \frac{\mathbf{x} \mathbf{x}^\top}{(\mathbf{x}^\top \mathbf{x})^{3/2}} \\
&= \frac{\mathbf{x}^\top \mathbf{x} \mathbf{I} - \mathbf{x} \mathbf{x}^\top}{(\mathbf{x}^\top \mathbf{x})^{3/2}}.
\end{aligned}$$

A.4 Proof of Idempotent P

For the matrix \mathbf{P} to be idempotent, it must be the case that $\mathbf{P} = \mathbf{P}^\top \mathbf{P} = \mathbf{P}\mathbf{P}$, where $\mathbf{P} \triangleq \mathbf{H}(\mathbf{H}^\top \mathbf{H})^{-1} \mathbf{H}^\top$, and $\mathbf{H} \in \mathbb{R}^{m \times n}$, with $m > n$. Thus we can show:

$$\begin{aligned}\mathbf{P}^\top &= (\mathbf{H}(\mathbf{H}^\top \mathbf{H})^{-1} \mathbf{H}^\top)^\top \\ &= \mathbf{H}(\mathbf{H}^\top \mathbf{H})^{-1} \mathbf{H}^\top \\ &= \mathbf{P} \\ \mathbf{P}\mathbf{P} &= \mathbf{H}(\mathbf{H}^\top \mathbf{H})^{-1} \mathbf{H}^\top \mathbf{H}(\mathbf{H}^\top \mathbf{H})^{-1} \mathbf{H}^\top \\ &= \mathbf{H}(\mathbf{H}^\top \mathbf{H})^{-1} \mathbf{H}^\top \\ &= \mathbf{P} \\ \therefore \mathbf{P}^\top \mathbf{P} &= \mathbf{P}\mathbf{P} = \mathbf{P}.\end{aligned}$$

■

A.5 Proof of Rank P

We can prove that $\text{rank}(\mathbf{P}) = n$. First recall that $\mathbf{H} \in \mathbb{R}^{m \times n}$, with $m > n$ and full column rank, i.e. $\text{rank}(\mathbf{H}) = n$. Let the SVD of \mathbf{H} be defined as

$$\begin{aligned}\mathbf{H} &= \mathbf{U}\Sigma\mathbf{V}^\top \\ &= [\mathbf{U}_1, \mathbf{U}_2] \begin{bmatrix} \begin{pmatrix} \Sigma_1 \end{pmatrix} \\ \begin{pmatrix} \Sigma_0 \end{pmatrix} \end{bmatrix} \mathbf{V}^\top\end{aligned}$$

where $\Sigma \in \mathbb{R}^{m \times m}$, $\Sigma_1 = \text{diag}(\sigma_1, \dots, \sigma_n) \in \mathbb{R}^{n \times n}$, and $\Sigma_0 = \mathbf{0} \in \mathbb{R}^{(m-n) \times n}$, where σ_i for $i = 1, \dots, n$ are the singular values of \mathbf{H} . Both $\mathbf{U} \in \mathbb{R}^{m \times m}$ and $\mathbf{V} \in \mathbb{R}^{n \times n}$ are unitary matrices, therefore $\mathbf{U}\mathbf{U}^\top = \mathbf{U}^\top \mathbf{U} = \mathbf{I} \in \mathbb{R}^{m \times m}$ and $\mathbf{V}\mathbf{V}^\top = \mathbf{V}^\top \mathbf{V} = \mathbf{I} \in \mathbb{R}^{n \times n}$. The columns

of $\mathbf{U}_1 \in \mathbb{R}^{m \times n}$ form an orthonormal basis for the range-space of \mathbf{H} , and the columns of $\mathbf{U}_2 \in \mathbb{R}^{m \times (m-n)}$ form the null-space of \mathbf{H}^\top . Similarly the first n columns of \mathbf{V} form an orthonormal basis for the range of \mathbf{H}^\top , and the $m - n$ columns of \mathbf{V} form an orthonormal basis for the null-space of \mathbf{H} . Finally, the eigenvectors \mathbf{V} of the matrix $\mathbf{H}^\top \mathbf{H}$ are the right singular values of \mathbf{H} , and the singular values of \mathbf{H} squared are the corresponding nonzero eigenvalues: $\sigma_i = \sqrt{\lambda_i(\mathbf{H}^\top \mathbf{H})}$. Similarly, the eigenvectors of $\mathbf{H} \mathbf{H}^\top$ are the left singular vectors \mathbf{U} of matrix \mathbf{H} , and the singular values of \mathbf{H} squared are the nonzero eigenvalues of $\mathbf{H} \mathbf{H}^\top$: $\sigma_i = \sqrt{\lambda_i(\mathbf{H} \mathbf{H}^\top)}$.

Define \mathbf{P} in terms of the SVD of \mathbf{H} :

$$\begin{aligned}\mathbf{P} &= \mathbf{H}(\mathbf{H}^\top \mathbf{H})^{-1} \mathbf{H}^\top \\ &= (\mathbf{U} \Sigma \mathbf{V}^\top)(\mathbf{V} \Sigma^\top \mathbf{U}^\top \mathbf{U} \Sigma \mathbf{V}^t)^{-1} (\mathbf{V} \Sigma^\top \mathbf{U}^\top) \\ &= (\mathbf{U} \Sigma \mathbf{V}^\top)(\mathbf{V} \Sigma^\top \Sigma \mathbf{V}^\top)^{-1} (\mathbf{V} \Sigma^\top \mathbf{U}^\top) \\ &= (\mathbf{U} \Sigma \mathbf{V}^\top)(\mathbf{V} \Sigma_1^2 \mathbf{V}^\top)^{-1} (\mathbf{V} \Sigma^\top \mathbf{U}^\top) \quad (\text{A.3})\end{aligned}$$

$$= (\mathbf{U} \Sigma \mathbf{V}^\top)(\mathbf{V})^{-1} (\Sigma_1^2)^{-1} (\mathbf{V}^\top)^{-1} (\mathbf{V} \Sigma^\top \mathbf{U}^\top) \quad (\text{A.4})$$

$$= \mathbf{U} \Sigma \mathbf{V}^\top \mathbf{V} \Sigma_1^{-2} \mathbf{V}^\top \mathbf{V} \Sigma^\top \mathbf{U}^\top \quad (\text{A.5})$$

$$= \mathbf{U} \Sigma_1 \Sigma_1^{-2} \Sigma_1^\top \mathbf{U}^\top \quad (\text{A.6})$$

$$= \mathbf{U} \Sigma_1 \Sigma_1^{-1} \Sigma_1^{-1} \Sigma_1^\top \mathbf{U}^\top \quad (\text{A.7})$$

$$= \mathbf{U} \mathbf{I}_{n \times n} \mathbf{U}^\top$$

$$= [\mathbf{U}_1 \mathbf{U}_2] \begin{bmatrix} \mathbf{I}_{n \times n} & \mathbf{0} \\ \mathbf{0} & \mathbf{0} \end{bmatrix} \begin{bmatrix} \mathbf{U}_1^\top \\ \mathbf{U}_2^\top \end{bmatrix}$$

$$= \mathbf{U}_1 \mathbf{U}_1^\top.$$

The middle product in eqn. (A.3) can be separated because it is an $n \times n$ matrix with rank n , and it is non-singular. In eqns. (A.3)-(A.7), we need only consider Σ_1 as Σ_0 drops out.

The rank of matrix \mathbf{P} is defined as the number of non-zero singular values of \mathbf{P} . Thus, $\text{rank}(\mathbf{P}) = n$. Similarly, because \mathbf{P} is idempotent, $\text{rank}(\mathbf{P}) = \text{tr}(\mathbf{P})$, then $\text{rank}(\mathbf{P}) = n$.

■

A.6 Proof of Idempotent \mathbf{Q}

For the matrix \mathbf{Q} to be idempotent, it must be the case that $\mathbf{Q} = \mathbf{Q}^\top \mathbf{Q} = \mathbf{Q}\mathbf{Q}$, where $\mathbf{Q} \triangleq (\mathbf{I} - \mathbf{P})$, and $\mathbf{P} \in \mathbb{R}^{m \times m}$. Thus we can show:

$$\mathbf{Q}\mathbf{Q} = (\mathbf{I} - \mathbf{P})(\mathbf{I} - \mathbf{P})$$

$$= \mathbf{I} - \mathbf{P}$$

$$= \mathbf{Q}$$

$$\mathbf{Q}^\top \mathbf{Q} = (\mathbf{I} - \mathbf{P})^\top (\mathbf{I} - \mathbf{P})$$

$$= (\mathbf{I} - \mathbf{P}^\top)(\mathbf{I} - \mathbf{P})$$

$$= \mathbf{I} - \mathbf{P} - \mathbf{P}^\top + \mathbf{P}^\top \mathbf{P}, \quad \mathbf{P} = \mathbf{P}^\top \mathbf{P}$$

$$= \mathbf{I} - \mathbf{P} - \mathbf{P}^\top + \mathbf{P}, \quad \mathbf{P}^\top = \mathbf{P}$$

$$= \mathbf{I} - \mathbf{P}$$

$$= \mathbf{Q}$$

$$\therefore \mathbf{Q}^\top \mathbf{Q} = \mathbf{Q}\mathbf{Q} = \mathbf{Q}$$

■

A.7 Proof of Rank Q

We can prove that $\text{rank}(\mathbf{Q}) = m - n$ by the SVD of \mathbf{H} . Apply the result from the proof for the rank of \mathbf{P} , where $\mathbf{P} \in \mathbb{R}^{m \times m}$ and $\mathbf{I} \in \mathbb{R}^{m \times m}$. Using the inner product we can define \mathbf{I} in terms of \mathbf{U}

$$\begin{aligned}\mathbf{I} &= \mathbf{U}\mathbf{U}^\top \\ &= [\mathbf{U}_1 \mathbf{U}_2] \begin{bmatrix} \mathbf{U}_1^\top \\ \mathbf{U}_2^\top \end{bmatrix} \\ &= \mathbf{U}_1 \mathbf{U}_1^\top + \mathbf{U}_2 \mathbf{U}_2^\top.\end{aligned}$$

Alternatively, by the outer product we can define

$$\begin{aligned}\mathbf{I} &= \mathbf{U}^\top \mathbf{U} \\ &= \begin{bmatrix} \mathbf{U}_1^\top \\ \mathbf{U}_2^\top \end{bmatrix} [\mathbf{U}_1 \mathbf{U}_2] \\ &= \begin{bmatrix} \mathbf{U}_1^\top \mathbf{U}_1 & \mathbf{U}_1^\top \mathbf{U}_2 \\ \mathbf{U}_2^\top \mathbf{U}_1 & \mathbf{U}_2^\top \mathbf{U}_2 \end{bmatrix}\end{aligned}$$

where $\mathbf{U}_1^\top \mathbf{U}_1 = \mathbf{I} \in \mathbb{R}^{n \times n}$, $\mathbf{U}_2^\top \mathbf{U}_2 = \mathbf{I} \in \mathbb{R}^{(m-n) \times (m-n)}$. Finally, $\mathbf{U}_2 \mathbf{U}_2^\top = \mathbf{P} \in \mathbb{R}^{m \times m}$ as proved above, and $\mathbf{U}_1 \mathbf{U}_1^\top = \mathbf{Q} \in \mathbb{R}^{m \times m}$ which is proven below.

Now define \mathbf{Q} as

$$\begin{aligned}\mathbf{Q} &= \mathbf{I} - \mathbf{P} \\ &= (\mathbf{U}_1 \mathbf{U}_1^\top + \mathbf{U}_2 \mathbf{U}_2^\top) - \mathbf{U}_1 \mathbf{U}_1^\top \\ &= \mathbf{U}_2 \mathbf{U}_2^\top.\end{aligned}$$

The rank of matrix \mathbf{Q} is defined as the number of non-zero singular values of \mathbf{Q} . Thus, for $\mathbf{Q} \triangleq (\mathbf{I} - \mathbf{P})$, and $\text{rank}(\mathbf{P}) = n$, the number of non-zero singular values of \mathbf{Q} is at most $m - n$, and therefore the $\text{rank}(\mathbf{Q}) = m - n$.

■

A.8 Physical Interpretation of \mathbf{P} & \mathbf{Q}

The physical interpretation for \mathbf{P} and \mathbf{Q} is a mapping of the measurement and the residual, as shown in Fig. A.1. \mathbf{Py} projects \mathbf{y} onto the $\text{range}(\mathbf{P})$ along the direction of \mathbf{y} . The complementary projector is \mathbf{Q} , where \mathbf{Qy} projects \mathbf{y} onto the $\text{range}(\mathbf{Q})$ which is orthogonal to the $\text{range}(\mathbf{P})$.

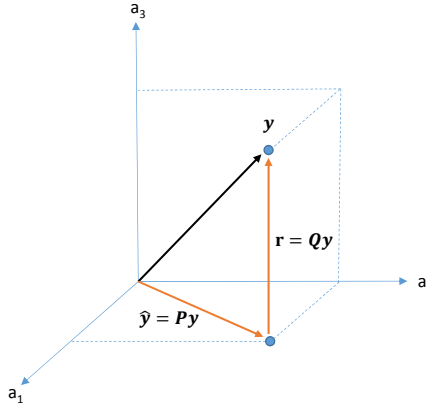


Figure A.1: For a general space in \mathbb{R}^3 , the mapping $\mathbf{Py} = \hat{\mathbf{y}}$ is the estimate for \mathbf{y} , and $\mathbf{Qy} = \mathbf{r}$ is the estimation residual for \mathbf{y} .

From the SVD of \mathbf{H} we have the relations:

1. $\mathbf{V}_1\mathbf{V}_1^\top$ is the orthogonal projector onto $[N(\mathbf{H})]^\perp = R(\mathbf{H}^\top)$.
2. $\mathbf{V}_2\mathbf{V}_2^\top$ is the orthogonal projector onto $N(\mathbf{H})$.

3. $\mathbf{U}_1 \mathbf{U}_1^\top$ is the orthogonal projector onto $R(\mathbf{H})$.
4. $\mathbf{U}_2 \mathbf{U}_2^\top$ is the orthogonal projector onto $[R(\mathbf{H})]^\perp = N(\mathbf{H}^\top)$.

A.9 Soft-Thresholding Operator Proof

This section solves the optimization problem

$$f(r) = \arg \min_s \left\{ \frac{1}{2} \left(r - \frac{s}{\sigma} \right)^2 + \frac{1}{\nu} |s| \right\} = \arg \min_s g_r(s),$$

where $r, s \in \mathbb{R}$, $\sigma > 0$ and $\nu > 0$ are the parameters of the Normal and Laplacian distributions, and

$$g_r(s) \triangleq \frac{1}{2} \left(r - \frac{s}{\sigma} \right)^2 + \frac{1}{\nu} |s|. \quad (\text{A.8})$$

Note first that $g_r(s) \Big|_{s=0} = g_r(0) = \frac{1}{2}r^2$.

Because $g_r(s)$ is not differentiable in s , three cases can be considered ($s < 0$, $s = 0$, and $s > 0$), with the final answer being the value of s over the three cases that gives the lowest cost. For $s \neq 0$:

$$\frac{\partial}{\partial s} g_r(s) = -\frac{r}{\sigma} + \frac{s}{\sigma^2} + \frac{1}{\nu} \operatorname{sgn}(s).$$

For $s > 0$, $\frac{\partial}{\partial s} g_r(s) = 0$ yields the critical value $s_+^* = \sigma(r - \mu)$, where $\mu \triangleq \frac{\sigma}{\nu}$.

Because, in this case $s_+^* > 0$, it must be that $r > \mu$. The cost at s_+^* is:

$$g_r(s) \Big|_{s=s_+^*} = g_r(\sigma(r - \mu)) = \mu r - \frac{1}{2}\mu^2.$$

Note that:

$$\frac{1}{2}(r - \mu)^2 \geq 0 \quad \forall r, \mu;$$

therefore,

$$\frac{1}{2}r^2 \geq r\mu - \frac{1}{2}\mu^2 \quad \forall r, \mu.$$

This ensures that in this case (i.e., $s > 0$), for any value of r , it is true that $g_r(s_+^*) \leq g_r(0)$.

For $s < 0$, $\frac{\partial}{\partial s}g_r(s) = 0$ yields the critical value $s_-^* = \sigma(r + \mu)$. Because, in this case $s_-^* < 0$, it must be that $r < -\mu$. The cost at s_-^* is:

$$g_r(s)\Big|_{s=s_-^*} = g_r(\sigma(r + \mu)) = -\mu r - \frac{1}{2}\mu^2.$$

Note that:

$$\frac{1}{2}(r + \mu)^2 \geq 0 \quad \forall r, \mu;$$

therefore,

$$\frac{1}{2}r^2 \geq -r\mu - \frac{1}{2}\mu^2 \quad \forall r, \mu.$$

This ensures that in this case (i.e., $s < 0$), for any value of r , it is true that $g_r(s_+^*) \leq g_r(0)$.

When $|r| < \mu$, it is straightforward to show that any non-zero value of s will increase the second term more than it decreases the first term; therefore, in this case $s^* = 0$.

Given the analysis above, the unique optimal solution for s as a function of r and $\mu > 0$ is:

$$s = \begin{cases} \sigma(r + \mu), & \text{if } r < -\mu, \\ \sigma(r - \mu), & \text{if } r > \mu, \\ 0, & \text{otherwise.} \end{cases} \quad (\text{A.9})$$

Eqn. (A.9) can be more compactly stated as

$$S_{\sigma, \mu}(r) = \sigma \operatorname{sgn}(r) \max(|r| - \mu, 0).$$

Appendix B

Neyman-Pearson Lemma

B.1 Problem Formulation

Consider two densities $p(\mathbf{y}|\mathcal{H}_0)$ and $p(\mathbf{y}|\mathcal{H}_1, \boldsymbol{\theta}_1)$, for the parameter \mathbf{y} and random variable $\boldsymbol{\theta}$, where \mathcal{H}_0 is the *null-hypothesis*, and \mathcal{H}_1 is the *alternate-hypothesis*. A constrained optimization problem can be formulated and solved by Lagrange multipliers, to maximize the probability of detection, P_D , of event \mathcal{H}_1 , given the probability of false alarm, $P_{FA} = \alpha$.

For $\mathbf{y} \in \mathcal{X}$, the subspace \mathcal{X}_1 , where \mathcal{H}_1 is decided, is found by maximizing

$$P_D = \int_{\mathcal{X}_1} p(\mathbf{y}|\mathcal{H}_1, \boldsymbol{\theta}) d\mathbf{y}$$

under the constraint

$$P_{FA} = \int_{\mathcal{X}_1} p(\mathbf{y}|\mathcal{H}_0) d\mathbf{y} = \alpha \quad (\text{B.1})$$

where $0 < \alpha < 1$.

Define an objective function (the Lagrangian) using the Lagrangian multiplier γ ,

such that

$$\begin{aligned}
\mathcal{L} &= P_D - \gamma(P_{FA} - \alpha) \\
&= \int_{\mathcal{X}_1} p(\mathbf{y}|\mathcal{H}_1, \boldsymbol{\theta}) d\mathbf{y} - \gamma \left[\int_{\mathcal{X}_1} p(\mathbf{y}|\mathcal{H}_0) d\mathbf{y} - \alpha \right] \\
&= \int_{\mathcal{X}_1} [p(\mathbf{y}|\mathcal{H}_1, \boldsymbol{\theta}) - \gamma p(\mathbf{y}|\mathcal{H}_0)] d\mathbf{y} + \gamma\alpha.
\end{aligned}$$

For any given value γ , the region \mathcal{X}_1 that maximizes \mathcal{L} , and hence P_D , under the constraint $P_{FA} = \alpha$, is given by

$$\mathcal{X}_1 = \{\mathbf{y} \in \mathcal{X} \mid p(\mathbf{y}|\mathcal{H}_1, \boldsymbol{\theta}) > \gamma p(\mathbf{y}|\mathcal{H}_0)\}. \quad (\text{B.2})$$

Equation (B.2) yields the likelihood ratio test (LRT) [76] which is the *uniformly most powerful* (UMP) test [76] with $P_{FA} = \alpha$,

$$\Lambda(\mathbf{y}) = \frac{p(\mathbf{y}|\mathcal{H}_1, \boldsymbol{\theta})}{p(\mathbf{y}|\mathcal{H}_0)} \stackrel{\mathcal{H}_1}{\gtrless} \gamma,$$

where γ is determined from the constraint $P_{FA} \leq \alpha$ in eqn. (B.1).

B.2 Illustrative Example

In the following examples, we use modified figures from [47]. Consider the P_D versus the P_{FA} for given threshold γ for two signal distributions shown in Fig. B.1. Distribution *a* is *noise-only*, while distribution *b* is *signal-plus-noise*. Both distributions in Fig. B.1 have the same distance between the peaks. The height of the distributions represent how often a signal is present, and the spread of the distributions indicate the magnitude of noise present; less noise reduces the spread of the distributions, while more noise increases the spread.

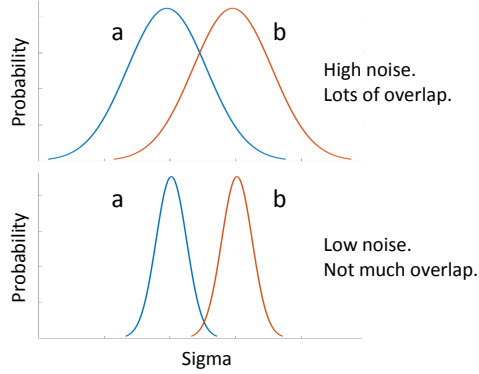


Figure B.1: Signal spread due to noise, and resulting overlap.

Consider the internal response to a signal detection system. In Fig. B.2, the vertical line represents the threshold γ , which splits the figure into four regions: a *hit* is defined as the *signal-plus-noise* region greater than (to the right of) γ , and a *miss* is the *signal-plus-noise* region less than (to the left of) γ . *False alarms* represent the *noise-only* region greater than γ , while *correct rejection* represents the *noise-only* region less than γ .

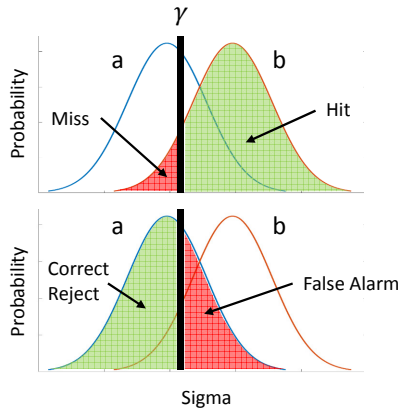


Figure B.2: The four regions of hypothesis testing, defined by two overlapping distributions (*a* & *b*) and the vertical line of the decision threshold γ .

Suppose that a low threshold is chosen, then the *signal-plus-noise* will likely be

detected, and therefore the system will have a very high hit rate, at the cost of an increased number of false alarms. Conversely, if the threshold is chosen to be high, then the number of false alarms will be reduced, at the cost of an increased miss rate. This is demonstrated by an example of threshold-shifting, shown in Fig. B.3.

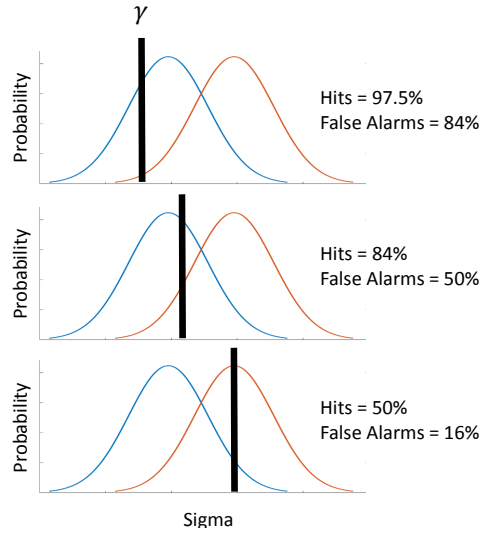


Figure B.3: An example result of *hits* versus *false alarms*, due to shifting the threshold γ .

Consider the following three conditions:

1. As the region \mathcal{X}_1 shrinks (γ tends toward infinity), both P_D and P_{FA} shrink toward zero.
2. As the region \mathcal{X}_1 grows (γ tends toward zero), both P_D and P_{FA} grow toward unity.
3. The case where $P_D = 1$ and $P_{FA} = 0$ will never occur if the conditional PDF's $p(\mathbf{x}|\mathcal{H}_0)$ and $p(\mathbf{x}|\mathcal{H}_1, \boldsymbol{\theta})$ overlap as in Fig. B.1.

Item 3 in the list above represents the fundamental trade-off in hypothesis testing, and motivates the N-P Lemma.

B.3 Relation to ROC Plots

In the 1940's, the Allied forces in England sought to make sense of the signals received from new Radar technology [58]. Specifically, they needed a graphical way to represent and determine a good signal from random noise. This graphical method is called the Receiver Operating Characteristic (ROC) plot, with the P_D equal to one minus the Probability of Missed Detection (P_{MD}) on the vertical axis (shown as *Hits* in Fig. B.4), versus the P_{FA} on the horizontal axis (shown as *False Alarms* in Fig. B.4). The *Discriminability index* (d'), where $d' = 0$, is the *Line-of-No-Discrimination*, indicating that any signal along or below this line cannot be discerned from random noise. The curves above this line, $d' = 1 \dots 4$, represent a detected signal with varying thresholds and/or discriminability. A perfectly detected signal lies on the vertical axis.

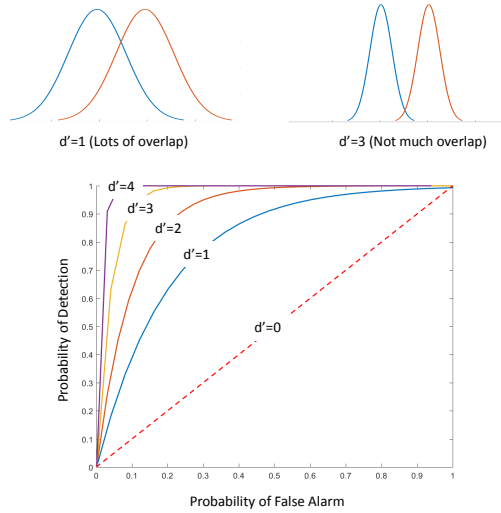


Figure B.4: ROC plot for Hits (P_D) versus False Alarms (P_{FA}).

The discriminability of a signal depends both on the separation and the spread of the *noise-only* and *signal-plus-noise* curves. Discriminability is made easier either by

increasing the separation (stronger signal) or by decreasing the spread (less noise). The number, d' , is often referred to as an estimate of the signal strength [58].

Appendix C

Generalized Likelihood Ratio Test

C.1 Problem Formulation

Consider a test for a signal present in Gaussian additive noise with non-zero mean [95]. A binary test can be performed for a random sample from a population that is normally distributed and has known variance. Based on the Neyman-Pearson (N-P) Lemma for binary hypothesis testing [59, 76], consider

$$\mathcal{H}_0 : \mathbf{y} \sim \mathcal{N}(\mathbf{0}, \boldsymbol{\sigma}^2 \mathbf{I}) \quad (\text{C.1})$$

$$\mathcal{H}_1 : \mathbf{y} \sim \mathcal{N}(\mathbf{H}\boldsymbol{\theta}, \boldsymbol{\sigma}^2 \mathbf{I}) \quad (\text{C.2})$$

for measurement $\mathbf{y} \in \mathbb{R}^{m \times 1}$, where $\boldsymbol{\sigma}^2 > 0$ is known, $\mathbf{H} \in \mathbb{R}^{m \times n}$ is known, and the unknown $\boldsymbol{\theta} \in \mathbb{R}^{n \times 1}$. The standard, or *null-hypothesis*, with known mean is defined as \mathcal{H}_0 , and the *alternate-hypothesis* with unknown mean is defined as \mathcal{H}_1 .

The Likelihood Ratio Test (LRT) [58] compares the model in \mathcal{H}_1 to the model in \mathcal{H}_0 , for threshold γ , such that

$$\frac{p(\mathbf{y}|\mathcal{H}_1, \boldsymbol{\theta})}{p(\mathbf{y}|\mathcal{H}_0)} \stackrel{\mathcal{H}_1}{\gtrless}_{\mathcal{H}_0} \gamma,$$

where

$$p(\mathbf{y}|\mathcal{H}_1, \boldsymbol{\theta}) = \frac{1}{(2\pi\sigma^2)^{k/2}} e^{-\left(\frac{1}{2\sigma^2}(\mathbf{y}-\mathbf{H}\boldsymbol{\theta})^\top(\mathbf{y}-\mathbf{H}\boldsymbol{\theta})\right)}$$

$$p(\mathbf{y}|\mathcal{H}_0) = \frac{1}{(2\pi\sigma^2)^{k/2}} e^{-\left(\frac{1}{2\sigma^2}(\mathbf{y}^\top\mathbf{y})\right)}.$$

When \mathcal{H}_1 is decided:

- if \mathcal{H}_1 is valid, this is a *correct detection*,
- if \mathcal{H}_1 not valid, this is a *false alarm*.

When \mathcal{H}_0 is decided:

- if \mathcal{H}_1 is valid, this is a *missed detection*,
- if \mathcal{H}_1 not valid, this is a *correct rejection*.

The log likelihood ratio test is

$$\ln(\Lambda(\mathbf{y})) = \ln\left(\frac{p(\mathbf{y}|\mathcal{H}_1, \boldsymbol{\theta}_1)}{p(\mathbf{y}|\mathcal{H}_0)}\right) \stackrel{\mathcal{H}_1}{\underset{\mathcal{H}_0}{\gtrless}} \gamma' \quad (\text{C.3})$$

where $\gamma' = \ln(\gamma)$.

Defining eqn. (C.3) in terms of eqn. (C.1) & (C.2) yields

$$\begin{aligned} \ln(\Lambda(\mathbf{y})) &= -\frac{1}{2\sigma^2} \left((\mathbf{y} - \mathbf{H}\boldsymbol{\theta})^\top(\mathbf{y} - \mathbf{H}\boldsymbol{\theta}) - \mathbf{y}^\top\mathbf{y} \right) \\ &= -\frac{1}{2\sigma^2} (-\mathbf{y}^\top\mathbf{H}\boldsymbol{\theta} - \boldsymbol{\theta}^\top\mathbf{H}^\top\mathbf{y} + \boldsymbol{\theta}^\top\mathbf{H}^\top\mathbf{H}\boldsymbol{\theta}) \\ &= -\frac{1}{2\sigma^2} (-2\boldsymbol{\theta}^\top\mathbf{H}^\top\mathbf{y} + \boldsymbol{\theta}^\top\mathbf{H}^\top\mathbf{H}\boldsymbol{\theta}). \end{aligned} \quad (\text{C.4})$$

The simplification in eqn. (C.4) is possible because: $\mathbf{y}^\top\mathbf{H}\boldsymbol{\theta} = \mathbf{y} \bullet (\mathbf{H}\boldsymbol{\theta}) = (\mathbf{H}\boldsymbol{\theta})^\top\mathbf{y}$. Because

$\boldsymbol{\theta}$ is unknown, eqn. (C.4) cannot be evaluated to implement a test.

The Generalized Likelihood Ratio Test (GLRT) [58] compares the *most likely* model in \mathcal{H}_1 to the *most likely* model in \mathcal{H}_0 , for threshold γ , such that

$$\frac{\max_{\boldsymbol{\theta}} p(\mathbf{y}|\mathcal{H}_1, \boldsymbol{\theta})}{\max_{\boldsymbol{\theta}} p(\mathbf{y}|\mathcal{H}_0)} \gtrless_{\mathcal{H}_0} \gamma.$$

The GLRT is determined by finding the Maximum Likelihood Estimate (MLE) of $\boldsymbol{\theta}$. The MLE estimates $\hat{\boldsymbol{\theta}}$ by finding the value of $\boldsymbol{\theta}$ that maximizes $\hat{\Lambda}(\boldsymbol{\theta}; \mathbf{y})$ [59], for $i = \{0, 1\}$:

$$\hat{\boldsymbol{\theta}}_i \triangleq \arg \max_{\boldsymbol{\theta}} p(\mathbf{y}|\mathcal{H}_i, \boldsymbol{\theta}).$$

For the alternate-hypothesis, the $\boldsymbol{\theta}$ that makes \mathbf{y} most likely is

$$\begin{aligned} \hat{\boldsymbol{\theta}}_1 &= \arg \max_{\boldsymbol{\theta}} p(\mathbf{y}|\mathcal{H}_1, \boldsymbol{\theta}) \\ &= \arg \max_{\boldsymbol{\theta}} \frac{1}{(2\pi\sigma^2)^{k/2}} e^{-\frac{1}{2\sigma^2}(\mathbf{y}-\mathbf{H}\boldsymbol{\theta})^\top(\mathbf{y}-\mathbf{H}\boldsymbol{\theta})} \end{aligned} \quad (\text{C.5})$$

$$= \arg \max_{\boldsymbol{\theta}} -\frac{1}{2\sigma^2}(\mathbf{y}-\mathbf{H}\boldsymbol{\theta})^\top(\mathbf{y}-\mathbf{H}\boldsymbol{\theta}) \quad (\text{C.6})$$

$$= \arg \min_{\boldsymbol{\theta}} (\mathbf{y}-\mathbf{H}\boldsymbol{\theta})^\top(\mathbf{y}-\mathbf{H}\boldsymbol{\theta}) \quad (\text{C.7})$$

$$= \arg \min_{\boldsymbol{\theta}} (\mathbf{y}^\top \mathbf{y} - 2\boldsymbol{\theta}^\top \mathbf{H}^\top \mathbf{y} + \boldsymbol{\theta}^\top \mathbf{H}^\top \mathbf{H}\boldsymbol{\theta}). \quad (\text{C.8})$$

The exponential function of $\boldsymbol{\theta}$ is an increasing function. Eqn. (C.5) can be reduced to eqn. (C.6) because the log of the exponent does not change the maximization of the exponent over $\boldsymbol{\theta}$. Eqn. (C.6) can be reduced to eqn. (C.7) because $\frac{1}{2\sigma^2}$ is independent of $\boldsymbol{\theta}$, which will not change the maximum relative to $\boldsymbol{\theta}$. Accounting for the negative value in eqn. (C.6) changes the problem from a maximization over $\boldsymbol{\theta}$, to an equivalent minimization over $\boldsymbol{\theta}$, in eqn. (C.7). Finally eqn. (C.8) is simply algebra.

To find $\hat{\boldsymbol{\theta}}_1$, take the partial derivative of eqn. (C.8) and set it equal to zero:

$$\begin{aligned} \frac{\partial}{\partial \boldsymbol{\theta}} (\mathbf{y}^\top \mathbf{y} - \boldsymbol{\theta}^\top \mathbf{H}^\top \mathbf{y} + \boldsymbol{\theta}^\top \mathbf{H}^\top \mathbf{H} \boldsymbol{\theta}) &= 0 \\ 0 - 2\mathbf{H}^\top \mathbf{y} + 2\mathbf{H}^\top \mathbf{H} \boldsymbol{\theta} &= 0 \\ \hat{\boldsymbol{\theta}}_1 &= (\mathbf{H}^\top \mathbf{H})^{-1} \mathbf{H}^\top \mathbf{y}. \end{aligned} \quad (\text{C.9})$$

Substituting eqn. (C.9) into eqn. (C.4) yields the analytical form of the GLRT

$$\begin{aligned} \ln(\hat{\Lambda}(\mathbf{y})) &= -\frac{1}{2\sigma^2} \left(-2\mathbf{y}^\top \mathbf{H}(\mathbf{H}^\top \mathbf{H})^{-1} \mathbf{H}^\top \mathbf{y} + \mathbf{y}^\top \mathbf{H}(\mathbf{H}^\top \mathbf{H})^{-1} \mathbf{H}^\top \mathbf{H}(\mathbf{H}^\top \mathbf{H})^{-1} \mathbf{H}^\top \mathbf{y} \right) \\ &= -\frac{1}{2\sigma^2} \left(-2\mathbf{y}^\top \mathbf{H}(\mathbf{H}^\top \mathbf{H})^{-1} \mathbf{H}^\top \mathbf{y} + \mathbf{y}^\top \mathbf{H}(\mathbf{H}^\top \mathbf{H})^{-1} \mathbf{H}^\top \mathbf{y} \right) \\ &= -\frac{1}{2\sigma^2} \left(-2\mathbf{y}^\top \mathbf{P}\mathbf{y} + \mathbf{y}^\top \mathbf{P}\mathbf{y} \right) \\ &= \frac{1}{\sigma^2} \left(\mathbf{y}^\top \mathbf{P}\mathbf{y} - \frac{1}{2} \mathbf{y}^\top \mathbf{P}\mathbf{y} \right) \\ &= \frac{1}{2\sigma^2} \mathbf{y}^\top \mathbf{P}\mathbf{y} \stackrel{\mathcal{H}_1}{\gtrless} \stackrel{\mathcal{H}_0}{\lessdot} \gamma', \end{aligned} \quad (\text{C.10})$$

where $\mathbf{P} \triangleq \mathbf{H}(\mathbf{H}^\top \mathbf{H})^{-1} \mathbf{H}^\top$.

From the result in eqn. (C.10), we can now determine the relation of the GLRT to the Probability of False Alarm (P_{FA}) and the Chi-square distribution.

C.2 GLRT relation to P_{FA} and χ^2

The objective is to choose γ' for the desired P_{FA} by evaluating eqn. (C.10) for the binary hypothesis. First, consider $\mathbf{y}^\top \mathbf{P}\mathbf{y}$ under \mathcal{H}_0 . Define \mathbf{H} in terms of the “thin” QR

factorization [42], e.g. $\mathbf{H} = \mathbf{Q}_1 \mathbf{R}_1$:

$$\mathbf{H} = \mathbf{Q}\mathbf{R}$$

$$= [\mathbf{Q}_1 \ \mathbf{Q}_2] \begin{bmatrix} \mathbf{R}_1 \\ \mathbf{0} \end{bmatrix}$$

$$= \mathbf{Q}_1 \mathbf{R}_1$$

where $\mathbf{Q} \in \mathbb{R}^{m \times m}$ is a basis for the column space of \mathbf{H} , and $\mathbf{R} \in \mathbb{R}^{m \times n}$ with $m > n$. Both \mathbf{Q}_1 and \mathbf{Q}_2 have orthogonal columns, where $\mathbf{Q}_1 \in \mathbb{R}^{m \times n}$, $\mathbf{Q}_2 \in \mathbb{R}^{m \times (m-n)}$. The parameter $\mathbf{R}_1 \in \mathbb{R}^{n \times n}$ is an invertible upper triangular matrix, and the zeros matrix, $\mathbf{0} \in \mathbb{R}^{(m-n) \times n}$. For full column-rank \mathbf{H} , i.e. $\text{rank}(\mathbf{H}) = n$, then both \mathbf{Q}_1 and \mathbf{R}_1 are unique.

Using the QR factorization of \mathbf{H} allows analysis of \mathbf{P} as

$$\begin{aligned} \mathbf{P} &= \mathbf{H}(\mathbf{H}^\top \mathbf{H})^{-1} \mathbf{H}^\top \\ &= \mathbf{Q}_1 \mathbf{R}_1 (\mathbf{R}_1^\top \mathbf{Q}_1^\top \mathbf{Q}_1 \mathbf{R}_1)^{-1} \mathbf{R}_1^\top \mathbf{Q}_1^\top \\ &= \mathbf{Q}_1 \mathbf{R}_1 (\mathbf{R}_1^\top \mathbf{I} \mathbf{R}_1)^{-1} \mathbf{R}_1^\top \mathbf{Q}_1^\top \\ &= \mathbf{Q}_1 \mathbf{R}_1 \mathbf{R}_1^{-1} (\mathbf{R}_1^\top)^{-1} \mathbf{R}_1^\top \mathbf{Q}_1^\top \\ &= \mathbf{Q}_1 \mathbf{Q}_1^\top \end{aligned} \tag{C.11}$$

where $\mathbf{Q}_1^\top \mathbf{Q}_1 = \mathbf{I}$. Substituting eqn. (C.11) into eqn. (C.10), the decision statistic is

$$\begin{aligned} \ln(\hat{\Lambda}(\mathbf{y})) &= \frac{1}{2\sigma^2} \mathbf{y}^\top \mathbf{P} \mathbf{y} \\ &= \frac{1}{2\sigma^2} \mathbf{y}^\top \mathbf{Q}_1 \mathbf{Q}_1^\top \mathbf{y} \\ &= \frac{1}{2\sigma^2} \mathbf{z}^\top \mathbf{z} \end{aligned}$$

where $\mathbf{z} = \mathbf{Q}_1^\top \mathbf{y} \in \mathbb{R}^{n \times 1}$ is a Gaussian random variable with m degrees of freedom, and

$\ln(\hat{\Lambda}(\mathbf{y}))$ is a $\chi^2_{(m-n)}$ random variable with $m - n$ degrees-of-freedom: the degrees-of-freedom of a Chi-square random variable is the number of measurements m , minus the number of parameters n .

Under the alternate hypothesis, $\mathcal{H}_1 : \mathbf{y}_1 \sim \mathcal{N}(\mathbf{H}\boldsymbol{\theta}, \boldsymbol{\sigma}^2\mathbf{I})$, the expected value of \mathbf{z}_1 is

$$\begin{aligned} E\langle \mathbf{z}_1 \rangle &= E\langle \mathbf{Q}_1^\top \mathbf{y} \rangle \\ &= \mathbf{Q}_1^\top E\langle \mathbf{y} \rangle \\ &= \mathbf{Q}_1^\top \mathbf{H}\boldsymbol{\theta}, \end{aligned}$$

and covariance of \mathbf{z}_1 is

$$\begin{aligned} E\langle \mathbf{z}_1 \mathbf{z}_1^\top \rangle &= E\langle \mathbf{Q}_1^\top \mathbf{y} \mathbf{y}^\top \mathbf{Q}_1 \rangle \\ &= \mathbf{Q}_1^\top (\boldsymbol{\sigma}^2 \mathbf{I}_n) \mathbf{Q}_1 \\ &= \boldsymbol{\sigma}^2 \mathbf{I}_n. \end{aligned}$$

Therefore, under \mathcal{H}_1 , $\mathbf{z}_1 \sim \mathcal{N}(\mathbf{H}\boldsymbol{\theta}, \boldsymbol{\sigma}^2 \mathbf{I}_n) \in \mathbb{R}^{n \times 1}$.

Under the null hypothesis, $\mathcal{H}_0 : \mathbf{y}_0 \sim \mathcal{N}(\mathbf{0}, \boldsymbol{\sigma}^2 \mathbf{I})$, the expected value of \mathbf{z}_0 is

$$\begin{aligned} E\langle \mathbf{z}_0 \rangle &= E\langle \mathbf{Q}_1^\top \mathbf{y} \rangle \\ &= \mathbf{Q}_1^\top E\langle \mathbf{y} \rangle \\ &= \mathbf{0}, \end{aligned}$$

and covariance of \mathbf{z}_0 is

$$\begin{aligned} E \langle \mathbf{z}_0 \mathbf{z}_0^\top \rangle &= E \langle \mathbf{Q}_1^\top \mathbf{y} \mathbf{y}^\top \mathbf{Q}_1 \rangle \\ &= \mathbf{Q}_1^\top (\boldsymbol{\sigma}^2 \mathbf{I}_n) \mathbf{Q}_1 \\ &= \boldsymbol{\sigma}^2 \mathbf{I}_n. \end{aligned}$$

Therefore, under \mathcal{H}_0 , $\mathbf{z}_0 \sim \mathcal{N}(\mathbf{0}, \boldsymbol{\sigma}^2 \mathbf{I}_n) \in \mathbb{R}^{n \times 1}$.

From eqn. (C.10), the test statistic is

$$\frac{\mathbf{z}^\top \mathbf{z}}{2\boldsymbol{\sigma}^2} \stackrel{\mathcal{H}_1}{\underset{\mathcal{H}_0}{\gtrless}} \gamma'. \quad (\text{C.12})$$

Given the P_{FA} constraint, the optimum decision threshold γ' is found by applying the inverse CDF of the Chi-square distribution with $m - n$ degrees-of-freedom. Thus, under \mathcal{H}_0 , we can define the P_{FA} in terms of the GLRT

$$P_{FA} = p(\chi_{(m-n)}^2 > \gamma).$$

In statistics literature, eqn. (C.12) is referred to as Wilks Theorem [100].